Self-propelled rod-like swimmers near surfaces

I n a u g u r a l - D i s s e r t a t i o n

zur
Erlangung des Doktorgrades
der Mathematisch-Naturwissenschaftlichen Fakultät
der Universität zu Köln

vorgelegt von

Kristian Marx

aus Braunschweig

Köln

2011

Berichterstatter: Prof. Dr. Gerhard Gompper
Prof. Dr. Johannes Berg

Tag der letzten mündlichen Prüfung: 30.01.2012

Contents

Abstract

Self-propelled microswimmers are biological organisms or synthetic objects that propel themselves through the surrounding fluid. Examples are sperm, various swimming bacteria such as Escherichia coli, the green alga Chlamydomonas reinhardtii and artificial bimetallic rods that catalyze chemical reactions in the surrounding hydrogen peroxide. Even though these swimmers differ in their size and driving mechanism, they can be classified as having *pusher* or *puller polarity*, which means that they are driven from the rear or the front, respectively. To study the differences in the dynamics of swimmers of different polarity, we develop a general model of rod-like swimmers and perform simulations in three dimensions, employing a particle-based mesoscopic simulation technique (multiparticle collision dynamics) for the hydrodynamic interactions.

In the center of our interest are the interactions of swimmers with walls and with each other at higher densities. In the dilute case, we find that all polarities (pusher, puller and neutral) show surface adhesion, the strongest in the pusher case. For pushers, this adhesion originates from sterical alignment with the wall and hydrodynamic attraction towards the wall, making them swim closest to the wall. For pullers, we show that they swim at a slightly larger distance from the wall than pushers, and that they are inclined towards the wall by a hydrodynamic repulsion of their middle part, which also leads to strong surface adhesion. We also measure the attractive force between pusher and wall and compare it to the dipole model, which is a commonly used far-field approximation for the flow surrounding polar swimmers.

Previous studies of self-propelled swimmers at high density were mostly performed in two dimensions or neglected either hydrodynamics or excluded-volume interactions. Using an efficient parallelization on GPU hardware, we are able to study the collective behavior of rods in three dimensions at various densities and driving forces, taking into account hydrodynamics and excluded-volume interactions. Our findings emphasize the importance of the polarity of swimmers: *Neutrally propelled* rods interact weakly via hydrodynamics, but display

an isotropic-nematic phase transition at lower critical densities than passive rods. Pusher rods align parallel with each other and form medium sized motile clusters that can develop into flow defects such as jets and swirls. The clusters primarily swim close to the surfaces, where the rod concentration is highest. The surface aggregation decreases with increasing rod density. While polar order is apparent at short distances within the clusters, at longer scales the flow defects destroy the order. However, nematic order is found to be slightly positive at a system-wide scale for high-density systems, indicating that clusters can align with each other. The clusters in puller systems are radically different. At low rod densities several small non-motile hedgehog-like clusters are formed at the walls, merging into one giant, system-spanning cluster at high rod densities. These giant clusters usually include a large fraction of all rods in the system. While these are jamming clusters, they are not static but deform slowly. We conclude that the puller clusters are due to aster-like defects, which have been predicted for puller fluids, combined with excluded-volume interactions.

A more specific model for sperm swimming is also being investigated. This model has been shown to display surface adhesion in the dilute solution and the capability to cluster and synchronize motion between two sperm. In multi-sperm simulations, we demonstrate the formation of small clusters by straight swimming sperm, but we find the interactions to be too weak for cluster formation among bent sperm. In order to strengthen interactions, we modify the sinusoidal beat pattern such that it displays an increasing amplitude towards the end of the tail. This indeed extends the time of two synchronized sperm swimming together, compared to the previous model.

1. Introduction

1.1. Motivation

In our everyday life, we encounter many lifeforms that are able to move through their environment, in order to feed, to protect themselves from predators, to reproduce or, in some higher species, just for the joy of it. We know that individual stimulus-controlled movement can be performed even by plants directing themselves towards the sunlight, however collective motion is usually attributed to be controlled by mind. A fish in a school actively steers its swimming to stay inside the swarm to be save from predators, herding zebras in the savanna and flocking birds do the same; traveling birds fly in a certain formation to reduce energy consumption and humans watch their every step not to bump into each other while walking in a crowd [1].

But the concept of mind controlling complex movement gets more and more questionable as the organisms become simpler and smaller. In fact, organisms living on the micrometer scale are observed to perform seemingly coordinated motions when they are in large numbers. They form clusters, swarms and swirls [2, 3], they get trapped near surfaces [4] and they can synchronize and capture each other to form large, regular patterns [5]. Some microscopic swimmers such as sperm employ chemical sensors to measure concentrations of a substance and a signaling network to follow its gradient (*chemotaxis*) [6, 7]. Some of them measure the nutrient concentration and adapt their motion patterns in order to reach or to stay in a nourishing environment, e.g. the E. coli bacterium [8]. Algae like Chlamydomonas reinhardtii and others typically dependent on photosynthesis, use optical sensors to direct their motion towards areas of higher light intensity (*phototaxis*) [9]. However, these microswimmers lack a complex nervous system allowing for direct observation of their fellows or communication, neither can they feel the collision with an obstacle or a wall. Sperm for example can follow a chemoattractant, but they do not produce it themselves. Therefore, communication between individuals is not necessary to

create this level of collective motion. The interactions via hydrodynamics [10] and steric interactions (collision, volume exclusion) [11] are already sufficient, and for many effects even one of these two is enough.

A better understanding of the collective behavior of simple microswimmers opens several perspectives for future applications. For example the presence of active swimmers influences fluid properties such as shear dependent viscosity [12] or the diffusivity of the solution [13, 14]. It might therefore be possible to design complex active fluids that meet specified requirements along these parameters.

To make chemical or biological analysis more efficient, considering the cost and the amount of material needed for the analysis, analysis devices can be miniaturized. Lab-on-a-chip solutions aim to implement the function of a small laboratory on a single chip, for example a glass plate with embedded microchannels for transport or mixing of different fluids, microsensors and even pumps. A few applications are already functional, for example a chip for counting sperm [15]. In the future it will be possible to use self-propelled swimmers activated by certain chemical components as biosensors or manipulators in microchannels, as they alter fluid properties such as viscosity, mixing or separation of different substances by being active or passive.

Our goal is to study the general behavior of self-propelled rod-like particles, especially their interactions at high swimmer densities close to boundaries, since this is a typical situation in microchannel geometries. Furthermore, most of the studies until now involved either steric interactions or hydrodynamic interactions, or they were carried out in (quasi-) two-dimensional systems, as will be reviewed in the following chapter. While these approaches are already proven to be very useful, the understanding of swimmer systems will significantly be advanced by combining both kinds of interactions in three-dimensional systems.

1.2. Hydrodynamics

1.2.1. Navier-Stokes equation

A fluid is a medium with a number of intrinsic properties like density ϱ, temperature T (or energy $k_\mathrm{B}T$), pressure p and the flow field $\vec{u}(\vec{r})$. From these, mass, energy and momentum of a given volume of the fluid can be calculated. The fluid behaves such that mass, energy and momentum are conserved in a closed system. From this principle alone follows the *Navier-Stokes equation*, which

describes the propagation of disturbances in the flow field $\vec{v}$ of incompressible ($\nabla\vec{u} = 0$) fluids [16]:

$$\varrho\left(\frac{\partial\vec{u}}{\partial t} + (\vec{u}\cdot\nabla)\vec{u}\right) = -\nabla p + \eta\nabla^2\vec{u} + \vec{f}(t) \tag{1.1}$$

The meanings of the terms are as follows.

- $\frac{\partial\vec{u}}{\partial t}$ is the acceleration of a volume element over time.
- $(\vec{u}\cdot\nabla)\vec{u}$ is the convection term, which describes the development of a volume element moving through space.
- $-\nabla p$ is the pressure gradient. The fluid experiences a force towards areas of lower pressure.
- $\eta\nabla^2\vec{u}$ is the viscous friction between layers of fluid moving with non-zero relative velocity.
- $\vec{f}$ is an external body force, for example gravity or boundary conditions.

1.2.2. Swimming in the low Reynolds-number regime

The Reynolds number is a dimensionless quantity describing the strength of viscous friction forces compared to inertial forces:

$$Re = \frac{\varrho v L}{\eta} = \frac{\text{inertial forces}}{\text{viscous forces}} \tag{1.2}$$

Here, L is a typical length scale, for example the diameter of a pipe in which the fluid is flowing, the diameter of a rigid body surrounded by fluid or the size of a swimmer. ϱ is the density of the fluid, η the viscosity, and v is the relative velocity between object and fluid. Typical Reynolds numbers of swimming objects range from $Re \sim 10^{-5}$ for microscopic swimmers such as E. coli over $Re \sim 10^3$ for small fish up to $Re \sim 10^8$ for whales [17].

A low Reynolds number has several consequences:

- For swimmers with $Re \ll 1$, inertial forces are basically irrelevant compared to friction. This affects coasting time: While an oil tanker needs at least 15 minutes for a complete stop with maximum reverse drive, a small bacterium stops coasting about 0.3μs after simply switching off the propelling mechanism [18].

- An object moving at low Reynolds numbers drags the surrounding fluid along. The result is that the shape of an object, be it of cubical form or of a streamlined bullet form, has little influence on the drag coefficient, if the surface area stays the same. Furthermore, it is a problem for self-propelled microorganisms as E. coli when collecting nutrients. They may be able to swim, but they drag along the surrounding, nutrient-poor fluid. Diffusion is much more efficient at restocking the wanted molecules compared to swimming towards them. However the bacterium can cross longer distances to reach areas of higher nutrient concentration, supporting the diffusional exchange.

- Fluid-flow patterns, e.g. the flow around a sphere, are laminar at low Reynolds numbers. With increasing Reynolds number, the resistance of the fluid to move *out of the way* of the swimmer grows, and between $Re \sim 1$ and $Re \sim 10^4$ the flow becomes turbulent [17].

- Replacing all physical quantities $(t, \vec{u}, \vec{r}, p, \vec{f})$ in the Navier-Stokes equation (1.1) by dimensionless quantities, the equation can be brought to the dimensionless form

$$\frac{\varrho v L}{\eta}\left(\frac{\partial \vec{u}}{\partial t} + (\vec{u}\cdot\nabla)\vec{u} + \nabla p\right) = \nabla^2\vec{u} + \vec{f}. \tag{1.3}$$

  Here, the Reynolds number appears as a prefactor on the left-hand side, therefore at low Reynolds numbers, the inertial terms can be neglected; this is called the *Stokes limit* of creeping flow.

In the Stokes limit, Eq. (1.1) is reduced to the Stokes equation:

$$\nabla p - \vec{f}(t) = \eta\nabla^2\vec{u} \tag{1.4}$$

Assuming we have a small system with a homogeneous pressure, the only two terms remaining are the friction and the external force. The beating flagellum of a swimmer is such an external force on the fluid. If it stops, $f = 0$, according to Stokes there is no friction anymore in the layers of the fluid close to the swimmer. This can only have one reason: The swimmer rests and does not coast along (as mentioned above). The swimming velocity of a swimmer is therefore proportional to the driving force. It swims at the velocity at which friction force and driving force balance each other, $\vec{F}_{\mathrm{D}} = -\eta\nabla^2\vec{u}$. Hence the swimmer is *force free*, it does not exert a net force on the surrounding fluid.

Equally important, there is no time dependency in Eq. (1.4) except for the external force $\vec{f}(t)$, therefore the dynamics will reverse if $\vec{f}(t)$ is reversed. Consider a swimmer in the Stokes regime undergoing a set of body deformations (e.g. a beating tail) that make it move from A to B. If afterwards the swimmer would perform the same set of deformations in reverse order, it would end up again at A, the whole system in the original state. This leads to the *scallop theorem* [18]: A swimmer should be able to swim continuously, hence the body deformation must be cyclic to be repeated over and over again. A scallop has only one degree of freedom for body deformation, opening and closing the shell. Assume that during one open-close cycle, the scallop moves from A to B. Afterwards, the time-reversed motion (open, close) takes it back from B to A. But because the open-close cycle looks the same in both time directions, it cannot be responsible for movement to opposite directions, and no movement can occur. A swimmer with a cyclic time-symmetric swimming stroke cannot move at all at $Re = 0$. In particular this is the case for all swimmers with just one degree of freedom and no rotating parts. Sperm solve this problem by the flexibility of their tail. It results in a traveling wave from front to rear in the flagellum. Under time reversal, the wave would travel from rear to front, which is clearly different. Sperm can swim. It is similar for E. coli and other swimmers using flagella forming helices that travel from front to rear by rotating them. Furthermore, the scallop theorem does not hold for a suspension of multiple swimmers synchronized via hydrodynamics. They have to be considered as one system with several degrees of freedom, and together they are able to swim [19, 20].

A very readable introduction to this topic is provided by E. M. Purcell [18].

1.2.3. Propulsion by flagellum: Anisotropic friction

A first study of the hydrodynamics of sperm propulsion by a planar or helical beat pattern has been done in 1952 by Taylor [21]. His method of calculating the interactions between the flagellum and the surrounding fluid are commonly known as *resistive-force theory* or *anisotropic friction*, and have been confirmed to high precision experimentally by detailed observations of the swimming patterns of sperm [22] and by comparison with the more accurate and complex slender-body theory[1] [24].

[1] Slender-body theory approximates the force a slender body exerts on the surrounding fluid by a distribution of stokeslets along the body [23].

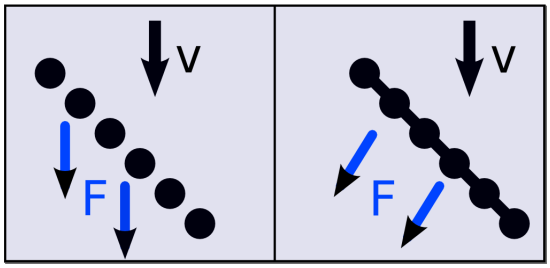

Figure 1.1.: Isotropic vs. anisotropic friction. A flagellum segment is moving down with velocity $\vec{v}$. Left: In the case of isotropic friction, the force on the fluid $\vec{F}$ is parallel to the movement: $\vec{F} \parallel \vec{v}$. Right: With anisotropic friction, movement and force are not parallel, allowing for the continuous generation of forward thrust.

Essential for the thrust generation of microswimmers is the resistance that flagella feel when moving through fluid. In the Stokes case of creep flow the friction coefficient is defined as the proportionality constant for the driving force $\vec{F}$ and the swimming velocity $\vec{v}$. A slender rod has friction coefficients $\gamma_{\parallel,\perp}$ for velocity components parallel and perpendicular to its orientation axis:

$$\gamma_{\parallel} = \frac{F_{\parallel}}{v_{\parallel}}, \qquad \gamma_{\perp} = \frac{F_{\perp}}{v_{\perp}} \tag{1.5}$$

Consider a segment of a flagellum that consists of individual, non-interacting beads and assume $\gamma_{\parallel} = \gamma_{\perp}$ for this segment. The flagellum moves with velocity $\vec{v}$ with both components (parallel and perpendicular) non-zero, as shown in the left part of Fig. 1.1. The resulting force on the fluid $\vec{F}$ would be parallel to the flagellum motion: $\vec{F} \parallel \vec{v}$. As mentioned above, the flagellar beat has to be cyclic, so after some time the flagellum segment will move with $-\vec{v}$, and the net driving force will be zero. Therefore, for a flagellum to produce thrust, the friction has to be anisotropic: $\gamma_{\parallel} \neq \gamma_{\perp}$, as shown in the right part of Fig. 1.1. In this case $\vec{v}$ and $\vec{F}$ are not parallel, a continuous thrust can be generated if the slope of the segment is inversed (as it is the case in a sinusoidal beat pattern for example).

The friction coefficients are related to the diffusion constants $D_{\parallel,\perp}$ via the Einstein relation

$$\gamma_{\parallel,\perp} = \frac{k_{\mathrm{B}}T}{D_{\parallel,\perp}}, \tag{1.6}$$

where k_{B} is the Boltzmann constant and T the temperature. A commonly used

result for the diffusion constant of a rod is [25]:

$$D_{\parallel} = \frac{\big(\ln(L/d) + \nu_{\parallel}(L/d)\big) k_{\mathrm{B}} T}{2\pi\eta L} \tag{1.7}$$

$$D_{\perp} = \frac{\big(\ln(L/d) + \nu_{\perp}(L/d)\big) k_{\mathrm{B}} T}{4\pi\eta L} \tag{1.8}$$

Here, $\nu_{\parallel,\perp}(L/d)$ are correction functions depending on the aspect ratio L/d of rod length L and diameter d. By numerically solving the hydrodynamic-interaction equations they were determined for $2 \leq (L/d) \leq 20$ as [25, 26]

$$\nu_{\parallel}(L/d) = -0.207 + 0.980 d/L - 0.133 (d/L)^2 \tag{1.9}$$

$$\nu_{\perp}(L/d) = 0.839 + 0.185 d/L + 0.233 (d/L)^2 \tag{1.10}$$

For example for $L/d = 20$, these results imply that the ratio for the friction coefficients is $\gamma_{\perp}/\gamma_{\parallel} \approx 1.48$. Simulations with the rod model used for the sperm flagella in Secs. 2.5 and 3.3 have been performed and yield good agreement [27].

1.3. Self-propelled swimmers

1.3.1. Swimmers in nature

Self-propelled swimmers are microorganisms that employ a propulsion mechanism to achieve directed motion in the surrounding fluid. Many of these organisms have a lengthy structure, they are therefore called *rod like*. A few example species are given in the following, pictures of some of them can be seen in Fig. 1.2:

- Sperm use the propulsion in combination with chemotaxis to reach the egg to fertilize it. Sperm of some species (e.g. sea urchin) even perform external fertilization, reaching the egg outside of the female body in open water [6]. The typical length scale of sperm is about 50μm.

- Escherichia coli bacteria travel to areas of higher nutrient concentration [8]. The typical size of the body of E. coli is $1-2\mu$m, the length of the flagella is on the order of 5μm. A comprehensive review of swimming E. coli can be found in Ref. [30].

- Myxococcus xanthus is a myxobacterium that spreads out for faster growth under normal conditions, but when starvation sets in, it aggregates by gliding on a surface into a more resistant fruiting body that can detach from the surface to be transported to a better suited environment [31].

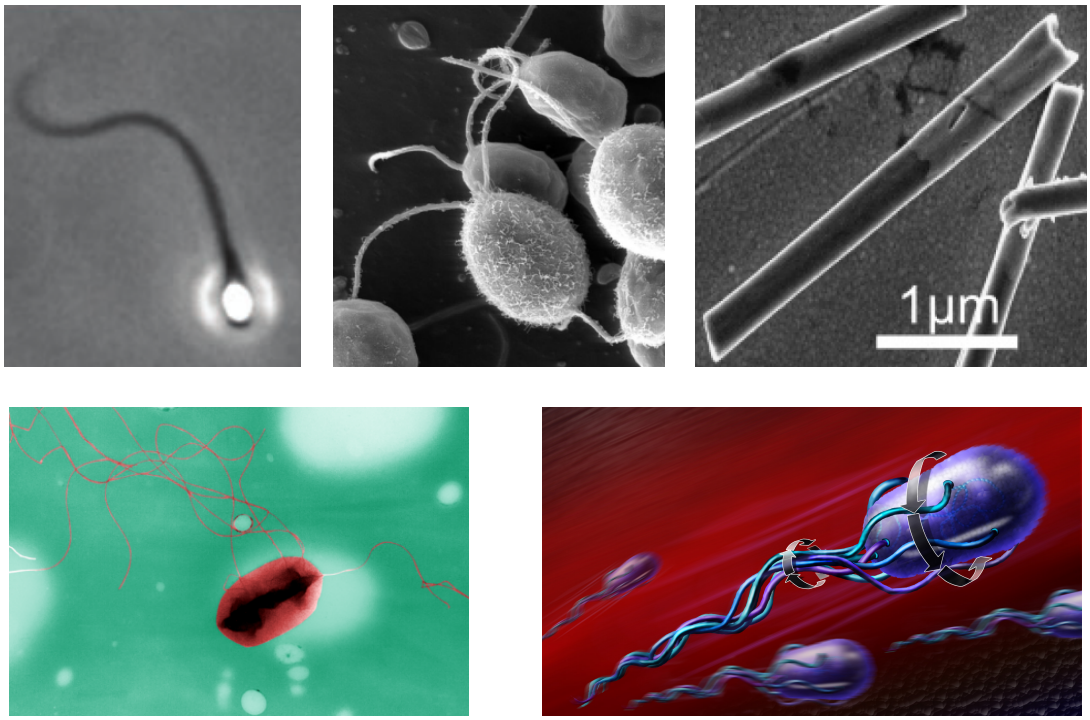

Figure 1.2.: Biological and synthetic microswimmers. Top, from left to right: Sperm [28], multiple Chlamydomonas reinhardtii (Dartmouth Electron Microscope Facility, public domain), palladium-gold nanorods [29]. Bottom: E. coli, resting in the left picture (E.H. White, public domain), swimming with bundled flagella in the right illustration (N. R. Fuller, National Science Foundation).

- Chlamydomonas reinhardtii is a green alga that can feed on sunlight. It uses two flagella at its front in a stroke pattern resembling breast swimming to move towards areas of higher light intensity [9]. The typical length of the cell body as well as the flagella is about 10μm.

- The green alga Volvox is a spherical multi-cellular organism that is propelled by flagella on thousands of its surface cells. Close to surfaces the hydrodynamic interaction between two Volvoxes is attractive, leading to cluster formation [32].

- Artificial bimetallic (e.g. palladium - gold) nanorods can act as a catalyst for surrounding hydrogen peroxide to decompose into water and oxygen. By this self-electrophoretic mechanism these rods produce directed motion [33, 29]. A review about artificial swimmers and their possible applications is given in Ref. [34].

- When actin filaments are placed on a surface coated with tethered motor proteins at sufficient density, the motor molecules attach to the polar filaments and start to move them across the surface, if ATP is present to fuel the process. As the coupling between the motor proteins and the filaments is polar, the molecules *walk* along the filaments always in the same direction, pushing the filament forward [35]. Note that these filaments are not force-free swimmers, instead they just drag along the surrounding fluid with their whole body. There is no part producing thrust on the filament.

1.3.2. Interaction mechanism

We focus here on self-propelled rod-like particles which interact via excluded volume (*steric* interaction, the bodies of the swimmers cannot interpenetrate each other) and hydrodynamic effects. Other mechanisms like chemical signaling are not considered. Direct collision of two self-propelled rods almost always happens between the front tip of rod 1 and the side of rod 2, direct tip-to-tip collisions are highly improbable. Such a collision between coplanar rods (or generally rods in two dimensions) is outlined in the left part of Fig. 1.3. Three situations are shown: The rods collide and

(A) align parallel if rod 1 hits rod 2 in front of the center of rod 2,

(B) aligned anti-parallel if rod 1 hits rod 2 shortly behind the center of rod 2,

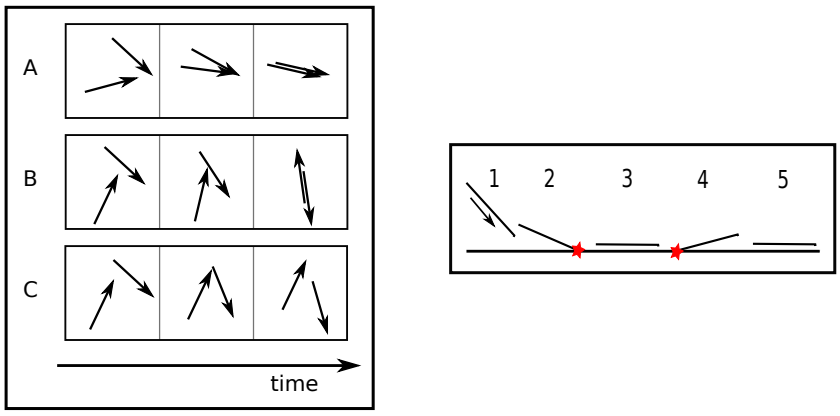

Figure 1.3.: Excluded volume interaction. Left: Two self-propelled coplanar (or two-dimensional) rods collide, the outcome depends on the point of collision (see text). Pictures from left to right symbolize the situation with passing time. Right: A self-propelled rod hits a hard surface in an oblique angle head first and gets aligned parallel to it (steps 1 to 3). Rotational diffusion lets the rod turn away from the wall, but it is suppressed to some degree because while turning away the rear end of the rod hits the wall (steps 4 to 5).

(C) change orientation only slightly if rod 1 hits rod 2 at the rear end.

In three-dimensional space these kinds of collision are much less common. Furthermore, many collisions of the (A) or (B) type end with the rods changing their orientation only slightly out of the plane common to both rods before the collision, so that the mutual alignment effect is much weaker. Only at high densities the steric interaction among swimmers becomes important again. For the interaction with the wall the case is entirely different, here excluded volume is as important in three dimensions as in two. In the process the swimmer approaches the surface at an oblique angle (Fig. 1.3 right) and hits it head first. The resulting torque aligns the rod parallel to the wall. In a system without Brownian dynamics the rod would stay at the wall for indefinite time, but the rotational diffusion turns it away from the surface. The rotational freedom however is limited by the rear tip of the rod hitting the wall, increasing the time the swimmer stays near the wall. It has been demonstrated that this kind of interaction alone is sufficient to explain strong surface aggregation if the swimming velocity is sufficiently high [36, 37], while passive rods show surface depletion for entropic reasons.

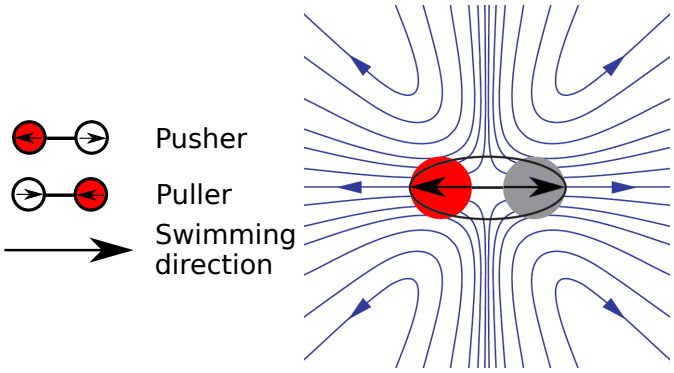

Figure 1.4.: Left: The forces exerted on the fluid by pushers / pullers. The red colored parts are the active ones. Right: Fluid flow field around a pusher (taken from Ref. [38]).

The short-range hydrodynamic interaction (HI) of swimmers strongly depends on the details of the swimmers under observation, but the mid- and long-range interaction can be approximated to leading order by a general model describing many kinds of rod-like self-propelled particles. A rod-like swimming organism usually has two linearly arranged parts: A passive part of the body (e.g. sperm head, E. coli body) that contributes drag to the balance of forces and an active part producing the propulsion (e.g. flagella, cilia). As described in Sec. 1.2.2, in the Stokes regime the swimmer does not exert a net force on the surrounding fluid. However, at the scale of the swimmer body, there is a spatial separation between the active part and the part experiencing only friction. The active part feels a positive force in moving direction, the passive part feels a negative force. It follows that the fluid surrounding the two parts also feels forces in opposite directions. In the linear geometry of the rod this gives two qualitatively different possible configurations, shown in Fig. 1.4 (left). The *pusher* (also called extensile swimmer) pushes out the fluid on both ends along the swimming axis, the *puller* (contractile swimmer) sucks in the fluid along this direction. Due to mass conservation the puller ejects the fluid perpendicular to its swimming direction at its center, the pusher sucks the fluid in at its waist, as can be seen in Fig. 1.4 (right). If the active and passive part are approximated as point forces of magnitude F_D and distance L, the swimmer can be described as a force dipole with a polarity $p = F_\mathrm{D} L$ [39, 38]. The induced flow $\vec{u}(\vec{r})$ at position $\vec{r}$ close to a

dipole can be described as

$$\vec{u}(\vec{r}) = \frac{p}{8\pi\eta r^3}(3\cos^2\theta - 1)\vec{r}, \tag{1.11}$$

where $\theta = \arccos\frac{\vec{r}\cdot\vec{p}}{|r||p|}$ is the angle between the dipole direction $\frac{\vec{p}}{|p|}$ and the flow position $\vec{r}$ [40]. The flow therefore decays proportional to $\frac{1}{r^2}$. Two parallel aligned swimmers with $p > 0$ swimming side by side attract each other, as for $\theta = \pi/2$ the flow $\vec{u}(\vec{r})$ is pointing towards the swimmer from the sides with $u_{\text{side}} \propto p/(\eta r^2)$, hence the $p > 0$ case describes the pusher. Furthermore, the induced flow field will result in a rotation of a swimmer in the flow field of another swimmer next to it with the angular velocity

$$\Omega \propto \frac{-p\left(\frac{\pi}{2} - \theta\right)}{\eta r^3}, \tag{1.12}$$

where $r = |\vec{r}|$ is the distance between the swimmers and θ is the angle between the swimmer orientation and the direction towards the other swimmer $\vec{r}$ [40]. For pushers ($p > 0$) the rotation leads to parallel alignment, for pullers ($p < 0$) it would lead to perpendicular alignment, but the perpendicular alignment of two moving swimmers is of course not a bound state. If the first puller passes by the second one, the second one can align parallel to the first puller and follow in its wake, because in this situation the two pullers attract each other. Similar behavior is observed for squirmers, spherical swimmers with propulsion by an imposed surface velocity, which can also be modeled as pushers or pullers. In this case the attractive force between pushers in the near-field is found to decay logarithmically with distance [41].

To describe the interaction of a polar swimmer with a wall, the complex flow induced by the whole swimmer can either be written (in the linear dynamics of the Stokes regime) as a superposition of flow singularities (stokeslets) [23] or, as a simplification, be considered as a force dipole. The interaction of these singularities with a no-slip wall can be described as interactions with multiple mirror-singularities on the other side of the wall that are positioned such that the flow field satisfies the no-slip condition at the wall [42]. The result is similar to the rod-rod interaction, a rotation towards parallel alignment of a pusher with the wall (on a timescale much shorter than rotation by Brownian motion for typical swimmers [4]) followed by an attractive force when alignment is reached. For the puller, the torque acts to turn the swimmer perpendicular to the wall, but if aligned parallel, the dipole field and its mirrors produce a hydrodynamic repulsion between puller and wall.

In a slit geometry with two opposing no-slip walls at a distance H, as it is used in our simulations, the drift velocity of a pusher aligned parallel to the wall at a distance z towards the wall is [4]:

$$v_z(z) = -\frac{3p}{64\pi\eta}\left(\frac{1}{z^2} - \frac{1}{(H-z)^2}\right) \tag{1.13}$$

Typical examples for pushers are sperm and the E. coli bacterium, and Chlamydomonas is considered the model organism for pullers. Still, it has to be considered that the approximation as a dipole is an oversimplification. The flow field of Chlamydomonas reinhardtii has been measured experimentally [43, 44], and strong deviations from the dipole model have been observed. In fact, the swimmer is better modeled by three stokeslets instead of one stresslet (dipole). In general, the dipole far-field approximation breaks down at distances r smaller than the swimmer size L.

An introduction to the behavior and modeling of microswimmers is given in Ref. [45].

1.3.3. Simple swimmer models with hydrodynamic interaction

One of the earliest and simplest models for the collective behavior of many self-propelled particles is the *Vicsek model*. Here, polar point particles with a constant swimming velocity interact by being oriented along the average of the orientation directions of the surrounding swimmers, plus some noise. This system shows a continuous phase transition when decreasing the noise strength from an isotropic state to a state showing global polar order [46]. A similar model with a hydrodynamic origin of the interactions is used in Ref. [47]. Point particles interact via a dipole force-field that represents the interaction among pushers, leading to short range orientation anisotropy and clustering behavior. At short distances though the pure dipole is a quantitatively insufficient description of the interactions of swimmers, and more elaborate numerical methods simulating the complete hydrodynamic interactions have to be employed.

Another severe disadvantage of these models is that the swimmers are point particles, meaning they cannot collide and do not resist being packed at large densities. While excluded-volume interaction between free swimmers in three-dimensional space usually involves only small degrees of reorientation at low volume fractions, swimmers on a plane that cannot interpenetrate each other often align parallel or anti-parallel to each other upon collision, leading to strong

changes in orientation for at least one of the collision partners. Furthermore collision is much more probable. Excluded-volume interaction therefore is much more dominant for two-dimensional swimmers, and even small systems without hydrodynamic interactions show a variety of interesting phenomena.

A first step to go beyond the far-field approximation was taken in Ref. [10]. A simple dumbbell swimmer is described in a two dimensional system by two point particles, which are connected by a stiff rod; one of the particles (the front particle in the puller case, rear particle in the pusher case) pushes the surrounding fluid behind the swimmer. The swimmers interact only via the hydrodynamics of the two point particles (and excluded volume interaction with walls). While surface aggregation is observed in dilute systems, the swimmer concentration profile becomes more homogeneous for higher densities. This is surprising, as among the swimmers of Ref. [10] there is no volume exclusion. The propulsion mechanism of the dumbbell swimmer is sometimes called a *phantom flagellum*, because the swimmer feels a propulsion force and the surrounding fluid feels the inverse momentum transfer without the presence of any moving parts on the swimmer. While these models are not as realistic as swimmers that propel themselves by e.g. beating a real flagellum, they account for a much larger, general range of rod-like self-propelled swimmers, making it possible to determine characteristics of this class of swimmers without the interference of specifics like the beat pattern, that usually create a lot of hydrodynamic disorder. Later, the dumbbell model is extended to include excluded-volume interactions between the swimmers [38]; surface aggregation and the influence of confinement (the distance between two opposing channel walls) on the diffusivity of the swimmers and passive tracers is studied. It is shown that negative correlations that are usually attributed to collective motion (and the resulting flow defects like swirls), also exist in strongly confined dilute systems.

Another variant of a phantom-flagella swimmer is presented in Ref. [48]. Here, pusher bacteria are modeled in three dimensions by two passive balls representing head and tail, and hydrodynamic point force at various positions along the axis connecting the balls. These configurations also include variants where the point force is located outside of the head-tail pair, some distance behind the tail or in front of the head. This simple model can be analyzed analytically, as it is the superposition of two dipoles. The interaction between two approaching swimmers is analyzed, however their results seem to contradict the experimental evidence of bound states for pushers.

A different concept of propulsion is followed by a swimmer sometimes called the *Golestanian swimmer*. It consists of three linearly aligned spheres connected by stiff bonds that can change their length. Because the swimmer has two degrees of freedom, the movement can be conducted non-reciprocal, and it is proven that it can swim [49]. Experimentally, this swimmer has been used as a fluid pump: The three spheres are individually controlled by optical tweezers to perform the non-reciprocal stroke. The swimmer is however not allowed to move, therefore it induces a fluid flow in its vicinity and acts as a pump [50].

1.3.4. Macroscopic effects

When Lord Rothschild 1963 put a drop of diluted bull sperm between two glass plates and observed it under the microscope, he detected that they were not homogeneously distributed in the fluid but showed maximum concentration directly at the surface of the plate [51]. This effect has since been observed for self-propelled swimmers in experiments [4] and simulations [52, 53, 54, 10, 55]. It follows from the swimmer-wall interactions described in section 1.3.2, but it is still subject of discussion whether the steric or the hydrodynamic interaction dominates. For example the experimentally determined surface aggregation of E. coli is explained and reproduced by a model solely based on steric interaction in Ref. [37], and equally successful explained and modeled by pure hydrodynamic dipole interaction in Ref. [4]. One of the goals of our investigations is to learn about the role played by the different interaction mechanisms.

From a macroscopic standpoint the combination of swimmer and medium is often called *active fluid*, emphasizing that it is intrinsically out of equilibrium, because the swimmers constantly dissipate energy. At the same time, it can be viewed macroscopically as a medium with special properties in which other, larger objects can be embedded. For example it has been shown that the presence of active swimmers influences the viscosity under shear conditions. Rods (passive or active) do not align parallel with the axis of extension in shear flows (perpendicular to the fluid-velocity gradient), but often are oriented such that the tips of the rods are both located in fluid flows with a component pointing away from the rod center. If the rod is an active pusher, the resulting dipole force supports this flow, leading to shear-thinning[2]. The puller on the other

[2]While for Newtonian fluids like pure water the viscosity is independent on shearing, in fluids showing *shear-thinning* the viscosity of some fluids is reduced at high shear rates [12, 14].

side is working against the shear flow, leading to the opposite effect of *shear-thickening*. Experiments with Chlamydomonas however paint a mixed picture, also showing shear-thinning at low shear rates due to fast reorientation of the algae [56]. The presence of self-propelled swimmers also greatly increases the diffusivity of tracer particles (or other passive substances solved in the fluid). This has been shown in simulations [14] and in experiments [13].

1.3.5. Collective motion

Though the microscopic dynamics of single swimmers are interesting by itself, systems containing a high number of swimmers often show astounding behavior that does not follow in a trivial way from the microscopic features, but emerges from the interaction between many individuals. This emergence of complex patterns is observed for many different kinds of systems, including bacteria, swarming fish, flocking birds, herding land-animals and pedestrians [1].

Many bacteria (e.g. M. xanthus and sometimes E. coli) usually do not swim in the bulk of water but live on surfaces, where they employ different translocation mechanisms such as swimming in a thin layer of fluid or cell-to-cell interaction via filaments, moving by growth or gliding [57, 58]. These organisms form quasi-two-dimensional systems, in which swarming phenomena are enhanced due to the stronger swimmer interactions compared to three-dimensional systems. Because of this, and due to the fact that two-dimensional systems are much easier to study in experiment, simulation and theory, these systems are much better examined than three-dimensional systems. In the following, some typical collective-motion effects are briefly described.

Giant density fluctuations If the driving force is dominant compared to the thermal and background noise, swimmers are not distributed homogeneously in the system but form various kinds of clusters. The clustering of self-propelled hard rods (without hydrodynamic interaction) depending on the driving force to diffusion ratio (*Peclet number*) has been studied in two dimensions in Ref. [59]. In systems where diffusion processes dominate, the rods do not cluster; with decreasing noise and increasing density, they begin to form small motile clusters, up to a single large jamming cluster[3] capturing all swimmers in the system. Rods

[3] A cluster is called *jamming* if it is immotile because of rods with all kinds of orientation blocking each other or rods mostly stuck in solid walls like hedgehog clusters shown in Fig. 1.5.

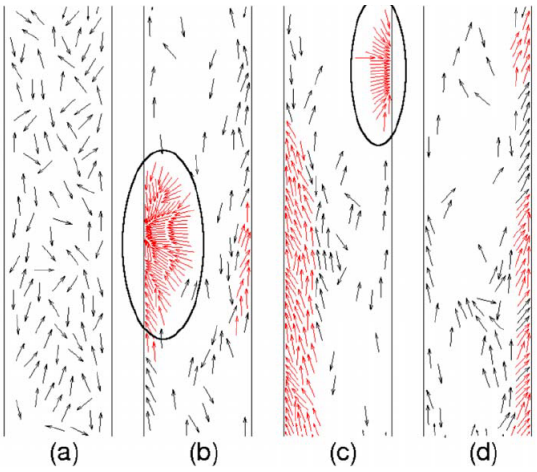

Figure 1.5.: Two-dimensional self-propelled hard rods in a channel geometry. (a): Isotropic initial condition. (b): After some time, jamming hedgehog clusters form when rods hit the wall and are blocked by following rods from aligning parallel to it. (c): The jamming clusters later become nematic (left cluster) and motile, and transform into simple wall aggregates (d) gliding along the wall. (Taken from [55].)

in a two-dimensional channel geometry (without hydrodynamic interactions) form transient hedgehog clusters [55], shown in Fig. 1.5b. When single rods hit the wall at a steep angle, following rods collide with them before they can align parallel to it, blocking the possibility to align and thus forming the hedgehog clusters. They are however not stable, after some time they become nematic and motile (on the left wall of Fig. 1.5c) and decay into simple wall aggregates (Fig. 1.5d).

Density waves In certain two-dimensional systems of self-propelled rods, density waves traveling through the system can be found. As these are motile polar patterns, they move along with the swimmers. These waves have been found in systems where filaments are being transported by surface-tethered motor proteins. At low filament density the system is disordered, but above a critical density motile polar clusters form, resulting at even higher density in the formation of polar density waves (Fig. 1.6) that keep their polar orientation over a long time [35].

In a different system of polar point particles that interact only via a torque that aligns close particles parallel to each other the formation of bands has been

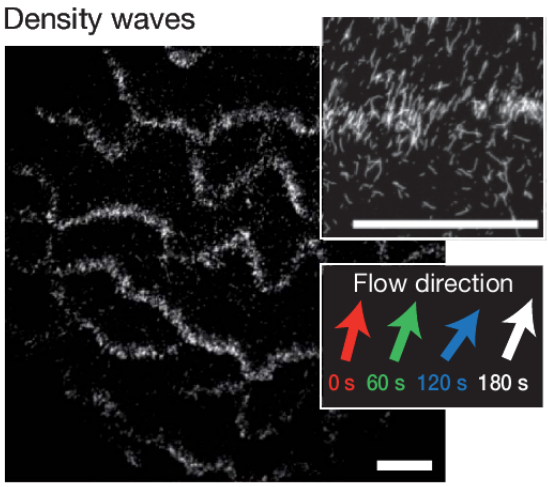

Figure 1.6.: Motor proteins tethered on a substrate couple to mobile actin filaments and move them across the surface. At high filament density ordered domains appear and form traveling polar density waves. (Taken from Ref. [35].)

observed. At low noise levels, the system is homogeneous, but with increasing noise the steady state shows the formation of bands of higher density and higher polar order compared to the surrounding areas [60]. The difference to density waves is that bands are elongated along the axis of polar order of the rods therein. In contrast, waves have a broad front that is perpendicular to the polar order of the rods forming them. Following from this is that bands can be stationary, while waves move through the system.

Segregation of passive and active particles For systems containing actively driven rods and passive rods that interact only via excluded volume, it was demonstrated that the active and passive particles segregate from each other. Depending on swimming speed, aspect ratio and composition complex patterns emerge, ranging from a disordered system over formation of small and medium sized motile clusters and polar band structures to large domains of purely active or passive rods [61].

Nematic phase transition at lower densities According to Onsager hard rods of length L and zero diameter in a two-dimensional system undergo a phase transition from the isotropic to the nematic phase at the critical density

$\phi^{\mathrm{crit}}_{\mathrm{passive}} = 3/(\pi L^2)$ [62]. This results from an entropic ordering process; at high densities, aligning all rods parallel decreases rotational entropy, but the increase in translational entropy more than compensates this loss. For active systems, it has been observed that the phase transition happens at lower critical density, compared to passive systems [63]. This results from the alignment produced by the collision of two self-propelled rods, while in passive systems only entropic effects play a role. A Smoluchowski equation for the configurational probability density of self-propelled rods has been derived in Ref. [64] and compared to the passive case described by Onsager. It is used to calculate the critical density of the isotropic-nematic phase transition for active rods in two dimensions to be [65]:

$$\phi^{\mathrm{crit}}_{\mathrm{active}} = \frac{\phi^{\mathrm{crit}}_{\mathrm{passive}}}{1+\frac{v^2}{5k_{\mathrm{B}}T}} = \frac{3}{\pi L^2\left(1+\frac{v^2}{5k_{\mathrm{B}}T}\right)} \tag{1.14}$$

Flow defects It has been shown however that global nematic and especially polar order (but also the isotropic state) are unstable in systems of self-propelled polar rods if hydrodynamic interactions are accounted for. Orientational order in active fluids is (among other effects) destroyed by flow defects predicted in Ref. [66, 67] and observed in Refs. [68, 69, 10]. These defects are studied in more detail in Ref. [70], where it is found that pusher rods in two dimensions tend to create spiral-like flow defects, while puller rods favor asters. Contrary to this, in Ref. [68] puller fluids are predicted not to show any instability.

Sperm trains and vortices When sperm are captured close to surfaces by the interaction mechanisms described in Sec. 1.3.2, the interaction between them is increased, making synchronization and swarming possible. It has been demonstrated that sea urchin sperm, which swim in circles when adhering to a surface, can entangle each other to form *sperm vortices* consisting of ten to twelve individuals [5]. At the densities necessary for this phenomenon, many such vortices form at once, aligning in a lattice (left pictures in Fig. 1.7). A different kind of cooperation is observed among sperm of the wood mouse. These sperm form large motile clusters (*sperm trains*) of thousands of swimmers in the female reproductive tract, increasing their swimming velocity and thus gaining an advantage over competing sperm from other males [71]. In this case, however, the interaction is not purely hydrodynamic; the wood-mouse sperm possesses a hook at its head that is deployed after ejaculation, and which is used to attach

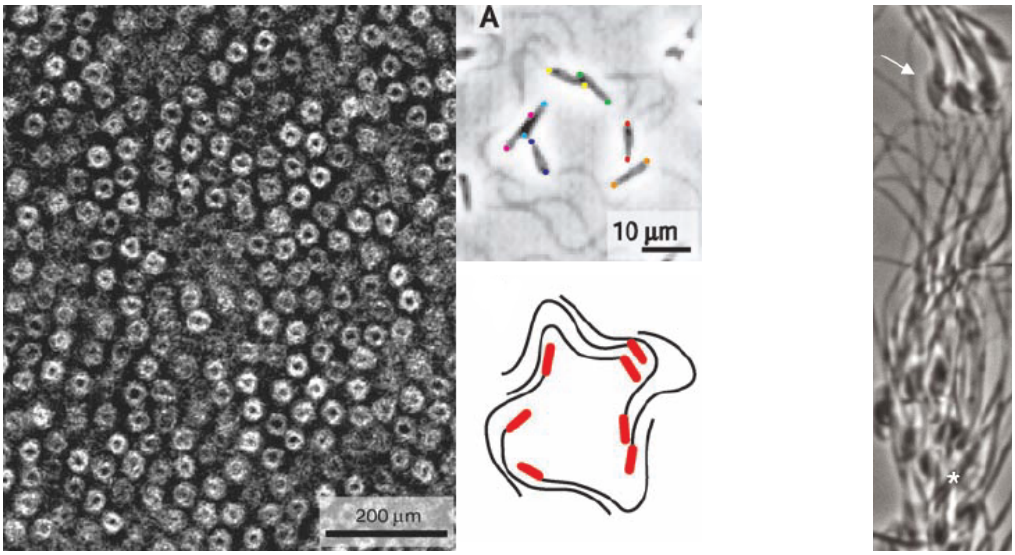

Figure 1.7.: Left: Sea urchin sperm trapped near a glass surface aggregate and form two-dimensional sperm vortices that align in a lattice. (Taken from Ref. [5].) Right: Wood mouse sperm attach to each other by apical hooks and form sperm trains that enhance swimming velocity. (Taken from Ref. [71].)

on flagella or hooks of other sperm. The right picture in Fig. 1.7 shows such a sperm train.

1.3.6. Sperm model hydrodynamics

While a self-propelled rod is a general model for rod-like swimmers, a more specific model for sperm has been developed [72]. In short, the model consists of a spherical head and a semi-flexible flagellum (Fig. 2.4). The flagellum includes a stiff, passive mid-piece near the head and a tail that is beating with a sinusoidal pattern to drive the swimmer. Either just the mid-piece or the complete flagellum can be assigned an additional curvature (called the *mid-piece curved* (MC) and *tail-curved* (TC) model, respectively), leading to helical trajectories when swimming in the bulk and circular trajectories when captured by a wall. The idea is to study the influence of the specific driving method of sperm as one class of self-propelled swimmers. As the details of the anatomy of sperm and beat pattern vary quite strongly among different species, this again is a rather general approach.

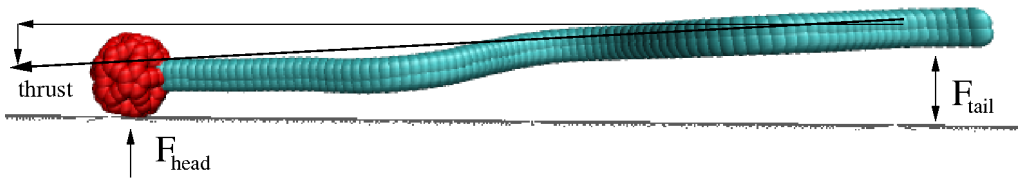

Figure 1.8.: Wall-adhesion mechanism of a sperm: Near a wall the beating plane of the flagellum aligns parallel to the surface. A small force F_{tail} repels the end of the flagellum from the wall, inclining the sperm orientation and hence the vector of thrust towards the wall. (Taken from Ref. [52].)

For a two-dimensional version of the sperm model, synchronization and clustering between sperm of different beat frequencies and phase shifts have been studied [73]. It was found that the sperm attract each other and form clusters. The cluster size diverges if all sperm have the same beating frequency, otherwise its mean decreases with a power law when increasing the frequency distribution variance. It has to be noted however, that hydrodynamic interactions are much stronger in two dimensions than in three.

In Refs. [72, 52] the swimming behavior of single three-dimensional sperm has been studied. In the bulk, the curvature C_{H} of the helical trajectory depends linearly on the preferred curvature c_0 of the tail or mid-piece for models employing a torsional stiff flagellum (MCS, TCS). In the case of a torsional elastic flagellum (MCE), the tail reacts stronger to the dynamic deformations by the hydrodynamic forces and the dependence of C_{H} on c_0 becomes non-linear. This twisting of the elastic flagellum also results in a discontinuous dependence of the rotation frequency of the beating plane on the curvature c_0 for the MCE model.

Once in contact with a (no-slip) wall, all sperm models display a tendency for adhesion, continuing to swim close to the wall in circles (or in a straight line if $c_0 = 0$). The degree of the surface adhesion depends on the model, where MCE and TCS produce the strongest surface excess [52], and MCS sperm show only weak adhesion for intermediate bending [74]. The mechanism of the wall adhesion is primarily the pusher interaction described in Sec. 1.3.2. A secondary effect supports the adhesion, it is outlined in Fig. 1.8; the beat of the tail in a plane parallel to the wall pushes the surrounding fluid not only to the rear, but also above and below the swimmer. This results in a small repelling force F_{tail} between the tail and the wall, while at the transition from mid-piece to tail

there is an attractive force towards the wall due to the fluid being sucked in. This leads to a slight inclination of the whole swimmer and therefore the sperm vector of thrust towards the wall. While swimming, the head hits the wall with the force F_{head}, but F_{tail} is still sufficient to maintain the inclination, keeping the sperm near the wall. Similar behavior has been observed for a pure flagellum without head or mid piece [53].

The inclination of the sperm towards the surface has also been observed experimentally for sperm with a planar beat pattern [75]. It is however not attributed to a repellent force between the end of the tail and the wall but to a hydrodynamic force pushing the head against the wall due to a hydrofoil effect generated by a flattened sperm head. Other simulation studies also suggest that the flattened form of the head is important for the wall adhesion, and describe a different adhesion mechanism, where the sperm swims at a finite distance from the wall in a force equilibrium between hydrodynamic attraction towards the wall and a slight inclination *away* from it [76]. It was argued [77] that the difference in the behavior results from details in the anatomy of sperm species and models. It is however evident that the sperm model of Ref. [72] shows a strong surface adhesion with a simple spherical head, indicating a flattened head is not essential to the phenomenon. This controversy was motivation for studies of the influence of anatomic parameters of our sperm model on the surface aggregation [74] and sperm cooperation, that are described in Secs. 3.3.2 and 3.3.3.

2. Methods

To study and understand different aspects of a system of microswimmers, it is beneficial to approach the problem with various methods. Experiments deliver the most realistic conditions and therefore count as the final judge considering validity of models. In the sense of *observing nature*, experiments also often give the starting motivation for further studies. The disadvantages are that not all parameters and observables of the system are accessible, quite often complex indirect methods of measurement have to be used. Numerical simulations try to model aspects of a system that are expected to be relevant for the occurrence of observed interesting behavior. Recreating real-world experiments in the computer makes all degrees of freedom, down to the smallest simulation element, subject to direct observation. Even more, situations that cannot be built in the laboratory because of special initial conditions or the variation of parameters fixed in nature are easy to simulate. Also of interest is using the level of model detail as a parameter. Reducing it (for example in the step from the sperm model to the rod model, as explained later in this chapter) can provide information about which aspects are needed to create certain phenomena, and how to generalize observations. Finally, theoretical approaches usually describe even more simplified versions of nature and often are only applicable to a limited set of problems. Theoretical descriptions tend to give the most insight to why a system behaves as it does.

All three approaches, experiment, simulation and theory, complement each other and have their own necessity. We focus here on numerical simulations.

2.1. Scales in simulations

Most dynamics simulations implement the following steps:

1. Calculate the interactions between all elements of the system.

2. Integrate equations of motion describing the dynamics over a certain time period Δt.

The differences between simulation approaches lie in the characteristic length scale of the system and in the special aspects of interest.

Similar to mathematical models describing aspects of the real world within a certain scope of application, computer simulations have an inherent scale that on the one hand limits their validity and precision describing small scale behavior, and on the other hand limits the maximum size of a system that can be treated. While quantum mechanics is necessary to study the formation of smaller molecules, the folding process of larger proteins can by today only be treated using simpler effective potentials in all-atom simulations. Here, every single atom of the molecule is represented by a point particle and its interactions, which can be bonded or non-bonded. Especially the non-bonded interactions are difficult from the computational point of view, as there is no principal limit in interaction partners. Each particle in the system may interact with every other. Complexity therefore scales quadratically with the number of particles present. To reduce computational cost, usually two strategies are employed:

1. Limit the interaction range and introduce some sort of book keeping in the algorithm to avoid comparing particles at large distances every time step.

2. Reduce the number of degrees of freedom by coarse graining.

The first point will be addressed in appendix A. Coarse graining means to replace recurring groups of elements in a model by one single element, which is now the smallest element in the simulation. Bonded atoms can be replaced by a single *bead* (a point particle or sphere) representing the molecule or monomer they form. These monomers can than interact to form larger structures.

An example for this strategy is the *bead-spring model*. A polymer, or more general a larger body (rod, micelle, membrane...) is formed by a number of beads tethered together by Hookean springs and sometimes other potentials that help form a desired shape. This concept will be used to construct models for microswimmers in Sec. 2.4 below. Of course this coarse graining neglects any structure on a length scale smaller than the group of elements that is being represented by a single bead.

Fast processes (e.g. molecular vibration) usually happen on very small length scales. That means, spatial coarse graining also implies coarse graining in time, making it possible to increase the time step Δt in the simulation without loosing too much accuracy. Quite often, aspects of the system that live on smaller length- and timescales are approximated by stochastic processes. Especially Monte Carlo algorithms make use of this concept, but also the MPC dynamics described in this chapter work this way.

The typical length scale of the simulations of microswimmers is about 1μm. The relevant factors of the system that should be represented well by the model can be summarized as:

- The swimmer: Either a rigid rod or a sperm consisting of a spherical head and a beating flagellum.
- Excluded-volume interactions between swimmers.
- Walls with excluded-volume interactions with the swimmers.
- Hydrodynamic interactions (HI) between all parts of the system.
- A large number of swimmers (rods), on the order of 10^3.

The chosen method is *molecular dynamics* (MD) for the modeling of the swimmers (consisting of beads, the *solute* particles) and a mesoscale hydrodynamics simulation approach, *multi-particle collision dynamics* (MPCD), for the hydrodynamic interactions.

2.2. Molecular dynamics

The molecular dynamics part of the simulation describes the bonded interactions (within a swimmer) and the non-bonded excluded-volume interactions as well as the motion of the solute particles (beads of mass m_b). For the integration of the equations of motion, the *Velocity Verlet* scheme is used, which is a variation of the *Verlet algorithm* [78]. The forces are calculated as follows:

Bonded interactions Both kinds of swimmers (sperm and rods) consist of a number of point particles connected by bonds with a finite equilibrium extension l_b. The interaction potential between two bonded beads at distance r is

$$V_b(r) = \frac{1}{2} K_\mathrm{b} (r - l_\mathrm{b})^2. \tag{2.1}$$

with K_b the spring constant. The interaction partners are hard-coded for the rods and stored in a list for the sperm model. Additionally, a second potential is needed to give the rods stiffness. For rods with $\hat{L}$ beads at positions $\vec{r}_0, \ldots, \vec{r}_{\hat{L}-1}$ we use the bending potential

$$V_\mathrm{bend}(\vec{r}_0, \ldots, \vec{r}_{\hat{L}-1}) = \frac{1}{2} K_\mathrm{bend} \sum_{i=1}^{\hat{L}-2} (\vec{r}_{i+1} - 2\vec{r}_i + \vec{r}_{i-1})^2 \tag{2.2}$$

The force on bead $j = 0, \ldots, \hat{L}-1$ calculated from this potential is (for simplicity we use scalars here, the equation is valid for every component of $\vec{F}^{(j)}_\mathrm{bend}$ and $\vec{r}_j$)

$$\begin{aligned}
F^{(j)}_\mathrm{bend} &= \frac{\partial}{\partial r_j} V_\mathrm{bend} \\
&= r_{j+2} - 4r_{j-1} + 6r_j - 4r_{j-1} + r_{j-2} \quad \text{for} \quad j = 2, \ldots, \hat{L} - 3 && (2.3) \\
F^{(\hat{L}-2)}_\mathrm{bend} &= -2r_{\hat{L}-1} + 5r_{\hat{L}-2} - 4r_{\hat{L}-3} + r_{\hat{L}-4} && (2.4) \\
F^{(\hat{L}-1)}_\mathrm{bend} &= r_{\hat{L}-1} - 2r_{\hat{L}-2} + r_{\hat{L}-3} && (2.5)
\end{aligned}$$

and similar for $j = 0, 1$.

Excluded volume The beads have a radius $r_\mathrm{b}/2$ such that two beads of different swimmers should not be able to come considerably closer than r_b. This is achieved by implementing a truncated and shifted, purely repulsive Lennard-Jones potential between them:

$$\begin{aligned}
V_\mathrm{VE}(r) &= \begin{cases} 4\left(\left(\frac{\sigma}{r}\right)^{12} - \left(\frac{\sigma}{r}\right)^{6}\right) + 1, & \text{for} \quad r < r_\mathrm{b} \\ 0, & \text{else} \end{cases} \\
\text{with} \quad r_\mathrm{b} &= \sqrt[6]{2}\sigma
\end{aligned} \tag{2.6}$$

For reasons given in Sec. 2.3.6, a similar Lennard-Jones potential keeps the beads from penetrating the boundary walls. For details about the implementation and parallelization of the excluded-volume interaction on the CPU and GPU (*graphics processing unit*), see appendix A.

2.3. Multi-particle collision dynamics

MPC dynamics is a mesoscale particle-based algorithm to simulate microfluidics at the micrometer scale. The fluid is represented by point particles (*solvent*

particles) of mass m_{fl} that move deterministically, but interact stochastically. In the stochastic process several fluid particles interact simultaneously (hence the name *multi*-particle collision), making it possible to avoid costly pairwise interactions. The MPC algorithm was introduced by Malevanets and Kapral [79] and further analyzed in Refs. [80, 81, 82], extensive reviews can be found in Refs. [83, 84]. Among its advantages are the following points:

- Thermal fluctuations are naturally included.
- The computational cost depends only linearly on the volume of the system, but not on the number of embedded objects. It is thus ideal for the simulation of a large number of swimmers.
- Arbitrarily shaped boundaries can be efficiently realized.
- Embedding solute particles (e.g. self-propelled rods) is easy.
- Efficient parallelization is possible.

The variant of the MPC scheme used in this work is described in the following.

2.3.1. Stochastic rotation dynamics

The simulation advances in discrete time steps Δt_{mpc} and consists of two alternating parts: The streaming step and the collision step.

Streaming step During the ballistic streaming step the fluid molecules propagate linearly without interacting. For each particle i a new position is calculated by

$$\vec{r}_i(t + \Delta t_{\mathrm{mpc}}) = \vec{r}_i(t) + \vec{v}_i(t)\Delta t_{\mathrm{mpc}}, \tag{2.7}$$

where $\vec{v}_i(t)$ is the particle velocity. Force terms may also be added to achieve flow. A constant acceleration of the fluid particles combined with no-slip boundary walls for example leads to a Poiseuille flow.

Care must be taken concerning boundary conditions, as will be explained below. If there are embedded objects in the fluid, their movement is simulated by molecular dynamics as described in the previous chapter. By means of simulation time, this happens simultaneously to the streaming step of the fluid.

Collision step As described in Sec. 1.2.1, an essential part for correct hydrodynamics is the conservation of mass and momentum. The first is trivial, as the particle number is constant, the latter must be fulfilled by the stochastic collision.

The idea is to divide the system into cubic cells and simulate the interaction of all particles in a cell by assigning new, random *relative* velocities to them without changing the center-of-mass velocity of the particles within the same cell. This means, momentum is conserved on the cell level, therefore also in the whole system. The new relative velocities can be directly drawn from the Maxwell-Boltzmann distribution. This is called the *MPC Anderson thermostat* (MPC-AT). It has the disadvantage to require many random numbers, the performance is limited by the performance of the random-number generator. An alternative is the *stochastic rotation dynamics* (MPC-SRD) approach:

1. Divide the system box into cubic cells of linear size a.[1] The average number of fluid particles per cell is $\hat{\rho}$.

2. For each cell C_j calculate the center-of-mass velocity $\vec{v}_j^{\,\mathrm{cm}}$ of all particles (solvent and solute) $i \in C_j$ with velocity $\vec{v}_i$ and mass m_i in the cell C_j:

$$\vec{v}_j^{\,\mathrm{cm}}(t) = \frac{1}{M_j} \sum_{i \in C_j} \vec{v}_i(t)\, m_i \quad \text{with} \quad M_j = \sum_{i \in C_j} m_i \tag{2.8}$$

3. For each cell C_j choose a unit vector of random direction $\vec{e}_j$ and calculate a rotation matrix $\underline{\underline{R}}(\vec{e}_j, \alpha)$ that rotates vectors by the angle α around the axis $\vec{e}_j$.

4. For each particle i (solvent and solute) in every cell C_j, calculate a new velocity by rotating the relative velocities using the rotation matrix:

$$\vec{v}_i(t + \Delta t_{\mathrm{mpc}}) = \underline{\underline{R}}(\vec{e}_j, \alpha)\Big(\vec{v}_i(t) - \vec{v}_j^{\,\mathrm{cm}}(t)\Big) + \vec{v}_j^{\,\mathrm{cm}}(t) \tag{2.9}$$

   This step is illustrated in Fig. 2.1.

While the SRD algorithm is usually faster than MPC-AT, it does not conserve angular momentum (in contrast to MPC-AT [85, 86]).

[1] The cell size a is considered as the basic unit of length in MPC simulations and usually chosen as $a = 1.0$.

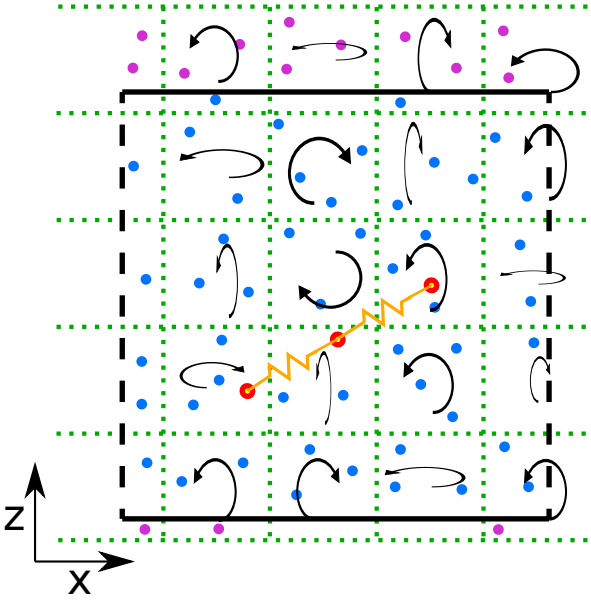

Figure 2.1.: The SRD collision step: The system has periodic boundaries in x-direction (dashed black line), no-slip walls in z-direction (solid black line). The relative velocities of the particles (solvent, blue, and solute, red) in each cell are rotated around an axis common to all particles in one cell, but different among other cells. The grid (green) is randomly shifted, cells adjacent to no-slip walls that are only partly filled with fluid particles are filled with virtual particles (violet).

Random grid shift Due to the grid of MPC-cells, slow moving fluid particles may stay in the same cell over multiple time steps Δt_{mpc} and therefore interact with the same other fluid particles over and over again. This leads to correlations between fluid particles that influence the fluid behavior. The correlations however only appear, if the particles mean free path, which is $\lambda = \Delta t_{\mathrm{mpc}} \sqrt{k_{\mathrm{B}} T / m_{\mathrm{fl}}}$ on average, is smaller than the cell size a in the inertial frame of the grid. Therefore, the algorithm introduces a dependence on the inertial frame, as a fluid moving relative to the grid would show a different behavior than a resting fluid.

To avoid this violation of Galilean invariance, a random grid shift is introduced before every MPC step [87]. Here, the origin of the grid of cells is shifted by $(\zeta_0, \zeta_1, \zeta_2)$, where $\zeta_i \in [0, 1)$ are equally distributed random numbers.

2.3.2. Random MPC: Switching off hydrodynamic interactions

Hydrodynamic interactions can be viewed as long-range correlations between fluid molecules. Next to these correlations the MPC fluid fulfills another task, it reproduces thermal fluctuations and provides a background friction. In some situations, e.g. to elucidate the relevance of hydrodynamic interactions compared to other aspects of the system, it is beneficial to be able to switch off the long-range correlations while still keeping the thermal fluctuations and not changing fluid properties like the viscosity significantly. This is possible efficiently by replacing the explicit fluid particles by *virtual particles* [88]. These particles are not stored in memory (as correlations are unwanted) and therefore do not participate in the streaming step. They just contribute to the center-of-mass calculation in the collision step with momentum drawn from a Maxwell-Boltzmann distribution of variance $m_{\mathrm{fl}} k_{\mathrm{B}} T$ and zero mean (if no flow is present). Their velocity components are Gaussian distributed, and as the sum of Gaussian-distributed random numbers is itself Gaussian distributed, instead of $\hat{\rho}$ virtual particles of mass m_{fl} it is sufficient to draw the velocity for a single particle of mass $\rho a^3 = \hat{\rho} m_{\mathrm{fl}}$. This means the collision step is only carried out for cells that contain monomer particles, and Eq. (2.8) becomes:

$$\vec{v}_j^{\,\mathrm{cm}}(t) = \frac{1}{M_j^{\mathrm{mon}} + \rho} \left(\vec{\xi}_j + \sum_{i \in C_j^{\mathrm{mon}}} \vec{v}_i(t)\, m_i \right) \quad \text{with} \quad M_j^{\mathrm{mon}} = \sum_{i \in C_j^{\mathrm{mon}}} m_i \tag{2.10}$$

Here, C_j^{mon} denotes only the monomer particles in cell C_j, and $\vec{\xi}_j$ is a random Maxwell-Boltzmann distributed momentum of variance $\rho k_{\mathrm{B}} T$.

2.3.3. Thermostat

The fluid dynamics itself conserves energy, but active swimmers dissipate energy and heat up the system. To keep it at constant temperature T, the fluid must be coupled to a heat bath. This can be achieved by a thermostat that rescales the velocities of the particles. Furthermore, in systems with inhomogeneous energy dissipation (e.g. a few self-propelled swimmers) temperature gradients form over time, inducing density gradients, viscosity fluctuations etc.

The simplest thermostat globally rescales all (relative) velocities with the same factor. To counter inhomogeneous heating, one usually applies cell-level thermostats that rescale only the relative velocities of particles within an MPC-cell to conserve large-scale flows. The thermostat used in our simulations is explained in Ref. [83]: For every cell C_j,

1. draw a random real number $\Psi \in [1, 1 + c]$, where $c \in [0.05, 0.3]$ is the strength of the thermostat.

2. Randomly select a scaling factor $S = \Psi$ or $S = 1/\Psi$ with equal probability.

3. Rescale the velocities with S with the acceptance probability $p_A = \min(1, A)$ where

$$A = S^{3(\hat{\rho}_j - 1)} \exp\left[-\frac{m_{\mathrm{fl}}}{2 k_{\mathrm{B}} T} \sum_{i=1}^{\hat{\rho}_j} (\vec{v}_i - \vec{v}_j^{\,\mathrm{cm}})^2 (S^2 - 1) \right]. \tag{2.11}$$

   Here, $\hat{\rho}_j$ is the number of fluid particles in that cell and $\vec{v}_j^{\,\mathrm{cm}}$ its center-of-mass velocity.

2.3.4. Boundary conditions

Two different boundary conditions are used, periodic boundary conditions and hard walls.

Periodic boundary conditions The (linear) increase of computational cost with the volume of the fluid limits the maximum size of systems that can be treated. The system geometry of interest however often is of (almost) infinite size, be it a free fluid without walls or a slit geometry with walls only in certain directions. To achieve this, boundary effects can be minimized by effectively replicating the simulation box over and over again, i.e. by connecting the ends of the box along the direction in question. In Fig. 2.1 the dashed black lines symbolize that particles leaving the box in positive x-direction to the right will enter the box again from the left. Moving in a system with periodic boundaries in two directions and hard walls in the remaining direction can be compared to moving inside of a spherical shell (if the curvature is ignored).

Periodic boundary conditions of course lead to perfect long-range correlations on the order of the system size. A single swimmer might interact with its periodic images if the system size is chosen too small.

No-slip boundary conditions At the microscopic scale, the fluid layer adjacent to a solid wall rests relative to it. In simulations, no-slip walls are achieved by the bounce-back boundary condition and so-called *ghost particles*. For the bounce-back condition, (fluid-) particles hitting the wall have their velocity reversed in the moment of contact with the wall[2]: $\vec{v}_{\text{new}} = -\vec{v}_{\text{old}}$. Still, this alone is not sufficient. The grid shift leads to the possibility of partly filled cells at the boundaries, as can be seen in Fig. 2.1. In case of periodic boundaries (left and right in Fig. 2.1), the incomplete cells are connected to form a complete cell, in the case of solid walls however no such connection exists, and partly filled cells lead to the occurrence of a certain amount of slip at the surface [89]. To circumvent this, resting virtual particles (ghost particles), similar to those described in section 2.3.2 about random MPC, are introduced in the partly filled cells. Let C_j be a cell adjacent to a wall and only filled with $\hat{\rho}_j$ fluid particles (instead of $\hat{\rho}$). In the collision step, the particles in C_j interact with each other

[2]This is different from the billiard-ball picture of bouncing objects, where only the velocities perpendicular to the wall are inversed, but not the velocity parallel to it. The billiard-ball behavior describes a slip-boundary condition.

Symbol	Description	Value
a	MPC-cell size	1.0
α	SRD rotation angle	130°
Δt_{md}	MD time step	0.001
Δt_{mpc}	MPC time step	0.02
m_{fl}	fluid particle mass	1.0
m_{b}	solute particle mass	10.0
l_{b}	bond length between beads	$1.0a$
$\hat{\rho}$	fluid particles per cell	10
r_{b}	excluded volume bead diameter	0.8
$k_{\mathrm{B}}T$	thermal energy	1.0
η	fluid viscosity	$41.17\sqrt{mk_{\mathrm{B}}T}/a^2$

Table 2.1.: Parameters used in the rod simulations reported in this work, if not mentioned otherwise.

and with $(\hat{\rho} - \hat{\rho}_j)$ virtual particles (see Fig. 2.1). Virtual particles are not stored in memory and do not have positions, their velocities are drawn from a Maxwell-Boltzmann distribution of variance $m_{\mathrm{fl}}k_{\mathrm{B}}T$ and contribute to the calculation of the center-of-mass velocity. Instead of $(\hat{\rho} - \hat{\rho}_j)$ virtual particles of mass m_{fl} a single virtual particle of mass $(\hat{\rho} - \hat{\rho}_j)m_{\mathrm{fl}}$ can be used.

The ghost particles also act as an additional thermostat, a heat bath at the walls. In most systems however this cooling is not sufficient and might even lead to temperature gradients and therefore to an inhomogeneous density if no other thermostat (or only a global thermostat) is used.

2.3.5. Units and parameters

The simulations are performed with dimensionless units. The basic units are:

- Length: MPC-cell size a
- Mass: Fluid-particle mass m_{fl}
- Energy: $k_{\mathrm{B}}T$
- Force: $k_{\mathrm{B}}T/a$

- Time: $\sqrt{m_{\mathrm{fl}} a^2/(k_{\mathrm{B}}T)}$

A more comprehensive list of all parameters used for the simulations described in this work (if not mentioned otherwise) is given in Tab. 2.1. Considering a typical swimming speed of $v = 0.02$ and a swimmer length of $L = 20$ the rods are studied at a Reynolds number of $Re \approx 0.1$.

2.3.6. Fluid properties

Viscosity The viscosity η of the fluid has two contributions, the kinetic viscosity η_{kin} and the collisional viscosity η_{col}, with $\eta = \eta_{\mathrm{kin}} + \eta_{\mathrm{col}}$. The kinetic contribution dominates the viscosity in the regime of long mean free paths $\lambda \equiv \Delta t_{\mathrm{mpc}} \sqrt{k_{\mathrm{B}}T/m_{\mathrm{fl}}} > a$, when momentum exchange mainly happens by particles moving through the system [81, 90]:

$$\eta_{\mathrm{kin}} = \frac{\hat{\rho} k_{\mathrm{B}} T \Delta t_{\mathrm{mpc}}}{2a^3} \left(\frac{5\hat{\rho}}{(\hat{\rho} - 1 + e^{-\hat{\rho}})[2 - \cos(\alpha) - \cos(2\alpha)]} \right) \tag{2.12}$$

The collisional contribution dominates when the mean free path is smaller than the cell size ($\lambda < a$, as it is the case when using the parameters from Tab. 2.1).

$$\eta_{\mathrm{col}} = \frac{m_{\mathrm{fl}}(\hat{\rho} - 1 + e^{-\hat{\rho}})}{18 a \Delta t_{\mathrm{mpc}}} [1 - \cos(\alpha)] \tag{2.13}$$

According to Eq. (1.2) a large viscosity is needed for the desired small Reynolds number. This makes a small MPC time step Δt_{mpc} necessary, increasing computational cost. Another advantage of a small Δt_{mpc} is a large Schmidt number

$$Sc = \frac{\eta}{\rho D}. \tag{2.14}$$

The Schmidt number is the ratio of momentum transport to mass diffusivity and is typically large ($Sc \sim 10^2$) for liquids [91], compared to small ($Sc \sim 1$) for gases.

Limitations of the MPC fluid One main difference between the MPC fluid and a liquid is the compressibility. The equation of state is the same as for an ideal gas[3] [83]

$$p = \frac{N_{\mathrm{A}} k_{\mathrm{B}} T}{V}, \tag{2.15}$$

[3] At the same time, the large viscosity, small Reynolds number and large Schmidt number clearly distinguish the MPC fluid from a gas.

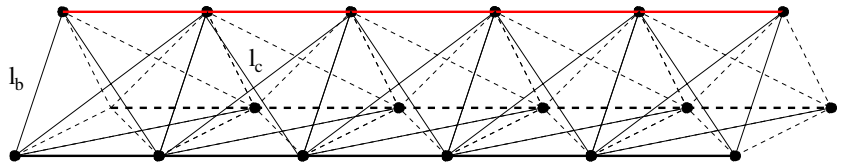

Figure 2.2.: A rod consisting of three filaments, interconnected by direct crosslinks of length l_b and diagonal crosslinks of length $l_c = \sqrt{2}l_\mathrm{b}$. The tail of the sperm model has the same structure. (Schematic from [36].)

where N_A is the Avogadro number and V is the volume under consideration. This results in a compressibility $\chi \propto 1/\rho$. Fast movement of embedded solute particles therefore can lead to the formation of longitudinal waves, strong density fluctuations, traveling through the system with the speed of sound $c_\mathrm{s} = \sqrt{2k_\mathrm{B}T/m_\mathrm{fl}}$. The time scale for the propagation of shear waves can be estimated by viewing the Navier-Stokes equation (1.1) as a diffusion equation

$$\frac{\partial \vec{u}}{\partial t} = \frac{\eta}{\rho}\nabla^2\vec{u} \tag{2.16}$$

with $\frac{\eta}{\rho}$ as an effective diffusion constant. It follows that the time it takes a shear wave to travel a distance r is $t_\mathrm{shear}(r) = \frac{\rho}{\eta}r^2$. The disturbance in the flow field produced by a passing by swimmer needs this time to reach the wall at distance r. Thus, swimmer and wall can only interact if the swimmer does not move too far in the time of the traveling signal.

Finally, the scale a of the MPC cell gives a lower limit for spatial resolution of the hydrodynamics. This is also important for interactions with walls, objects should not be much closer than $1.0a$ to walls. Interactions of embedded objects with boundaries on scales larger than a have been shown to be reproduced correctly [92, 93].

2.4. Rod model

A self-propelled rod is among the simplest generic models of self-propelled swimmers. It is a semi-flexible rod built of beads without any actively moving parts. The beads are connected by harmonic springs of finite equilibrium extension $l_\mathrm{b} = 1.0$ as described by Eq. (2.1). Bending stiffness is achieved by the potential

described in Eq. (2.2). Spring constant K_b and bending rigidity K_bend are chosen such that the rod is essentially stiff and not changing length. $\hat{L}$ such connected beads form one filament, and the swimmer rod consists of either one or three filaments. The structure of the three-filament rod is depicted in Fig. 2.2.

Within a distance r_w from the walls the beads feel a repulsive force from a truncated Lennard-Jones potential similar to Eq. (2.6), but with range $r_\mathrm{w} = 0.7a$ instead of r_b. It is therefore improbable that a significant part of a filament is located in the MPC-cell layer adjacent to the wall, which otherwise might lead to unphysical non-hydrodynamic effects.

The propulsion of the rod is achieved by applying a constant force on every *active* bead while applying the inverse momentum change to the surrounding fluid, equally distributed among the fluid particles present in the same MPC cell as the propelled bead. It is therefore a phantom-flagellum model. The choice which of the beads are active determines the polarity of the swimmer:

- Pusher: The rear half of the rod is propelled.
- Puller: The front half of the rod is propelled.
- Unpolar: All beads are propelled.

In any case, all beads feel the drag of the surrounding fluid.

Due to details of the propulsion method used here[4], the driven beads experience a stronger friction in forward direction than the passive beads. This effectively reduces the driving force F_D significantly to an (unknown) effective driving force $F_\mathrm{D}^\mathrm{eff} < F_\mathrm{D}$, and we cannot calculate the friction coefficient $\gamma_\parallel$ using the swimming velocity of the rod and Eq. (1.5). However, this has no impact on fluid dynamics. The drag coefficient γ of the passive rod without driving force can still be measured by switching off the repulsion effect on the surrounding fluid. This way, the rod is no longer self propelled, but pulled along by a constant external force F_ext (comparable to a charge in a homogeneous electrical field), and the drag coefficient is

$$\gamma = \frac{F_\mathrm{ext}}{v}. \tag{2.17}$$

[4] A driven bead exerts an opposite momentum change on all fluid particles in the same MPC cell. Thus, as the bead has a high probability of interacting with some of these fluid particles in the next collision step, the bead feels the drag from the surrounding flow it has just induced, and that is directed in the opposite direction of the beads movement.

2.4.1. Constrained motion of single rods

In some cases measurements are greatly simplified by limiting or fixing some of the degrees of freedom of the swimmer. For example measuring the force between a swimmer parallel to the wall depending on the distance to the wall in z-direction is much easier if the swimmer is aligned parallel to the wall at a certain distance by exterior forces (see section 3.1.2). This could be achieved by simply setting the z-component of every bead to a fixed value. This however means that the temperature at this degree of freedom is zero. To avoid this, the z-components of every bead are *almost* fixed, controlled by a strong harmonic potential

$$V_{\mathrm{Z}}(z) = \frac{1}{2} K_{\mathrm{Z}} (z - z_0)^2. \tag{2.18}$$

A (constant) external force (e.g. hydrodynamic attraction) that is compensated by this potential can be measured by averaging $z - z_0$ over time:

$$F_{\mathrm{ext}} = K_{\mathrm{Z}} \left\langle z(t) - z_0 \right\rangle_t \tag{2.19}$$

In some cases (e.g. measuring the drag coefficient of a single rod) this potential is applied to two degrees of freedom (z and y). Especially in this case the space that can be occupied by the swimmer is drastically reduced, which might amplify finite-size effects. A rod swimming "on a rail" in a system with periodic boundary conditions might pass the same position over and over again in quick succession, leading to local flows, strong inhomogeneous heating and density fluctuations; thus, a large enough system has to be chosen.

2.4.2. Multi-rod systems

While single-rod systems are necessary to learn about the details of the model used in these studies and represent the experimental condition of strongly diluted active fluids, multi-rod systems represent the more common setting of active fluids with high densities of swimmers. There are several new aspects of interactions: The hydrodynamic interactions between the swimmers directly follow from the MPC dynamics, but for mutual volume exclusion an interaction as described in section 2.2 is added. Two-dimensional rods made from spherical particles tend to form a regular lattice by dense sphere packing, as shown in Fig. 2.3. As the beads and gaps of neighboring rods interlock, it is hard for them to glide past each other, effectively increasing the friction between rods. This

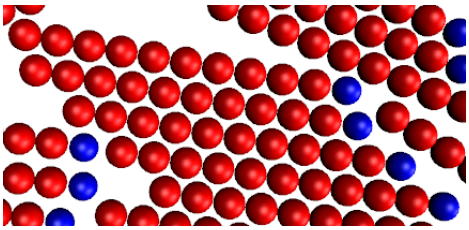

Figure 2.3.: Rods consisting of non-overlapping beads tend to form a regular lattice by dense sphere packing in two-dimensional systems. This increases the friction in large jamming clusters. In three dimensions this interlocking is much less common and does not pose a problem.

supports the formation of jamming clusters as observed in Ref. [59]. This effect is much less severe in three-dimensional systems, especially with further noise coming from hydrodynamic interactions. Indeed observations of our simulations do not show the crystalline structure of dense sphere packing.

To keep systems of different volumes comparable, we define a volume fraction

$$\phi = \frac{V_{\text{rod}}}{V} = \frac{\pi(r_{\text{b}}/2)^2 L}{V} \tag{2.20}$$

where V is the volume of the simulation box and V_{rod} is the volume of a rod, which we approximate as the volume of a cylinder with length L and diameter r_{b}.

2.5. Sperm Model

Next to the general self-propelled rod we also studied a more detailed sperm model that has been developed by Jens Elgeti [72] and is shown in Fig. 2.4. It consists of a near-spherical head of radius r_{h} formed by usually 163 point particles arranged in a tight mesh that results in a high drag in the surrounding fluid, and a semi-flexible tail formed by three interconnected filaments as shown in Fig. 2.2. Those filaments have a typical length of $L = 100l_{\text{b}}$ to $L = 150l_{\text{b}}$. Harmonic bonds and bending rigidity are implemented similar to the rod model as described in Sec. 2.2. Table 2.2 shows simulation parameters that differ from those used in the rod simulations (Tab. 2.1). Considering a typical swimming speed of $v = 0.01$ [53] and a length scale of $L = 50a$, the Reynolds number for the sperm system is $Re \approx 0.3$.

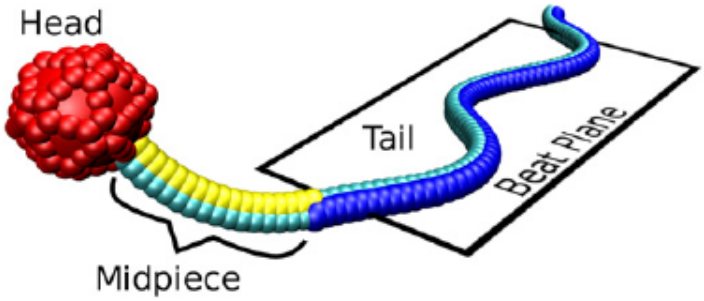

Figure 2.4.: The mid piece curved sperm model consisting of the spherical head (red), the stiff curved mid piece with the shortened filament (2) in yellow and the beating flagellum tail. The filament (1) that is periodically changing its bond length $l_{\mathrm{b}}^{(1)}$ is shown in dark blue. Taken from Ref. [52].

Symbol	Description	Value
Δt_{md}	MD time step	0.0005
Δt_{mpc}	MPC time step	0.05
m_{b}	solute particle mass	5.0
l_{b}	bond length between beads	$0.5a$
r_{h}	sperm head radius	$2.0a$
ω	sperm beat frequency	$0.1\sqrt{k_{\mathrm{b}}T/m_{\mathrm{fl}}a^2}$
A	sperm bending amplitude	$0.1l_{\mathrm{b}}$
k	sperm beat wave number	$0.15/l_{\mathrm{b}}$
η	viscosity of the fluid	$16.67\sqrt{mk_{\mathrm{B}}T}/a^2$

Table 2.2.: Parameters used in the sperm simulations reported in this work, if different from those given in table 2.1.

The first part of the flagellum usually represents the mid piece and therefore is inactive. Bending of the flagellum is achieved by varying the bond lengths $l_\mathrm{b}^{(0)}, l_\mathrm{b}^{(1)}, l_\mathrm{b}^{(2)}$ of the three filaments $(0), (1), (2)$ separately. On the tail part of the flagellum, a sinusoidal beat pattern can be imposed by a periodic local contraction and extension of the bond length $l_\mathrm{b}^{(1)}$ of filament (1) according to

$$l_\mathrm{b}^{(1)}(t, s) = l_\mathrm{b} + A \sin(ks - \omega t + \varphi_0), \tag{2.21}$$

where t is the time, s the linear position along the flagellum, φ_0 the constant phase shift of this particular sperm, A the beat strength (bending amplitude), k the wave number and ω the beat frequency, while $l_\mathrm{b}^{(0)} = l_\mathrm{b}$. Furthermore, spontaneous bending asymmetry can be introduced either in the mid piece (*mid piece curved*, MC) or in the whole flagellum (*tail curved*, TC), achieved by shortening the bond length of filament (2) to $l_\mathrm{b}^{(2)} = l_\mathrm{b} - \Delta l$. This leads to a helical trajectory of the swimming sperm, in contrast to a constant shortening of $l_\mathrm{b}^{(1)}$ (additional to the periodic pattern of Eq. (2.21)) which would only result in swimming in circles. Another important parameter that influences the dynamic distortion is the torsional rigidity of the flagellum, where we differentiate between an elastic (E) and a stiff (S) flagellum.

The propulsion finally results from the flagellum pushing back the surrounding fluid while moving nearly perpendicular to its long axis. A slender rod at low Reynolds number has a perpendicular friction coefficient (see Sec. 1.2.3) $\gamma_\perp = F_\perp / v_\perp$ that is approximately 1.5 to 2 times as high as the friction coefficient $\gamma_\parallel$ parallel to its long axis [27]. The traveling sinusoidal wave pattern in the flagellum therefore pushes back the fluid towards the rear end of the swimmer. Because the passive head drags along the surrounding fluid at the front of the swimmer, the sperm is a pusher. Similar to the rod simulation, hydrodynamic interactions (via MPCD) and excluded-volume interactions between sperm and between sperm and walls are included.

A more detailed description and discussion of this sperm model can be found in Refs. [72, 52]. A slightly modified simulation program written by Jens Elgeti is used for this study.

3. Results

3.1. Single rod

3.1.1. Flow field

As described in section 1.3.2, the far field approximation for the flow field of a swimming self-propelled rod is a force dipole. In the near field the details of the flow field depend on the precise geometry of the swimmer. To visualize the flow field around a single rod the simulation program divides the space around the swimmer in cubic cells and calculates the average velocity of the fluid molecules in these cells. The cell lattice moves (and rotates) with the swimmer with its origin in the center-of-mass of the rod. The problem arising is that small rotational fluctuations of the rod lead to a large displacement of the cell lattice, especially far away from the rod center. The cells therefore sample the velocities of larger areas, resolution is lost. To prevent this, the rod is not freely swimming but guided *on a rail* by strong harmonic potentials in z- and y-direction (see chapter 2.4.1). This way, it is also kept parallel and in constant distance to the wall, if present.

Figure 3.1 shows the flow field around a pusher and a puller moving in positive x-direction in a system without walls. The arrows represent velocities of the fluid with respect to the resting laboratory frame. Because the swimmer exerts no net force on the fluid, no significant global flows arise. There is however a small flow opposed to the rod swimming direction, as during the acceleration the rod gives some momentum to the surrounding fluid. The velocity components are slightly shifted such that the average flow in the observed box is zero in Figs. 3.1 to 3.3. It is clearly visible how the pusher sucks in fluid from above and below and pushes it out at the front and rear ends, and the inverse for the puller.

For comparison, Fig. 3.2 shows the flow field in a similar system with an unpolar rod, which is a self-propelled rod that is driven at every bead of its body, while the total driving force is the same as for the pusher and puller.

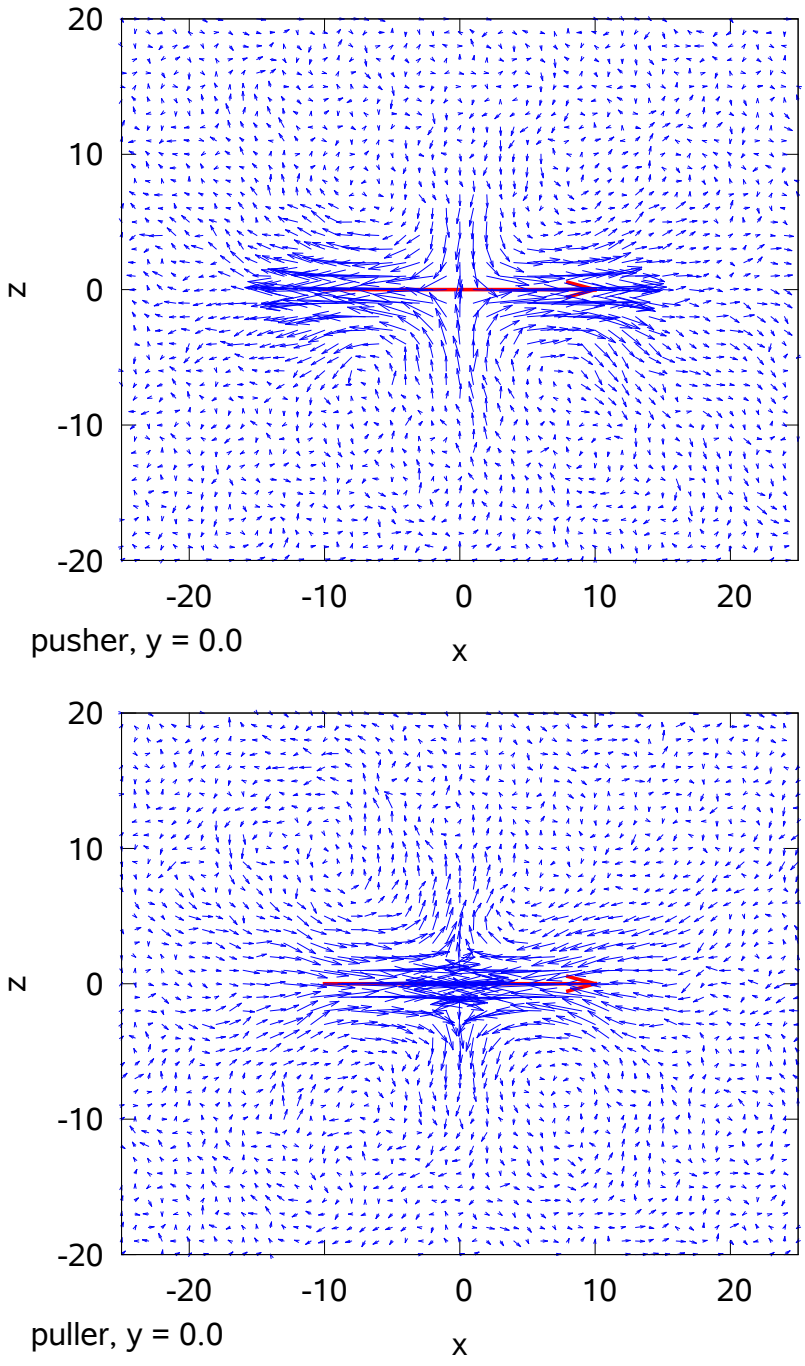

Figure 3.1.: Flow field around single self-propelled rods of different polarity in a system without boundaries. The rod has a length of $L = 20a$ and a propulsion force of $F_{\mathrm{D}} = 600\, k_{\mathrm{B}}T/a$. The lattice constant of the cell grid is $1.0a$. A similar plot for an unpolar swimmer is shown in Fig. 3.2.

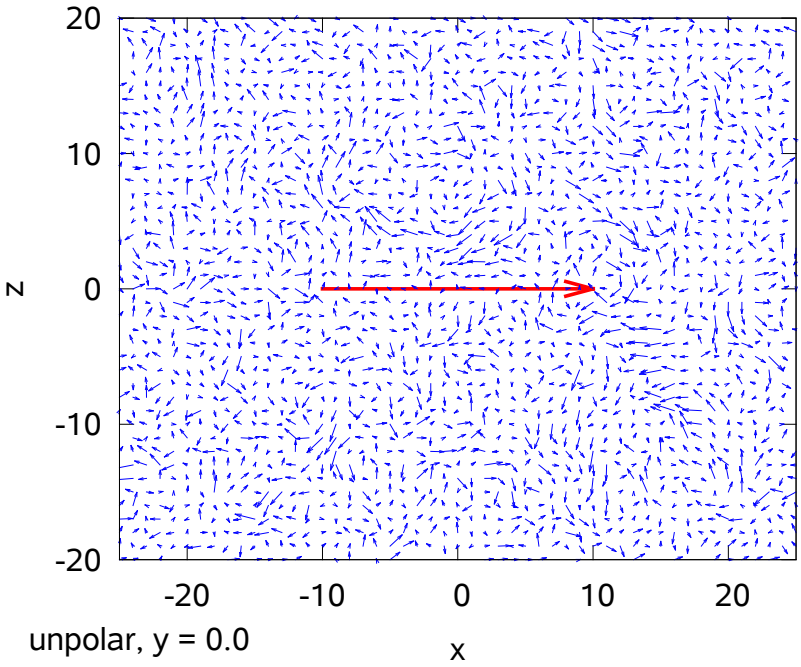

Figure 3.2.: Flow field around a single unpolar self-propelled rod, similar to the system shown in Fig. 3.1. Note: The prefactor for the arrow length here is two times the factor for the plots in Fig. 3.1.

The swimmer does not produce a flow field disturbance that is visible at this signal-to-noise level. Note that to enhance visibility the arrows in Fig. 3.2 have twice the length of arrows in Fig. 3.1 at the same velocity.

Simulations of a rod swimming close to a wall visualize the hydrodynamic interaction with great clarity. Fig. 3.3 shows the flow field around such rods at various view points.

3.1.2. Hydrodynamic interaction with a wall

As described in Sec. 1.3.2 the self-propelled rod hydrodynamically interacts with nearby walls. The expected far-field interaction has been described in Ref. [4], but the analytic dipole approach used here looses validity at wall distances d comparable to or smaller than the rod length L. We performed simulations to measure the attractive / repulsive force between the pusher / puller swimmer and the wall, while the swimmer is aligned parallel to the wall and kept at a constant distance as is described in section 2.4.1. The interaction force according to Eq. (2.19) is very noisy, making necessary a high number of longer runs to get sufficient statistics. Comparing simulations also showed that the data is less noisy for rods consisting of three filaments as shown in Fig. 2.2. Fig 3.4 shows the results for a three-filament pusher rod of length $L = 10$. The simulation results are compared to the predictions of the dipole model, where the dipole force F_{dipole} is calculated by

$$F_{\text{dipole}}(z) = -\gamma_{\perp} v_z(z), \tag{3.1}$$

with $v_z(z)$ as given by Eq. (1.13) and $\gamma_{\perp} = 1577$ is the friction coefficient for this rod moving perpendicular to its long axis. This friction coefficient is determined in simulations where the rod is pulled perpendicular to its long axis through the fluid by a small external force.

While validity of the far-field model is expected for wall distances $d > L$, our data shows good agreement even closer to the wall, for $d/L > 0.5$. This is interesting because in simulations with multiple rods a lot of short range interactions occur, and it is important to know whether the dipole picture can still be employed in their interpretation. The data point closest to the wall in the top plot in Fig. 3.4 describes a rod at a distance to the wall of $d = 1.5$. While the interaction at this scale is not of dipole type, the small error bars and the continuity of the curve confirm that hydrodynamic interactions are still resolved sufficiently well at lengths on the order of a.

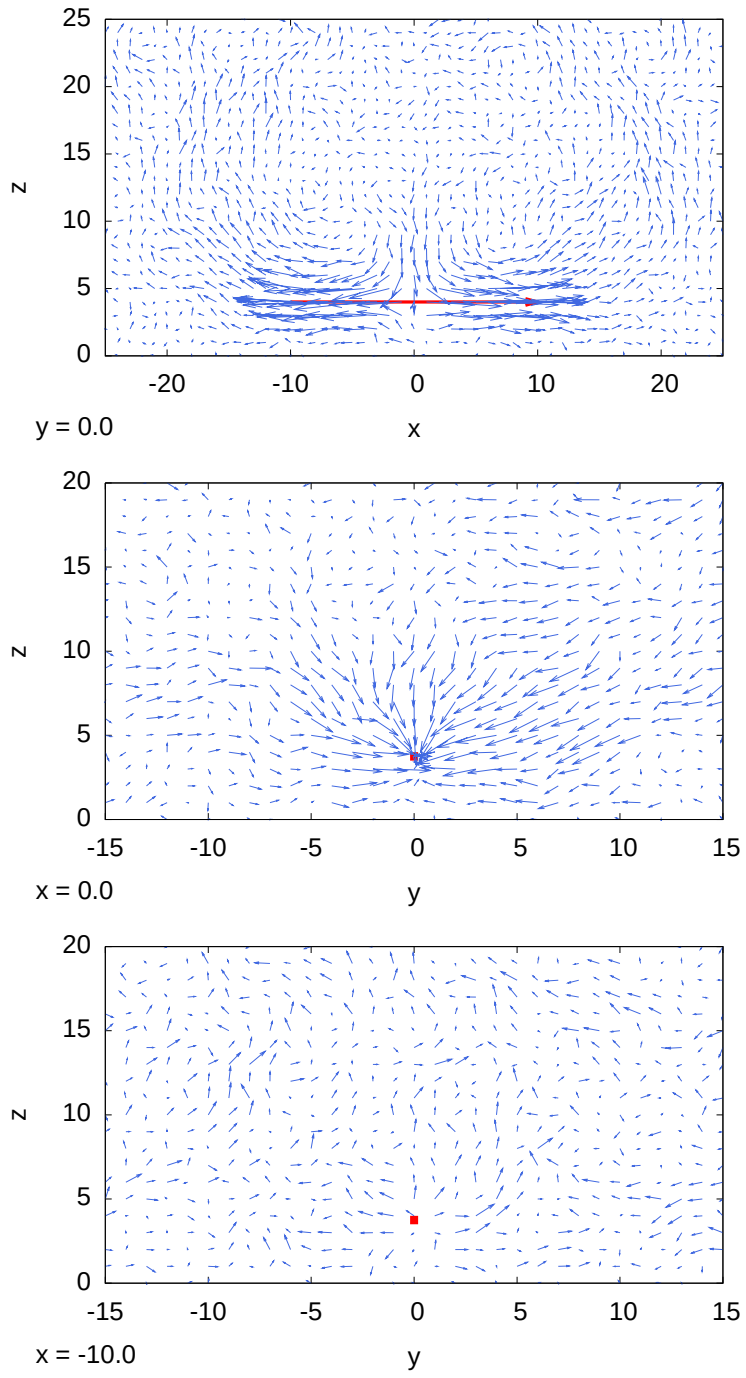

Figure 3.3.: Flow field around a self-propelled pusher rod near a wall. Distance to wall is $d = 4a$, rod length is $L = 20a$, driving force is $F_\mathrm{D} = 600\, k_\mathrm{B}T/a$. The swimmer moves in positive x-direction. Top: the flow field in a plane along the rod. Middle and bottom: plane perpendicular to the rod; in the middle of the rod (middle) and at its rear end (bottom).

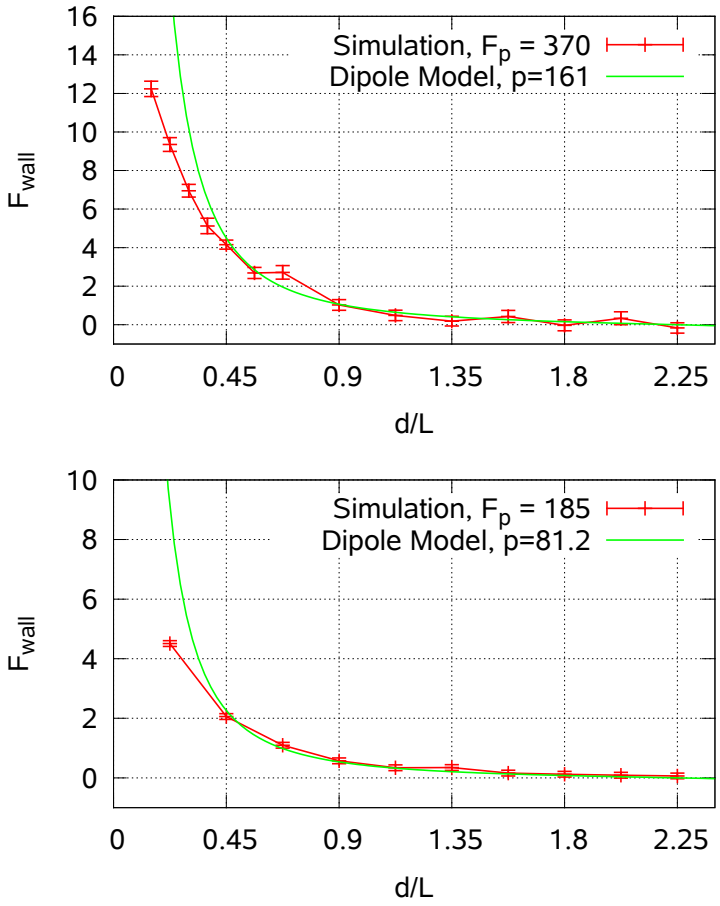

Figure 3.4.: Attractive force F_{wall} between wall and self-propelled pusher rod swimming at constant distance d parallel to the wall. Rod length $L = 10a$. Top: Driving force $F_{\text{D}} = 370\, k_{\text{B}}T/a$, velocity $v = 0.023$ (in the middle of the channel). Bottom: $F_{\text{D}} = 185\, k_{\text{B}}T/a$.

Within limits of the error bars the interaction forces F_{wall} measured in the $F_{\text{D}} = 370\, k_{\text{B}}T/a$ system have twice the magnitude of the forces measured in the $F_{\text{D}} = 185\, k_{\text{B}}T/a$ system. Therefore in this range of swimming velocities the wall attraction scales linearly with driving force. Because of the high computational cost to achieve sufficient statistics in these simulations, we did not study further parameter sets.

3.1.3. Freely swimming rod

The second aspect of swimmer-wall interaction is the volume exclusion, a rod cannot interpenetrate the wall. This effect alone is sufficient for single rods to aggregate near walls, as was shown in Ref. [36]. Still hydrodynamic interactions can support wall adhesion, and the details of the process are highly dependent on the polarity of the swimmer. Wall *adhesion* or *aggregation* means in this context that the swimmer spends a large part of its time very close to a wall. In multi-swimmer systems it means that the average concentration of swimmers is highest close to the walls. A pusher rod is expected to approach the wall in a very flat angle, feeling a torque to align it parallel to the wall and an attractive force towards it, while a puller feels a torque towards perpendicular alignment and a repellent force from the wall in the case of parallel alignment. Because the steric interactions also point towards parallel alignment, the surface aggregation of the pusher is the strongest, compared to puller or unpolar rods, as shown in Fig. 3.5. The wall distance $d \approx 1a$ is the closest the rod can come towards the wall without being repelled by the Lennard-Jones potential. Therefore the pusher spends most of his time directly at the wall, with only little rotational fluctuation. While the unpolar swimmer behaves very similar to the self-propelled rod without hydrodynamics, the puller also shows a strong surface excess, in spite of the seemingly opposite hydrodynamic effects compared to the pusher. An explanation can be found in the average angle between the swimmer and the wall, shown in the bottom plot of Fig. 3.5. The puller feels a torque towards perpendicular alignment. Therefore the rod is inclined towards the wall, leading to a rapid approach at a steeper angle until the front tip hits the wall. Now, the steric interaction turns the rod towards parallel alignment, and both effects form a balance.[1] In the range of distances with the highest

[1] Of course at these small distances, the dipole model is no longer valid quantitatively. The picture of the flow however stays the same: the front tip sucks in the surrounding fluid,

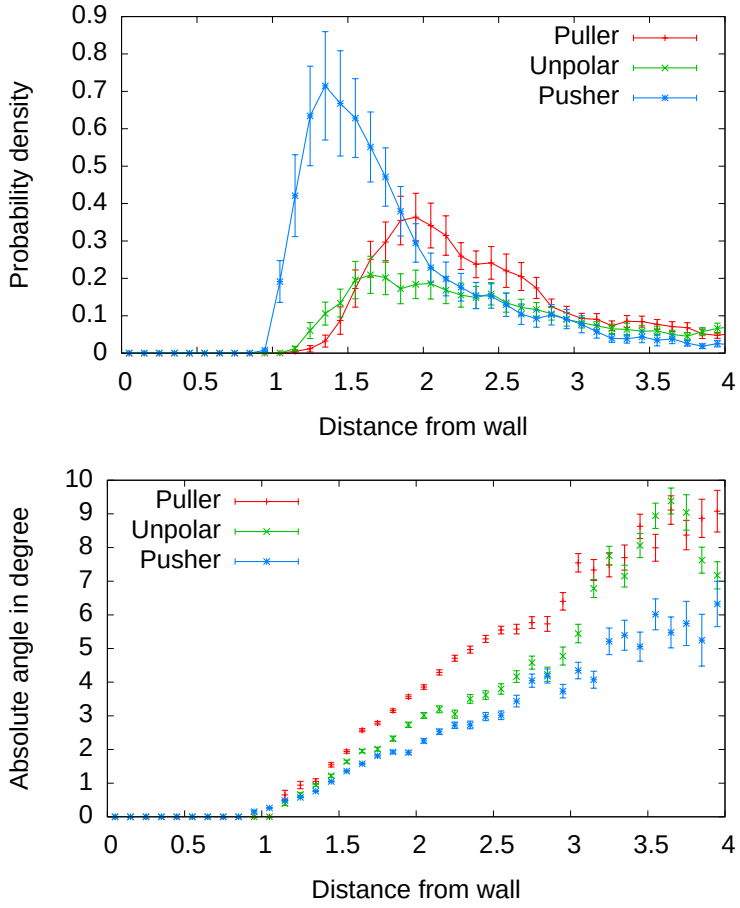

Figure 3.5.: Dynamics of a single freely swimming rod of length $L = 20a$ in a Box of size $60a \times 60a \times 70a$, driving force $F_D = 370\, k_B T/a$, for pusher, puller and unpolar rod. Top: Probability density, normalized such that the area below the curves (over the whole scale $d = 0$ to $d = 35a$) has size 1. Bottom: Distribution of angle between swimmer and wall close to the wall.

puller concentration, $d = 1.6a$ to $d = 2.5a$, with $d = 2.0a$ as its maximum, the inclination angle of the puller is significantly larger than those of pusher or neutral. The propulsion mechanism of the swimmer points along the swimmers axis, therefore the inclined puller always has a positive component of the driving force pointed towards the wall, explaining the aggregation. Furthermore this data confirms the parallel-alignment effect of hydrodynamic interactions of the pusher, as the angle of approach is smaller for the pusher than for the unpolar swimmer.

In Ref. [38] it was observed that in dilute systems without Brownian noise the surface aggregation behavior of swimmers of different polarity with an without hydrodynamic interactions is quite uniform. The hydrodynamic interaction is therefore assumed not to be important in this process. In contrast, our results show that when Brownian noise is accounted for the surface excess is greatly enhanced by the hydrodynamic interactions, because the steric alignment process alone is much weaker under these more realistic conditions.

3.2. Multi-rod systems

To study the behavior of multi-rod systems at different densities, driving forces and swimmer polarities, simulations were performed for the parameter sets shown in Tab. 3.1. The simulations each occupied one GPU (and one CPU) for 300 to 800 hours. For details about the implementation on the GPU platform, see Appendix A.

3.2.1. General behavior

Three-dimensional systems with high densities of self-propelled rods of different polarity interacting via hydrodynamics and volume exclusion are studied.

At high volume fractions, starting conditions become non-trivial. Random placement of rods becomes inefficient, because overlap has to be avoided. To circumvent this problem, we mostly used a simple nematic ordered phase as starting condition: All rods are aligned parallel to the x-axis with random orientation (+x or -x), randomly positioned in x-direction and evenly distributed in y- and z-directions, as can be seen in the top picture in Fig. 3.6.

therefore is attracted towards the wall; the fluid leaves the swimmer in the middle of the rod (as can be seen in Fig. 3.1), pushing it away from the wall.

Volume fraction ϕ, # of rods N_s	Polarity	Run $F_D = 240$	Run $F_D = 320$	Run $F_D = 400$
0.070, 6048	pusher	as1	bs1	cs1
	puller	al1	bl1	cl1
	unpolar	au1 (crashed)	bu1	cu1
0.049, 4232	pusher	as2	bs2	cs2
	puller	al2	bl2	cl2
	unpolar	au2	bu2	cu2
0.037, 3200	pusher	as3	bs3	cs3
	puller	al3	bl3	cl3
	unpolar	au3	bu3	cu3
0.024, 2048	pusher	as4	bs4	cs4
	puller	al4	bl4	cl4
	unpolar	au4	bu4	cu4
swimming velocity v_0		0.0080(3)	0.0103(6)	0.0130(2)
$t_L = L/v_0$		2500	1942	1538

Table 3.1.: The varied parameters for the 36 simulations we ran to study multi-rod behavior. Fixed parameters: $\hat{L} = 20$, box: $120a \times 120a \times 60a$. t_L is the approximate time it takes a single swimmer to swim a distance equal to his own length L. The driving force F_D is always given in units of $k_B T/a$.

The collective behavior of the swimmers is qualitatively different between pushers, pullers and unpolar rods.

Pushers The pusher system quickly looses the nematic order (more details in section 3.2.2 below) of the starting condition by means of a collective motion of a high number of rods with the same orientation, which can be seen in the middle picture in Fig. 3.6. The movement looks like a "V" formed by the collectively reorienting rods and afterwards turns into a large swirl that mixes the solution and destroys the remaining (long-range) order. This development is in good agreement with observations [68] for a similar three-dimensional system of pusher rods, where slender-body theory [23] is employed to calculate hydrodynamic interactions, but volume-exclusion interactions are neglected. After some time, the systems show a flowing, non-jamming state. Small polar clusters form

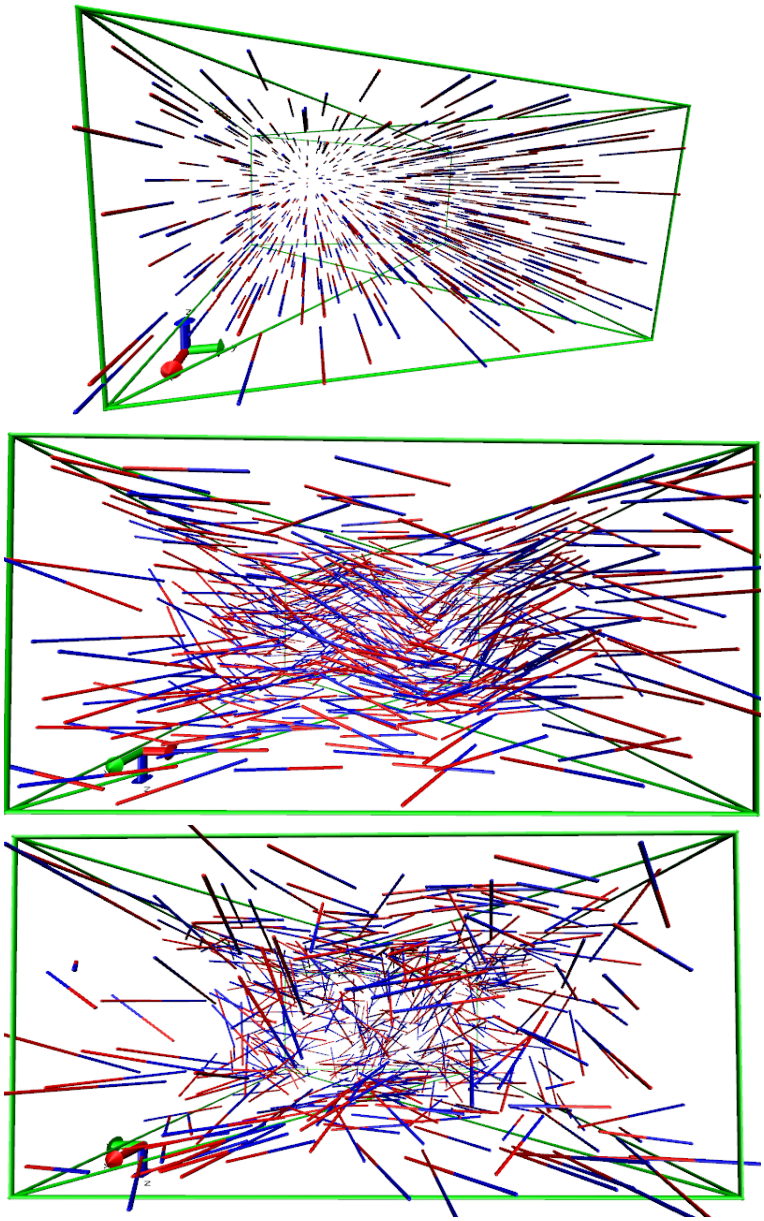

Figure 3.6.: Multi-rod system: $N_s = 6048$ rods of length $L = 20a$ in a box of size $120a \times 120a \times 60a$ (only every 10th rod is shown here). This system contains pusher rods with driving force $F_D = 320$, the passive front part of the rod is shown in red, the active rear in blue. The green box depicts the simulation box with no-slip boundaries at top and bottom and periodic boundary conditions to the sides. Top: the initial condition. Middle: formation of collective motion right after start, at $t = 1100 \,\hat{=}\, 0.6 t_L$. Bottom: the system at about $t = 70000 \,\hat{=}\, 36 t_L$.

temporarily, such as the one that can be seen in the bottom left in the bottom picture of Fig. 3.6. (Please note that in these pictures only every 10th rod is shown, the density is therefore significantly higher in reality.) These polar clusters are highly motile; multiple close rods swimming in the same direction drag along a lot of fluid, resulting in spontaneous local jets and swirls that destabilize or destroy any longer-lasting nematic order in the surrounding. The top picture in Fig. 3.9 shows a layer of rods next to a wall in a high-density pusher system. Some jets and also half-circular structures can be identified. In the dynamics, these form swirls that are strong enough so that rods visibly move in directions different from their orientation $\vec{n}$. The jets are short lived, therefore the local flows do not grow to scales of the whole system (in x or y direction), and we do not expect them to suffer (or be enhanced) from finite size effects. The swirls are not completely confined to the surfaces, they can also be observed in the bulk, as can be seen in the bottom picture in Fig. 3.9. The formation of jets and swirls is in good agreement with the predicted flow instabilities described in Sec. 1.3.5.

Pullers In the beginning there is no collective motion of pullers comparable to the pusher system. The rods start to move (either in $+x$ or $-x$ direction) from their nematically ordered starting positions without significantly changing orientation until they collide with each other. But while the pushers only show loose bonding and small clusters can easily interpenetrate or redirect each other, the pullers quickly form a giant jamming cluster that is at first still spanning the entire linear system size and showing influence of the nematic starting conditions, but then quickly deforms into more random patterns. A typical cluster spanning the system in z-direction (from no-slip wall to wall) can be seen in the two upper pictures in Fig. 3.7. After some time, the rods close to the walls clearly have a tendency to point head first towards the walls (as seen in the bottom picture in Fig. 3.7 and in Fig. 3.10). This phenomenon is sometimes called a *hedgehog cluster*. The rods in the bulk tend to more isotropic orientation. The typical cluster at high volume fraction is jamming, but not completely static. It usually deforms over time, creeps along the surface, sometimes briefly decays into two or more smaller clusters that tend to be more motile and often merge again. At smaller volume fractions the clusters do not span from wall to wall anymore, as can be seen in Fig. 3.8, and typically there are one or two smaller clusters present, instead of a single large one.

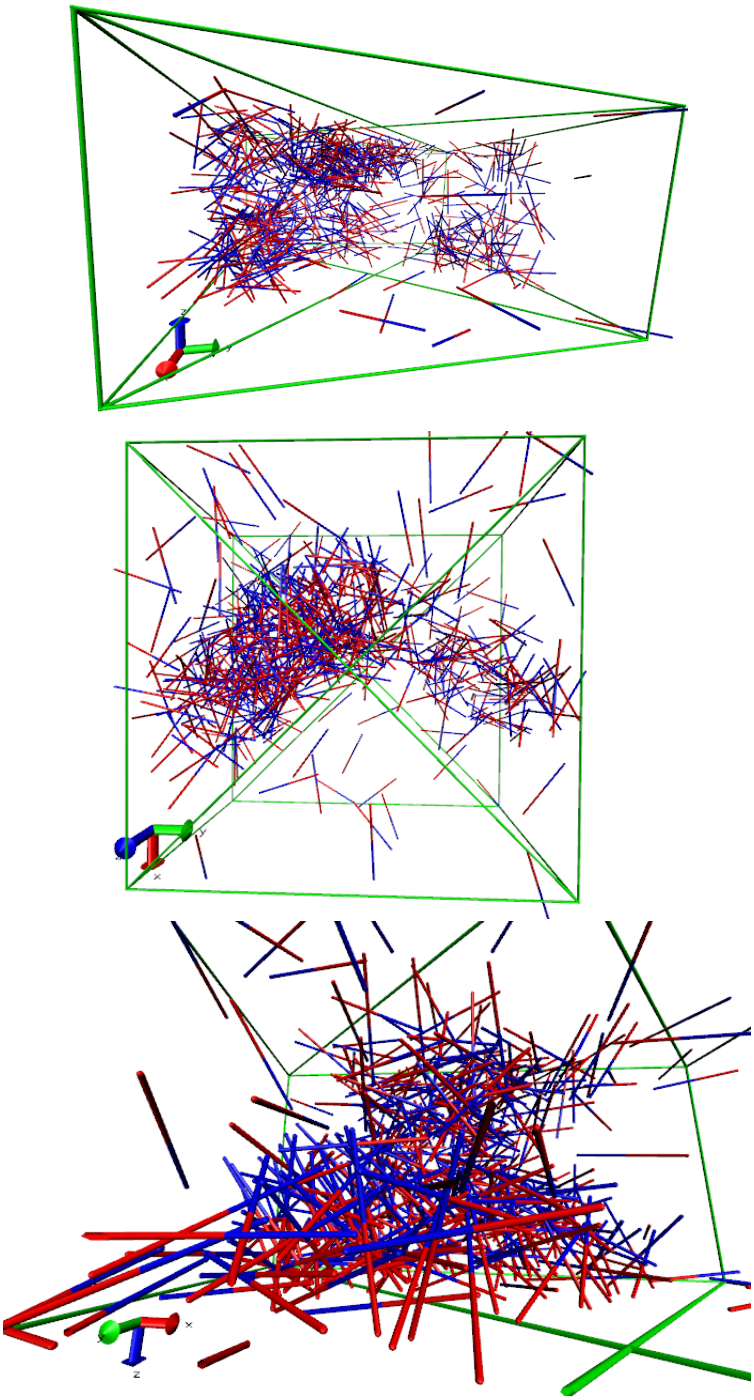

Figure 3.7.: Multi-rod system similar to the one in Fig. 3.6, but with puller rods instead. The active front is red, the passive rear is blue. Top and middle: The system at about $t = 80000 \mathrel{\hat{=}} 41 t_{\mathrm{L}}$ from different perspectives. Bottom: Part of a typical cluster, close to a wall. Directly at the wall, almost all rods point towards the wall.

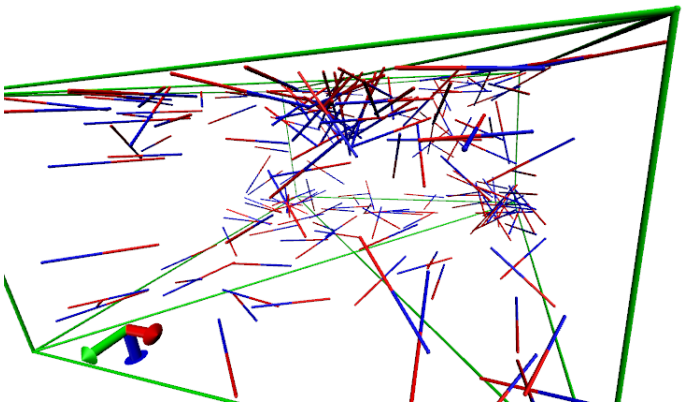

Figure 3.8.: Snapshot of the puller system with $N_s = 2048$ (lowest density) and $F_D = 320$. Two small hedgehog clusters are visible, one at the top and one at the bottom.

Considering whether active fluids of pullers show instabilities as described in Refs. [70, 67] but denied in Ref. [69], we agree with the former. While the excluded-volume interaction in our system plays a significant role in the jamming-cluster formation, the behavior of unpolar driven rods clearly shows that undisturbed flow on the time scale of puller-cluster formation is possible for neutral swimmers. As the swimmer polarity is the only difference between the two systems, the puller fluid has to induce flow defects. Aster-like defects [70], together with the volume-exclusion interaction of the rods are an explanation for the cluster formation. It is however possible that high swimmer densities are required for the formation of flow defects, because as described above and as can be seen in Fig. 3.11, while the pusher system looses its nematic order immediately, the puller system keeps the nematic order while the rods are still (approximately) homogeneously distributed in the system. The collision of the rods moving into opposite directions produces an area of higher density, and this might lead to fluid defects and finally the jamming cluster. Simulations with a polar starting condition might give further information about the criteria for cluster formation.

Neutral As is shown in Fig. 3.2 unpolar swimmers do not produce (significant) disturbances in the surrounding fluid. The hydrodynamic interaction between them therefore is much weaker, leading to longer persistence lengths and a transition to the nematic phase at volume fractions far below the critical density of

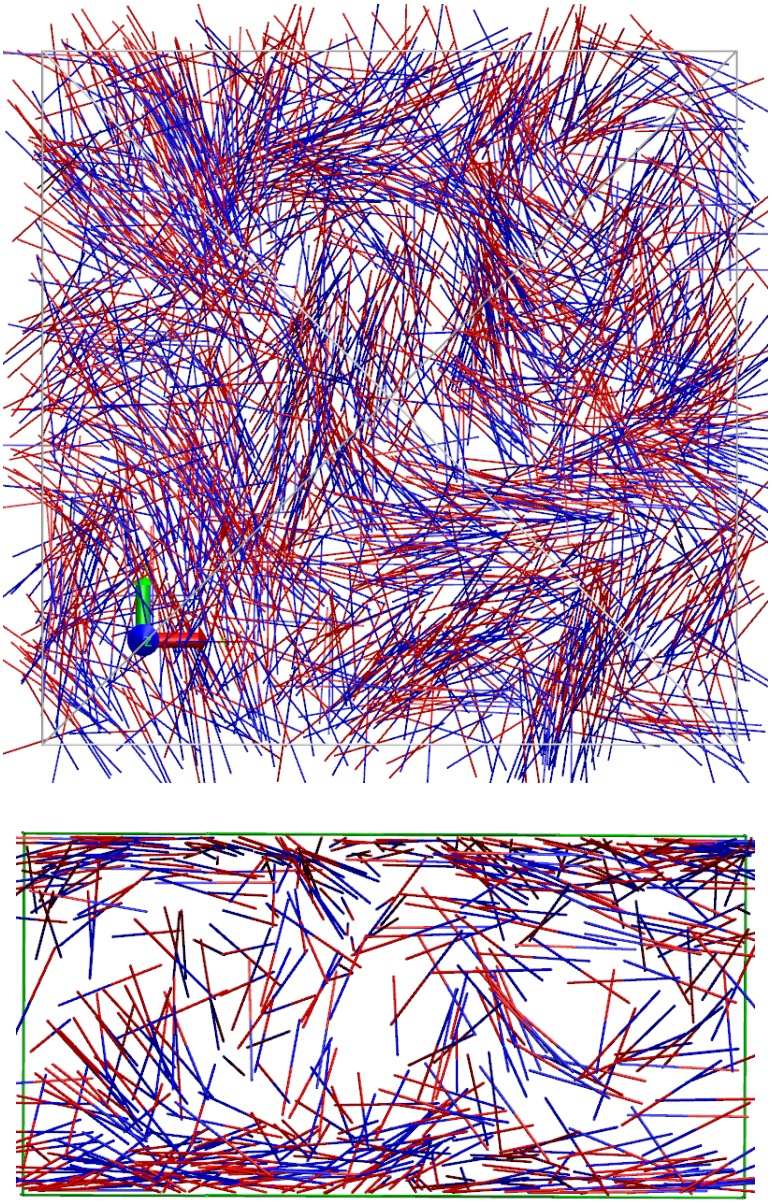

Figure 3.9.: Snapshots of layers of the multi-rod systems with $N_s = 6048$ pushers and $F_D = 400$. The red side of the rods represents the front, the blue side the rear. Within the layers, all rods are drawn (in contrast to Figs. 3.6 to 3.8, where only every 10th rod is drawn). Top: Rods within a distance $d = 10a = L/2$ of a wall. Bottom: Rods in a layer of thickness $10a$ perpendicular to the walls at top and bottom. The layer cuts the top image horizontally in the middle.

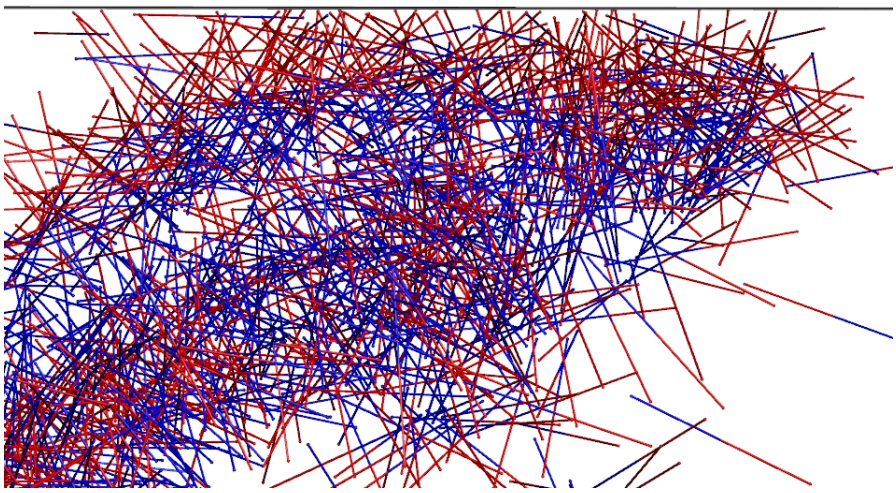

Figure 3.10.: Snapshot of the puller system with $N_\mathrm{s} = 6048$ and $F_\mathrm{D} = 400$. Shown are rods in a layer of thickness $10a$ perpendicular to the wall that is symbolized by the black line at the top of the picture.

passive rods. This will be discussed in Sec. 3.2.8.

3.2.2. Nematic order

The initial state is one of maximal nematic order. To make sure the untypical initial conditions do not influence the observations, we measured the temporal development of the global nematic-order parameter [68],

$$C_\mathrm{nem}(t) = \frac{1}{N_\mathrm{s}(N_\mathrm{s}-1)} \sum_{i \neq j} \frac{1}{2}[3(\vec{n}_i \cdot \vec{n}_j)^2 - 1]. \tag{3.2}$$

Here $\vec{n}_i$ is the normalized orientation of rod i. In the perfectly nematic state $C_\mathrm{nem}(t) = 1$, while in the isotropic state $C_\mathrm{nem}(t)$ fluctuates around 0. The left plot in Fig. 3.11 shows that indeed the phase with residual nematic order is very short compared to the overall simulated time for the polar rods. In the pusher case the nematic order does not drop to the isotropic value of zero because small aligned clusters have a positive contribution and the clusters themselves might even align nematically close to walls. While this could also be a finite-size effect that arises because there are always only a small number of polar clusters present in the system, the slow decay of orientation autocorrelation reported in Sec. 3.2.7 below suggests otherwise. Furthermore a nematic state at high densities has been predicted for pusher systems that include steric interactions [67]. The unpolar

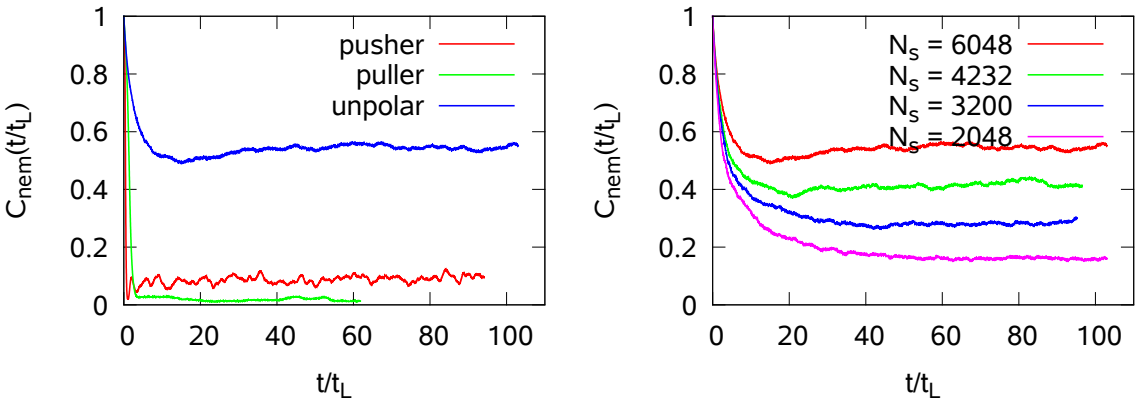

Figure 3.11.: Global nematic order $C_{\mathrm{nem}}(t)$. Left: Rods of different polarity compared for the $N_{\mathrm{s}} = 6048$, $F_{\mathrm{D}} = 320$ systems. Right: Unpolar rods compared for different rod concentrations at $F_{\mathrm{D}} = 320$.

driven rod shows a different behavior. The nematic order does not fall to (near) zero but approaches a constant value depending on the volume fraction and swimming velocity.

3.2.3. Wall aggregation

As we have seen in section 3.1.3 for single swimmers, all three kinds of rods show surface adhesion. Judging from the system snapshots, the pusher system of high density also shows a tendency to surface aggregation. This is confirmed by the density distributions in Fig. 3.12, which show the surface aggregation of pusher and neutral rods for various volume fractions.

However the surface aggregation decreases with increasing rod number, because the denser the walls are populated by swimmers, the stronger the interaction becomes. And while few pushers could align parallel and form motile clusters close to the wall, a higher density leads to too much collisions and disturbing hydrodynamic influence from other, unaligned rods. It has been shown that pusher systems that interact only via hydrodynamics and no volume exclusion also show this phenomenon of decreasing surface excess at high densities [10]. This indicates that hydrodynamic flow defects increasing in intensity at high rod densities are responsible for the drop in surface aggregation. Because surface adhesion still increases slightly with swimming velocity, the hydrody-

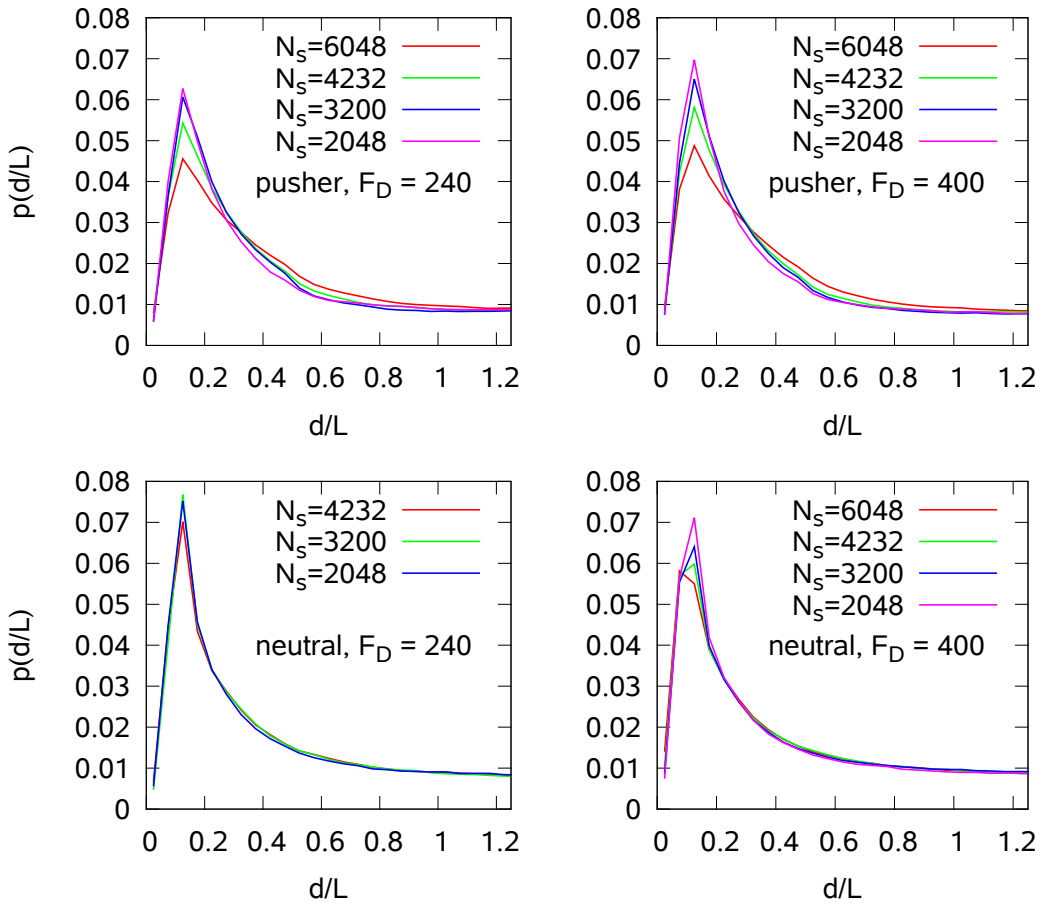

Figure 3.12.: Surface aggregation of pusher and neutral rods of length $L = 20a$ in a box with a wall distance of $60a$ at different rod numbers N_s, polarities and driving forces F_D. Two opposite walls are present in the system, the plots here are averages over the distributions close to both of them. p is a probability density, it has been normalized such that the area below the complete curves from $d = 0$ to $d = 30a = 1.5L$ has size 1. The bin size used in the histograms is $1a$.

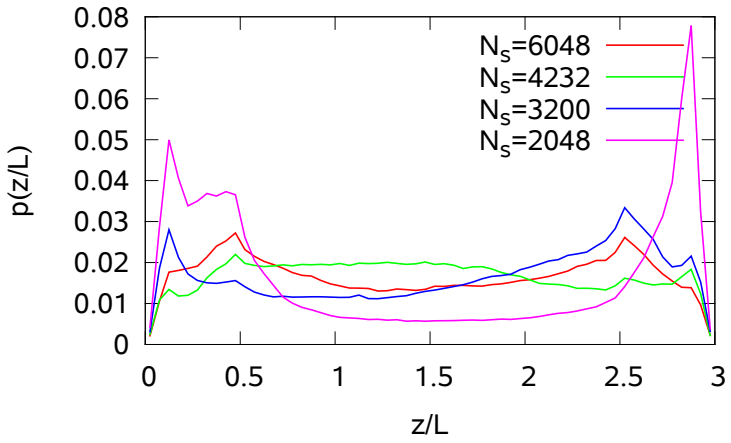

Figure 3.13.: Surface aggregation of puller rods (walls at $z = 0$ and $z = 60a = 3L$): Most rods can be found in the bulk. The reason is the formation of large jamming clusters spanning from wall to wall. The irregular structures of the clusters also lead to the asymmetry of the plot when averaging over our limited simulation times.

namic interaction of the swimmers with the wall still works and competes with the flow field defects.

For the neutral swimmer systems, where strong flow defects are absent, surface adhesion only weakly depends on the density. Hence, excluded-volume interaction among the rods does not have a strong effect on the adhesion at the densities studied. For single swimmers interacting only via excluded volume, the swimming velocity does not influence surface adhesion [36]. In spite of this, the bottom right plot in Fig. 3.12 shows that the adhesion slightly decreases with swimming velocity, especially for higher densities. The reason might be a higher rod-rod collision rate at higher velocities and densities.

The surface adhesion also decreases with increasing volume fraction in low-density puller systems.The slow jamming-cluster dynamics only provides a few slowly deforming cluster configurations in the typical runtime of our simulations, by far no representative sample of the whole phase space. Therefore the histogram in Fig. 3.13 is rather irregular and not symmetric.

3.2.4. Angle of approach

Fig. 3.14 shows the average angle $\langle\theta\rangle$ between swimmers and the wall as a function of distance d to the wall. The angle a rod would have at distance d if it directly touches the wall is given by $\theta_{\max}(d) = \arcsin(2(d - d_{\mathrm{LJ}})/L)$, where d_{LJ} is the range of the repulsive wall potential. Due to the higher number of samples compared to the single-rod simulations, the plots look smooth even for larger distances from the wall. Note however the large error bars that show half the standard deviation of the sample. The angle of approach is not very sensitive to parameters like the density (compare the two plots in Fig. 3.14) or driving force (not shown here). The peak near $d = 10a$ represents the distance above which the rod cannot touch the wall anymore. Left of the peak there are still some rods pointing towards the wall in a very steep angle touching the wall (the hedgehog clusters of the puller configurations are made from these); these rods increase the average. At $d > L/2$ there are no such contributions anymore, therefore the average decreases.

In contrast to the dilute case, in the multi-rod system the pushers display a larger average angle to the walls than the neutral swimmers. We attribute this to the flow defects, e.g. swirls in the fluid induced by pushers at high densities.

3.2.5. Cluster-size analysis

The most surprising phenomenon of the multi-rod system is the formation of large clusters by the puller rods. To analyze cluster formation and size distribution, we define two rods to belong to the same cluster if any of their beads are closer to each other than $d_{\max} = 1.3a$ and the angle between their orientations is not bigger than 35°. At this distance, beads do not touch yet (they do at a distance of $r_{\mathrm{b}} = 0.8a$), but they strongly feel the others hydrodynamic influence. The angular criterion ensures that rods that are passing by each other in opposite direction, and therefore are close only for a very short time, are not considered to belong to the same cluster. The latter case is quite unlikely for clustering puller systems, and the cluster-size distributions are not changed qualitatively for the puller by the additional orientation constraint. For the pusher and especially the neutral swimmer on the other side there is a significant difference, as is demonstrated below.

Fig. 3.15 shows the cluster-size distribution for swimmers with driving force $F_{\mathrm{D}} = 320$ in the $N_{\mathrm{s}} = 6046$ system at different polarities. The averages are

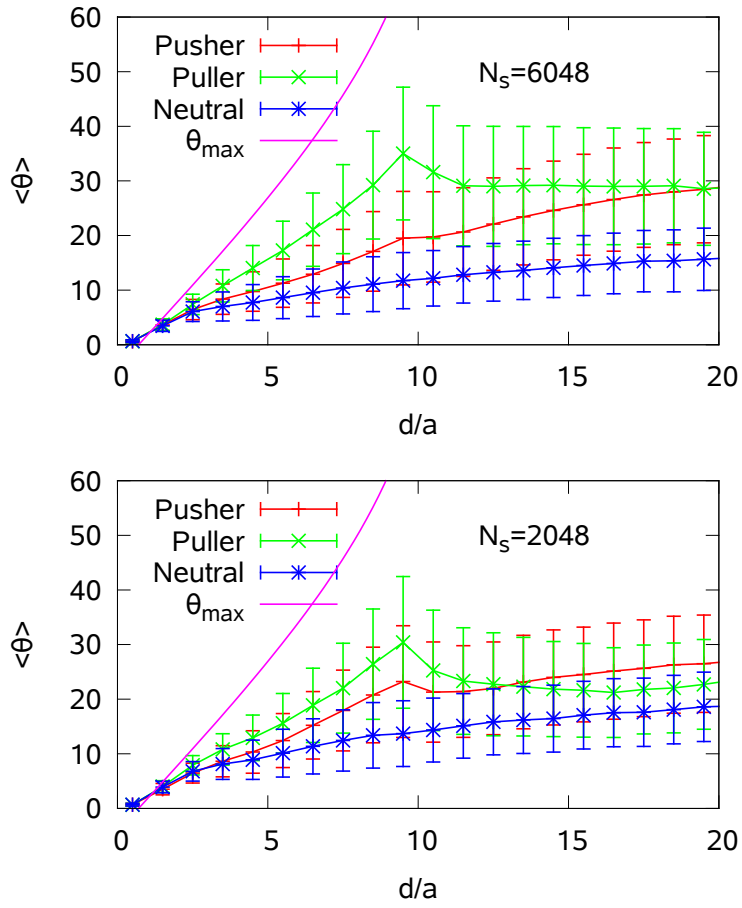

Figure 3.14.: Average angle θ between swimmers of length $L = 20a$ and the wall as a function of distance d of the swimmers center of mass from the wall. Shown is data from simulations with driving force $F_{\mathrm{D}} = 320$ and rod numbers $N_{\mathrm{s}} = 6048$ and $N_{\mathrm{s}} = 2048$. θ_{max} is the maximal possible angle due to volume exclusion. Error bars show half the standard deviation of the sample.

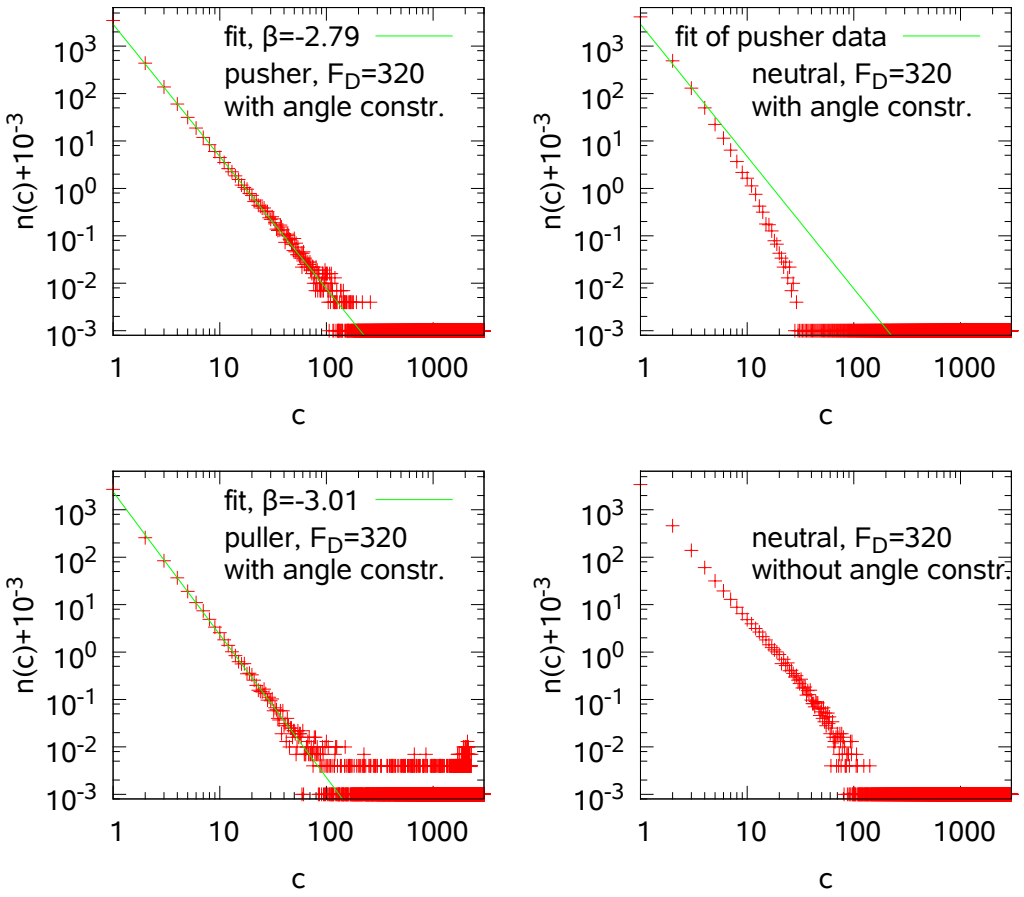

Figure 3.15.: Cluster-size distributions for swimmers with driving force $F_\mathrm{D} = 320$ in the $N_\mathrm{s} = 6048$ system at different polarities. $n(c)$ is the number of occurrences of clusters of size c averaged over 334 snapshots of the system within a time span of 40000 time units ($\hat{=}21t_\mathrm{L}$). The $n(c)$-axis is shifted by $+10^{-3}$ in order to make the zero-counts visible on the logarithmic scale. In the case of the graph in the bottom right the orientation of swimmers is not considered when deciding whether they belong to the same cluster (see text). β is the exponent of the power-law fit of the pusher and puller up to a cluster size of $c = 30$.

calculated from 334 time frames out of an interval of 40000 time units, and have been shifted by $+10^{-3}$ in order to make the zero counts visible. Additionally, the average cluster sizes have been plotted for all pusher and puller system in Fig. 3.16. The difference in the cluster-size distribution between the swimmers is eye catching. Both, pushers and pullers, follow a power law for smaller clusters. The exponent of the fit of the cluster-size distribution up to a cluster size of 30 is $\beta = -2.79$ for the pusher and $\beta = -3.01$ for the puller. The neutrally driven rod on the other hand shows a cluster-size distribution with an exponential decay, a fact that could be overlooked if the clustering rule without the orientation constraint was employed, as can be seen in the bottom right of Fig. 3.15. In that case, rods that pass by each other very closely would be interpreted as forming a cluster. (This could also be counteracted by lowering the maximum distance $d_{\max} = 1.3$ to e.g. $d_{\max} = 1.0$, but at this value the large jamming clusters of the puller systems are not recognized anymore by the algorithm.)

Towards larger clusters $c \gtrsim 100$ the distribution for the pusher shows a slight tail, but clusters larger than 200 rods are extremely rare. For the pullers this large-cluster tail contains a significant portion of the rods[2]. Furthermore the cluster-size distribution is not continuously decaying, but has a small peak for clusters of maximum size. Fig. 3.17 shows this increase in a linear plot with the data strongly smoothed (by averaging every data point over the neighboring 100 data points) for better visibility. The last peak can be fitted well by a Gaussian distribution around $c_{\text{peak}} = 2210$, which points towards a dynamic equilibrium state where for a significant time during the 40000 time units there was a single large cluster fluctuating around the size of 2210 rods. The time it takes the high-density puller system to completely decorrelate after a large cluster has been formed is too long to create sufficient statistics to judge whether this is a typical cluster size. In Fig. 3.16 the average cluster sizes are compared among all pusher and puller systems. The influence of rod density on the cluster size is much stronger than the influence of the driving force F_{D}, although an increase of cluster size with F_{D} is clearly visible. The top picture in Fig. 3.9 shows a layer of rods next to a wall in a high-density pusher system. Due to the

[2]Note that the scale at the lower end of $n(c)$ is discreet, meaning the points at $4{\cdot}10^{-3}$ represent events where one such cluster has been found among the 334 studied time frames. As there can only be one or two large clusters per time frame and there is one data point for each cluster size, it is highly probable to count none or a single occurrence of a certain cluster size within the 334 time frames.

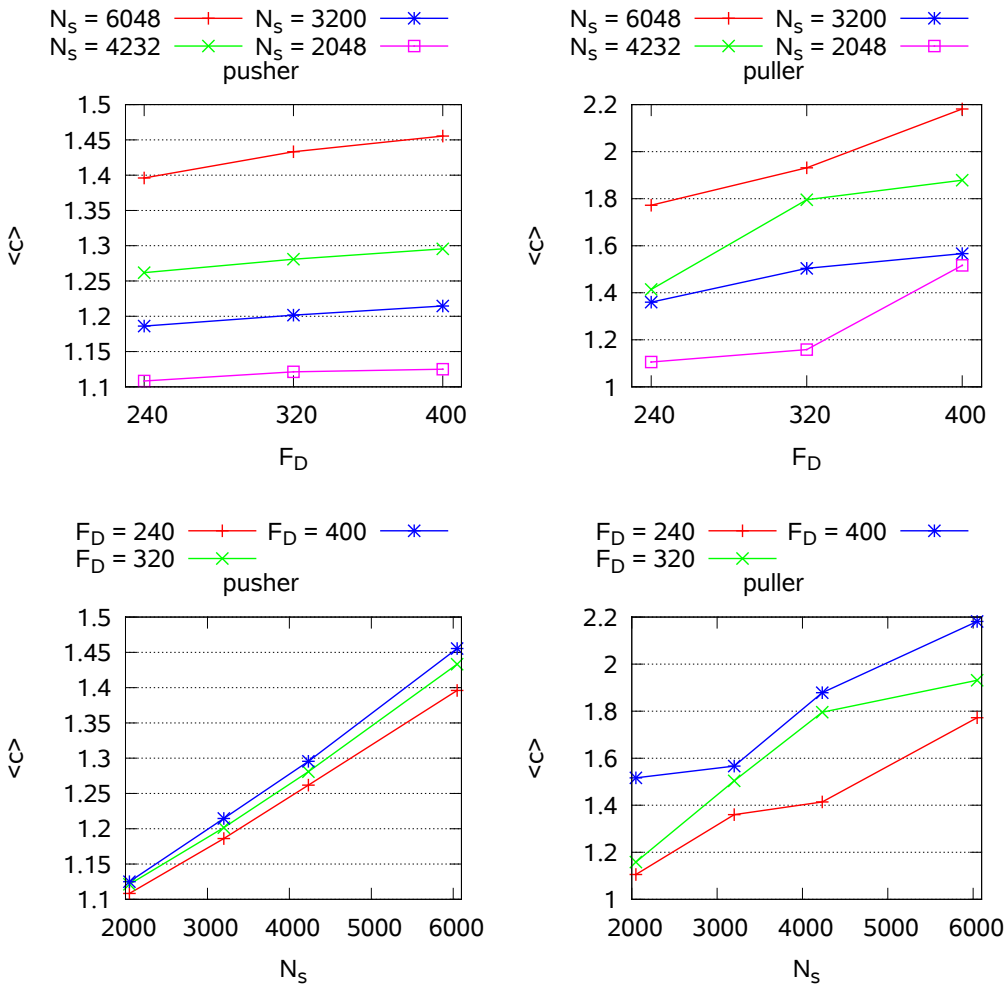

Figure 3.16.: Average cluster size $\langle c \rangle$ of all pusher (left) and puller (right) systems, depending on driving force F_D (top) and number of rods N_s (bottom). The average of the puller system shows strong scatter because per data point plotted here only one simulation run was used, and the jamming-cluster dynamics of the puller systems are too slow to produce sufficiently many independent configurations.

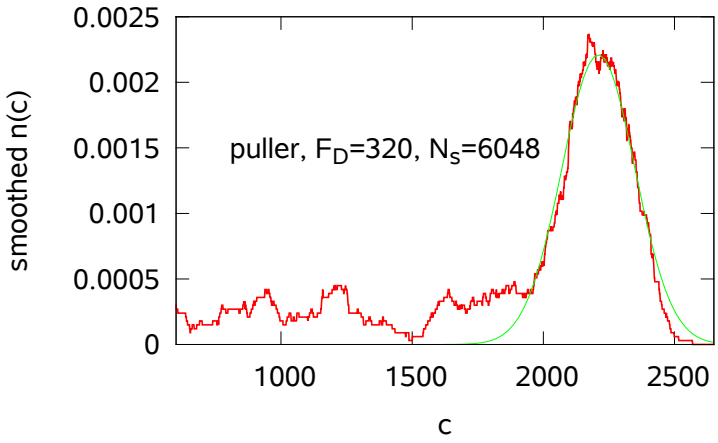

Figure 3.17.: Large-cluster end of the cluster-size distribution of the puller system in a linear plot. The curve is strongly smoothed out (every data point is averaged over the neighboring 100 data points). The Gaussian fit of the peak has the mean $c_{\mathrm{peak}} = 2210$.

concentration profile, the density close to the walls is significantly increased, and the packing of the rods might be dense enough that several smaller clusters or jets are recognized by the algorithm as (transient) super clusters.

To simplify the comparison of the clustering behavior of the various puller systems, we calculate the average percentage of rods $p^{>}(c)$ that are part of a cluster of size c or bigger. The result is shown in Fig. 3.18. We also rescaled the cluster size c with the total number of rods in the system N_{s}, such that $c/N_{\mathrm{s}} = 1$ describes one large cluster that contains all rods in the system. All of the curves show a quick drop at $c = 2$, even at the highest density and driving force still about 40% of the rods are not part of any cluster. Another 20% are distributed on clusters of sizes up to $c = 15$ in this case, but then there follows almost a plateau. Most of the systems show a more or less distinct plateau in $p^{>}(c)$ after the fast drop. Considering that in these plots, the negative slope is proportional to the number of rods in clusters of the given size, this shows that the (puller) systems have

- a very high number of small clusters up to sizes of the order of $c = 2$ to $c = 10$,
- relatively few clusters of medium size (the plateau in Fig. 3.18, the power

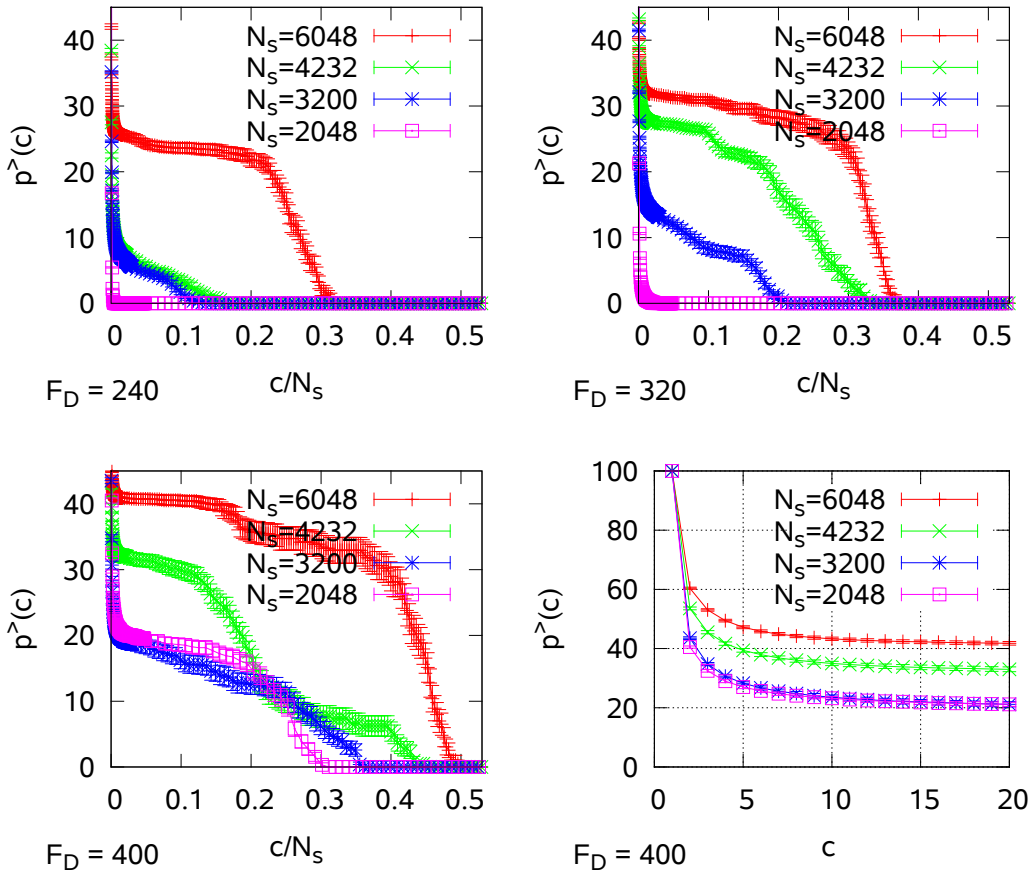

Figure 3.18.: The average percentage of puller rods $p^{>}(c)$ that are part of a cluster of size c or bigger. In the first three graphs, the cluster size c has been normalized with the total number of rods in the system N_s. Hence, the largest possible cluster has $c/N_\mathrm{s} = 1$.

law in Fig. 3.15)

- a very large cluster (the peak in Fig. 3.17) that contains, due to its size, a large proportion of all rods (the steep decay after the plateaus in Fig. 3.18).

We have to emphasize however that each curve in Fig. 3.18 represents a single simulation run, analyzing only a few completely independent conformations each. Therefore the position of the transition from the plateau to the steeper decay could (and probably does) vary strongly among independent systems of the same parameters. This is also underlined by the fact that curves not always appear *in the right order* in the graphs, e.g. in the bottom-left graph the curves sometimes cross.

3.2.6. Spatial correlation of orientation

We analyze the spatial correlation of orientation for the different swimmer types. Fig. 3.19 shows polar and nematic correlation functions. Due to the presence of walls in the system, the symmetry is broken in z-direction, therefore we only compare the correlation of rods within a fluid layer of (approximately) constant distance to a wall. More precisely, the box is divided into ten layers of thickness $6a$, and only the rods within a certain layer are compared. In Fig. 3.19 *close to wall* means rods in layers 2 and 9, *mid-channel* means rods in layers 5 and 6. The polar correlation $C_{\mathrm{pol}}(z,r)$ differentiates between rods with orientation $\vec{n}_i$ swimming in the same direction and rods swimming in opposite directions [68]:

$$
\begin{aligned}
C_{\mathrm{pol}}(z,r) &= \frac{\left\langle \sum_{i\neq j} (\vec{n}_i \cdot \vec{n}_j)\, \sigma_{i,j}(z,r) \right\rangle_t}{\left\langle \sum_{i\neq j} \sigma_{i,j}(z,r) \right\rangle_t} \qquad (3.3)\\
\text{with} \quad \sigma_{i,j}(z,r) &= \delta(|x_i - x_j| - r)\, \delta(z_i - z)\, \delta(z_j - z)\\
\text{and} \quad \delta(x) &= \begin{cases} 1 & \text{for } |x| < \frac{1}{2} \cdot \text{bin size} \\ 0 & \text{else} \end{cases}
\end{aligned}
$$

Two parallel rods swimming in the same direction yield a correlation of $C_{\mathrm{pol}}(z,r) = 1.0$, rods swimming in opposite directions yield $C_{\mathrm{pol}}(z,r) = -1.0$ and two perpendicular rods yield $C_{\mathrm{pol}}(z,r) = 0$. The polar correlation of a high number of arbitrarily distributed (and oriented) rods (an isotropic system) fluctuates around zero.

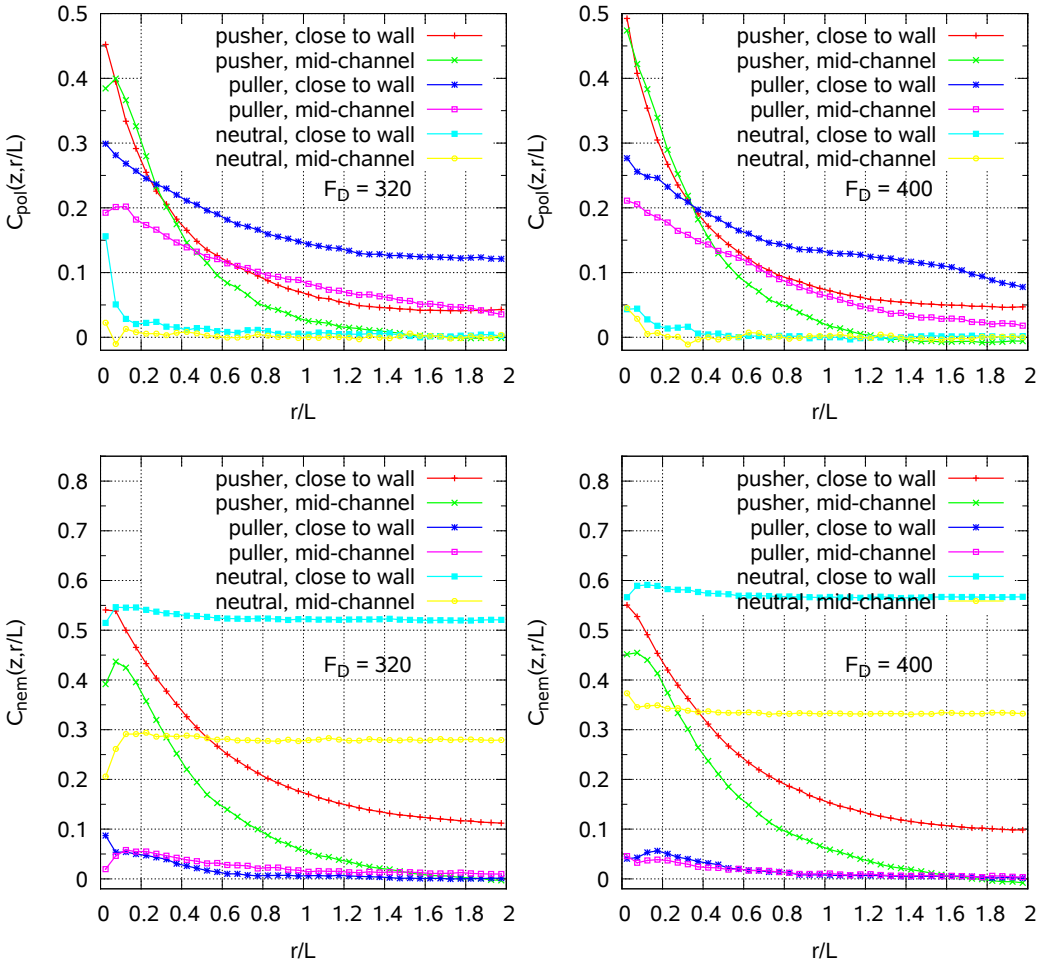

Figure 3.19.: Polar $C_{\mathrm{pol}}(z,r)$ and nematic $C_{\mathrm{nem}}(z,r)$ radial correlation function for rods of length $L = 20a$ in the system with $N_{\mathrm{s}} = 6048$ rods for two different driving forces F_{D} and all three polarities. The rods are either located close to a wall (wall distance $6a$ to $12a$) or in the middle of the channel (wall distance $24a$ to $30a$). (Note that the data points at minimum r are generated from very few rods, leading to stronger scattering.)

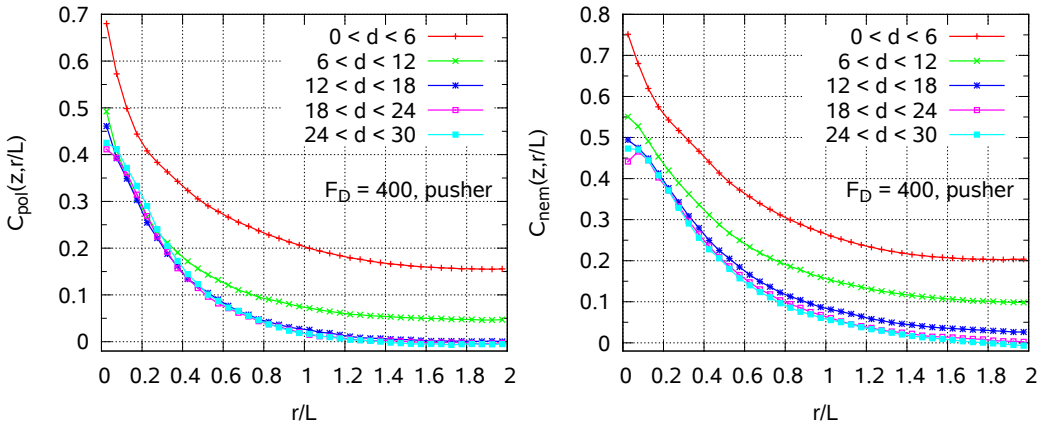

Figure 3.20.: $C_{\mathrm{pol}}(z,r)$ and $C_{\mathrm{nem}}(z,r)$ for pusher rods with driving force $F_{\mathrm{D}} = 400$ in layers with a certain wall distance d. The distance between the walls is $60a$.

The nematic correlation is similar to the nematic order parameter from Eq. (3.2), it treats parallel and anti-parallel rods equally:

$$C_{\mathrm{nem}}(z,r) = \frac{\left\langle \sum_{i \neq j} \frac{1}{2}[3(\vec{n}_i \cdot \vec{n}_j)^2 - 1]\, \sigma_{i,j}(z,r) \right\rangle_t}{\left\langle \sum_{i \neq j} \sigma_{i,j}(z,r) \right\rangle_t} \tag{3.4}$$

In the nematic case (all rods parallel or anti-parallel) it is $C_{\mathrm{nem}}(z,r) = 1.0$, in the isotropic case it fluctuates around zero.

The top plots in Fig. 3.19 show $C_{\mathrm{pol}}(z,r)$ for z values close to the wall or in the bulk. Near the walls the pusher rods display the highest polar correlation. This confirms that the medium-size motile pusher clusters (shown in the top left plot of Fig. 3.15) are indeed polar swarms or jets of rods swimming together, instead of jamming clusters. Several polar swarms can be distinguished in the top picture in Fig. 3.9, which shows a snapshot of a slice next to a wall of a high-density pusher system. Fig. 3.20 shows the correlation functions for pushers depending on the distance to the walls. The fast correlation decay to zero in the bulk indicates that on a global scale the system is isotropic in the bulk (as can also be seen in the bottom picture of Fig. 3.9), which means that swarms do not align with each other in the bulk. Near the walls this behavior is slightly changed. Even in systems with a high volume fraction pushers experience confinement by

the walls (see Sec. 3.2.3), resulting in behavior more similar to a two-dimensional system. There, due to a high collision rate and a lack of space to avoid each other, clusters show a tendency to mutual nematic alignment [94], or formation of longer nematic jets. This conclusion is supported by the fact that the correlation is positive even on a system-wide scale, as indicated by the left plot in Fig. 3.11.

The pullers show a less pronounced polar and especially nematic correlation for short distances, not forming swarming clusters. However close to the walls hedgehog clusters increase the polar correlation, indicating that they are a common phenomenon[3]. Fig. 3.10 shows such a hedgehog cluster. In this case of a very large cluster, the hedgehog part does not form the whole cluster but is merely the interface between the bulk cluster and the wall. The observation that pullers show positive nematic order contradicts reports by Saintillan and Shelley [68], where nematic correlation was considered to be slightly negative for pullers at close range. However Saintillan and Shelley neglect volume-exclusion interactions in their simulations, what should lead to completely different dynamics in the system without the formation of any jamming clusters.

For the neutrally driven rods finally, the polar correlation fluctuates around zero as the initial condition for all systems has a local and global polar order of zero, and the swimmers do mainly align only by excluded-volume effects that are rather weak in three dimensions and furthermore do not differentiate between rods swimming in the same or opposite directions. The nematic correlation on the other hand is close to the wall the highest of all swimmers, independent of range and constant over time (see Sec. 3.2.2). These observations will receive further discussion in Sec. 3.2.8.

3.2.7. Persistence time

The trajectory of a single rod-like swimmer in a system without walls is similar to the structure of a polymer described by the worm-like chain model. At distances x far below the persistence length ξ_p, the trajectory of the swimmer is directional, while at much larger distances $x \gg \xi_\mathrm{p}$, the trajectory can be

[3]While hedgehog clusters increase the polar correlation, this is not the case for the nematic correlation. The reason is that in a hedgehog cluster, the rods are not parallel but inclined towards each other, with a preference for a common orientation. This can also be seen in Fig. 3.10. The deviations in orientation have a stronger effect on the nematic order than on the polar order due to the quadratic term in Eq. (3.4) and the fact that perpendicular rods (that may exist on opposite sides of hedgehog clusters) yield a negative contribution.

considered as a random walk[4] [95]. As we want to compare swimmers with different swimming velocities, we choose the persistence time τ as a criterion, instead of the persistence length. With the assumption that the non-jamming rods swim with constant velocity v_0, it is $\tau = \xi_\mathrm{p}/v_0$. The persistence time τ can be defined using the autocorrelation function of the orientation vector $\vec{n}_i$:

$$C_{\vec{n}}(t) = \left\langle \langle \vec{n}_i(t_0) \cdot \vec{n}_i(t_0 + t) \rangle_{t_0} \right\rangle_i \tag{3.5}$$

The autocorrelation function is expected to decay exponentially with t for large times:

$$C_{\vec{n}}(t) = A_\mathrm{C}\, e^{-t/\tau} \tag{3.6}$$

Fig. 3.21 shows the decay of the correlation function $C_{\vec{n}}(t)$ for all pusher systems. At very short times the function deviates from an exponential curve, it decays slower (see top right graph of Fig. 3.21). We attribute this to the formation of small- to medium-size clusters, stabilizing short term behavior by excluded-volume interaction.

The curves in Fig. 3.21 are each fitted with two different persistence times τ_1 for small t and τ_2 for large t, with $\tau_2 > \tau_1$. For even larger t the autocorrelation functions show unpredictable oscillations that seem to be artifacts of finite system size and finite measuring time. The persistence times τ_1 and τ_2 are shown in Fig. 3.22 (top left and bottom graph). This two-step dynamics is a result of polar cluster formation. Persistence time τ_1 describes the reorientation of the single rods, the larger τ_2 describes the reorientation of the clusters.

τ_1 decreases with higher rod density and stronger driving force. This dependence on rod density is to be expected qualitatively, as collision frequency increases with N_s. In order to judge the dependence on the driving force, we approximate the swimming velocity of the rods as v_0, the swimming velocity of single rods, as given in Tab. 3.1 (although this is clearly an inaccurate approximation). Using this, the top right graph in Fig. 3.22 shows the persistence length $\xi_\mathrm{p} = \tau/t_\mathrm{L}$ (in units of L). It is independent of the driving force F_D. (The small deviations might result from the rather crude approximation of the swimming velocity.) The graph also displays a fit of the persistence length $\xi_\mathrm{p} = c_\mathrm{cs}/N_\mathrm{s}$ of the $F_\mathrm{D} = 400$ system, with fit constant $c_\mathrm{cs} = 11800(260)$. For the largest rod density the fit deviates; to determine the functional dependence of the cluster size on the rod density, more data points at high densities are necessary.

[4]For the polymer in the worm-like chain model, the tangential vectors along the polymer correspond to the orientation vectors along the swimmer trajectory.

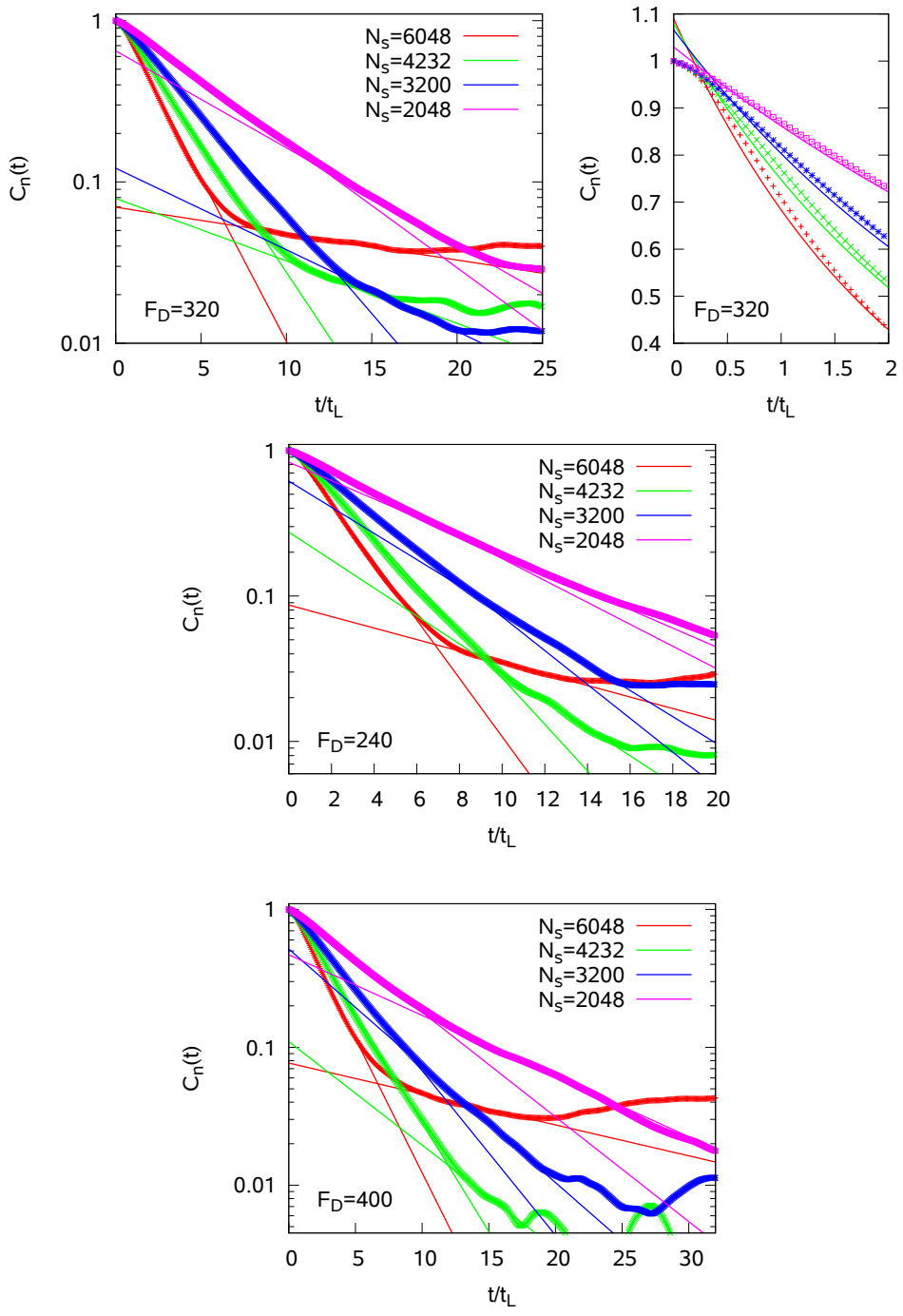

Figure 3.21.: The autocorrelation function $C_{\vec{n}}(t)$ for all pusher systems. Each function displays two regimes of decay, both are separately fitted with Eq. (3.6). The top right graph is a linear enlargement of the small-t part of the top left graph.

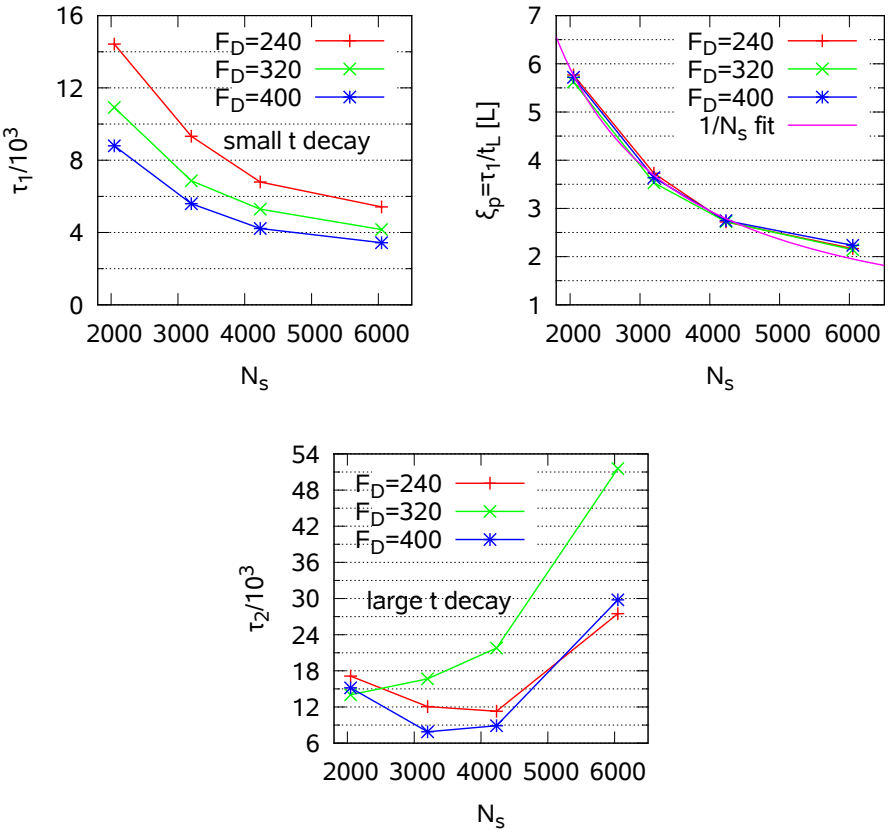

Figure 3.22.: The persistence times $\tau_{1,2}$ for all pusher systems, determined by the exponential fits shown in Fig. 3.21. Errors in the top graphs are on the order of the symbol size. Top left: Persistence times τ_1 for small t. Top right: Persistence times for small t rescaled with the time t_L it takes a single rod to swim its own length. Assuming in the multi-rod system all rods swim with the same velocity v_0 as rods in the dilute case, $\xi_\mathrm{p} = t/t_\mathrm{L}$ is the persistence length. Bottom: Persistence times τ_2 for large t. Errors are much larger than symbol sizes, but hard to estimate due to various contributions.

Volume fraction ϕ, # of rods N_s	Run $F_D = 150$	Run $F_D = 200$	Run $F_D = 250$
0.024, 1024	A1	B1	C1
0.037, 1600	A2	B2	C2
0.049, 2116	A3	B3	C3
0.068, 2916	A4	B4	C4
0.078, 3364	A5	B5	C5
0.089, 3844	A6	B6	C6
swimming velocity v_0	0.0111(3)	0.0142(3)	0.0184(3)
$t_L = L/v_0$	901	704	543

Table 3.2.: The 18 runs with neutrally driven rods used to study the isotropic-nematic transition.

The persistence times τ_2 for the cluster dynamics are not continuous. They drop at intermediate rod densities and increase strongly at high densities. The error of τ_2 is quite large, as it strongly depends on the range of the decay we assign to the second regime. It is also not clear why the $F_D = 320$ system shows a different behavior from the other two systems.

3.2.8. Nematic phase transition for unpolar self-propelled rods

For two-dimensional rods in a system without hydrodynamics it has been shown that the isotropic-nematic phase transition happens at lower densities if the rods are actively driven, see section 1.3.5. In three dimensions, collisions are far less common and do not necessarily result in parallel alignment of the colliding rods. The effect is therefore weaker and more difficult to predict. Despite of this, Figs. 3.11 and 3.19 show that the systems with the neutrally driven rods are no longer in the isotropic state but are nematic. This result may be biased, because the initial state was perfectly nematic, with the nematic axis being parallel to the hard walls. Near the nematic transition correlations decay much slower than in isotropic systems, therefore boundary conditions are rather important in this case [65]. In order to gain less biased results, we performed additional simulations in three dimensions with the following parameters:

- no walls; periodic-boundary conditions in all directions

- box size $60a \times 60a \times 60a$
- rod length $\hat{L} = 10$, diameter $r_\mathrm{b} = 0.8$
- rods neutrally driven
- initial conditions: half of the rods pointing in x-direction, half of them pointing in y-direction[5]; this results in an initial nematic order of $C_\mathrm{nem}(0) = 0.25$
- driving force F_D and number of rods N_s are varied over 18 parameter sets shown in Tab. 3.2

As before, hydrodynamic interactions are included. While these are expected to be weaker for the neutrally driven rods compared to the pushers or pullers, they might still destabilize nematic ordering.

According to the Onsager model for long, thin rods, the isotropic-nematic phase transition of passive rods happens in three dimensions at $\phi_\mathrm{crit}^\mathrm{Ons} = 4\frac{r_\mathrm{b}}{L}$ [96], where r_b is the rod diameter. The critical volume fraction for the rods used here is $\phi_\mathrm{crit}^\mathrm{Ons} = 0.32$, which is much larger than the volume fraction in any of the systems described in Tab. 3.2.

The results are shown in Fig. 3.23. All $N_\mathrm{s} = 3844$ systems and the $F_\mathrm{D} = 200$ and $F_\mathrm{D} = 250$ systems with $N_\mathrm{s} = 3364$ rods take a very long time to reach a steady state, the nematic order is still increasing with time at $t \approx 150 t_\mathrm{L}$[6]. The nematic order parameters for these systems plotted in the bottom right graph of Fig. 3.23 are thus only lower limits. Still it is clear that the nematic order increases significantly with swimming velocity. Future studies, eventually on GPU architecture or without hydrodynamic interactions, will give more insight about the scaling of the nematic order with swimming velocity.

[5] This initial condition is simpler to prepare than the real isotropic state of randomly distributed and oriented rods, because problems with overlapping rods can easily be avoided.

[6] The computational runtime for the $N_\mathrm{s} = 3844$ systems that have not yet reached a steady state is about 1100 hours of CPU time.

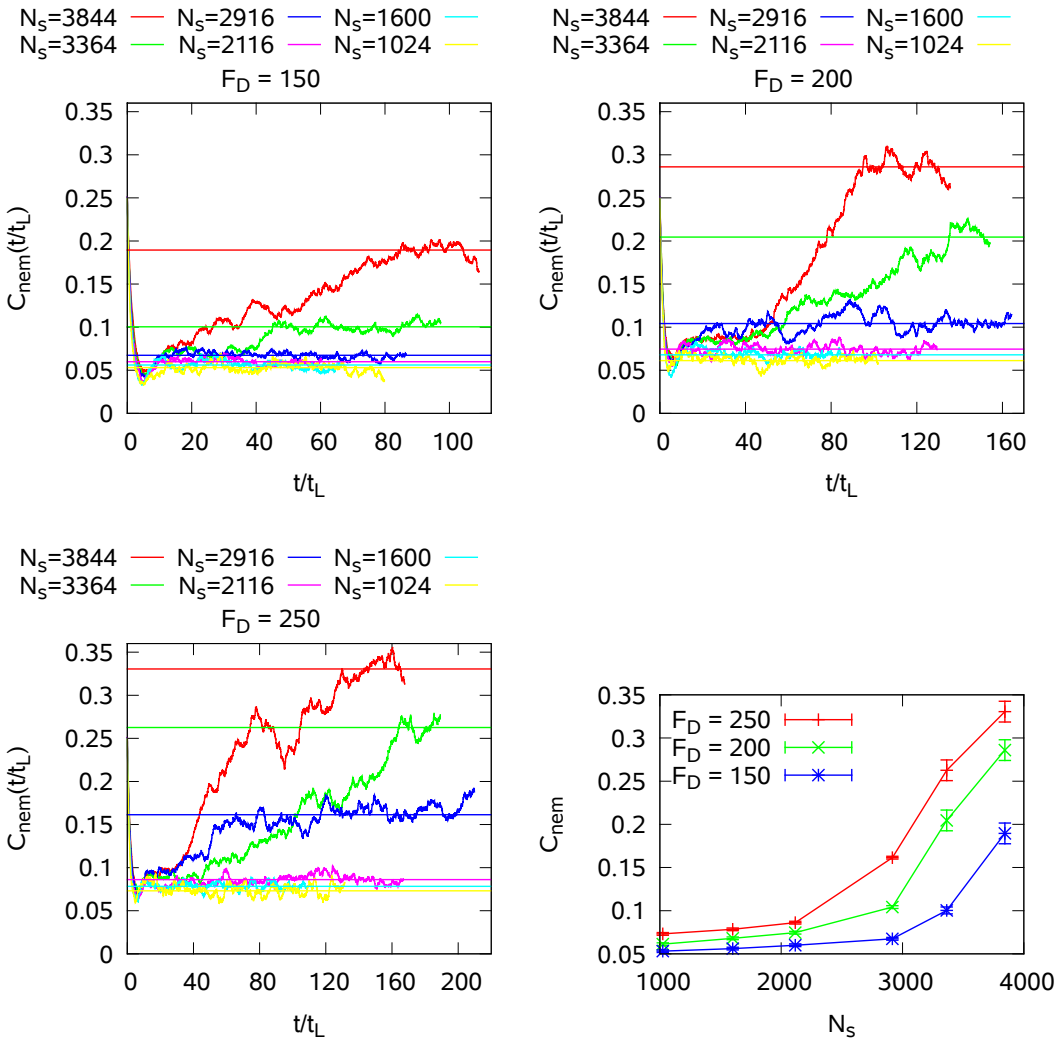

Figure 3.23.: The global nematic order parameter C_{nem}. The top and bottom left plots show the development of $C_{\mathrm{nem}}(t)$ with time (scaled by t_{L}, the time it takes a single swimmer to swim the distance of its own length L, shown in Tab. 3.2), to give an indication whether the systems already reached a steady state. The approximations for $C_{\mathrm{nem}}(t \to \infty)$ are also marked in the plots and are compared for all systems in the bottom right plot. Note however, that the systems with $N_{\mathrm{s}} = 3844$ and two of the $N_{\mathrm{s}} = 3364$ systems have not yet reached a steady state. The C_{nem} values for these systems therefore are only lower limits.

3.3. Multi-sperm systems

3.3.1. Swarming and cluster formation

The sperm model described in section 2.5 can be classified as a pusher swimmer. The matters of interest here are whether the cooperation, swarming and wall-aggregation behavior observed for pusher rods persists in a model system containing short-ranged disturbances due to the flagellar beat and swimmers that differ in parameters such as the beat amplitude and phase. An intermediate goal was to investigate the formation of a sperm vortex [5] as shown in Fig. 1.7. However, the results of the simulations show that while single straight and bend sperm of the *mid-piece curved, torsionally elastic flagellum* (MCE) and *tail-curved, torsionally stiff flagellum* (TCS) classes of this model show a good surface adhesion [52], a higher density of sperm leads to a much higher effective hydrodynamic noise generated by sperm crossing each others paths.

A large number of multi-sperm simulations has been run for various parameter settings. Mostly, the results show that in the bulk the interaction strength between sperm was too weak to lead to beat synchronization and maintain this synchronization over longer time.

Fig. 3.24 shows a snapshot from a large system containing 100 MCE sperm with moderate bending that have demonstrated a good surface adhesion in dilute systems. As can be seen in the bottom plot of Fig. 3.24 the surface aggregation is quite pronounced for this high density, but still the formation of clusters or swarms is not observed. Sometimes two sperm swim together for on the order of five flagellar beats but then part ways even without interference by other swimmers. We therefore do not expect the high density of sperm to be the single or most important hindrance to swarm formation, but the continuous rotation of the beating plane. A simulation run with the same parameters as system (A) except for half the sperm density (only 50 sperm) showed no significantly different characteristics. Similar to the rod systems, the surface excess was shown to decrease with higher swimmer densities [53].

To synchronize, two sperm must meet with identical orientation in the three-dimensional space at a distance along the swimming axis that compensates for the phase difference in the flagellar beat. The surface aggregation leads to a quasi two-dimensional system, where the probability for a match in the orientation is higher, furthermore the surface adhesion is expected to stabilize the

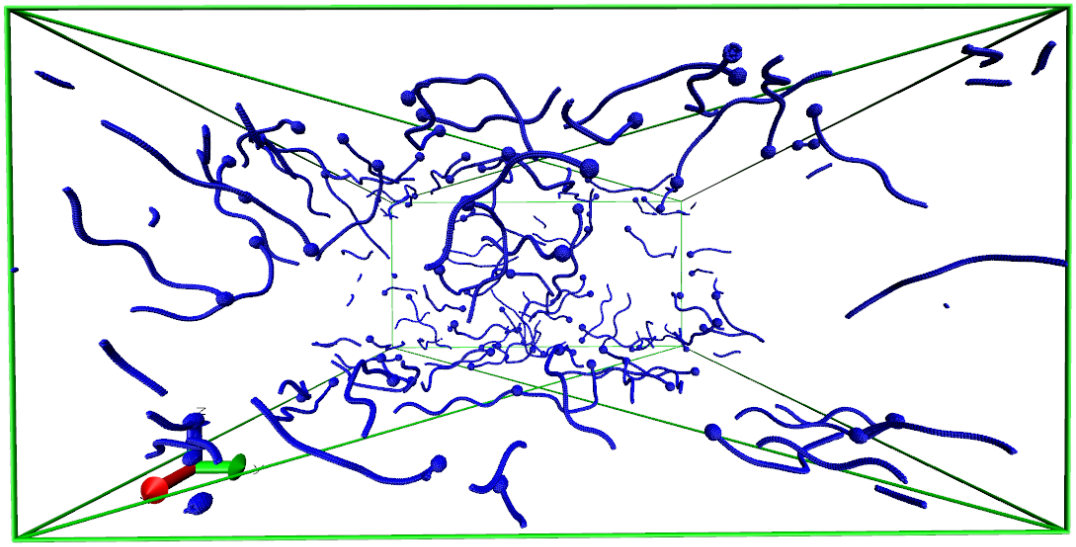

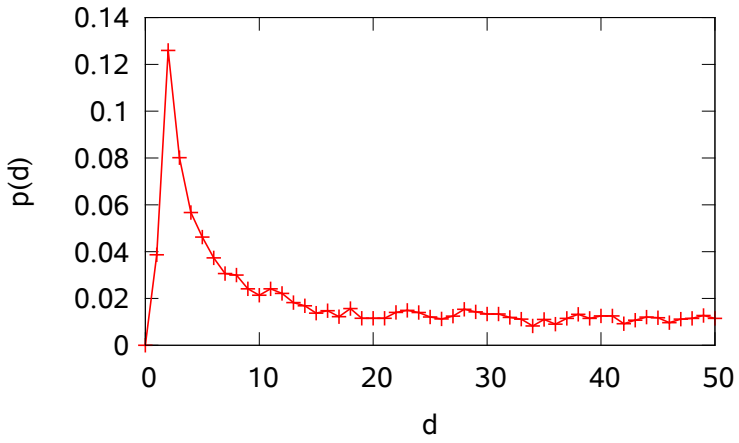

Figure 3.24.: System (A): A system with 100 bend MCE sperm (with a tail length of $L = 50a$, wave number $k = 0.15$, beating frequency $\omega = 0.1$ and random phase shift φ_0) in a simulation box of size $200a \times 200a \times 100a$. No-slip walls are located at the top and the bottom, periodic boundary conditions in the other directions. Top: Snapshot of the system after $t \approx 414 t_B$, where $t_B = \frac{2\pi}{\omega}$ is the duration of one complete beat. Bottom: Sperm density distribution p along the distance to the nearest wall d, averaged over time.

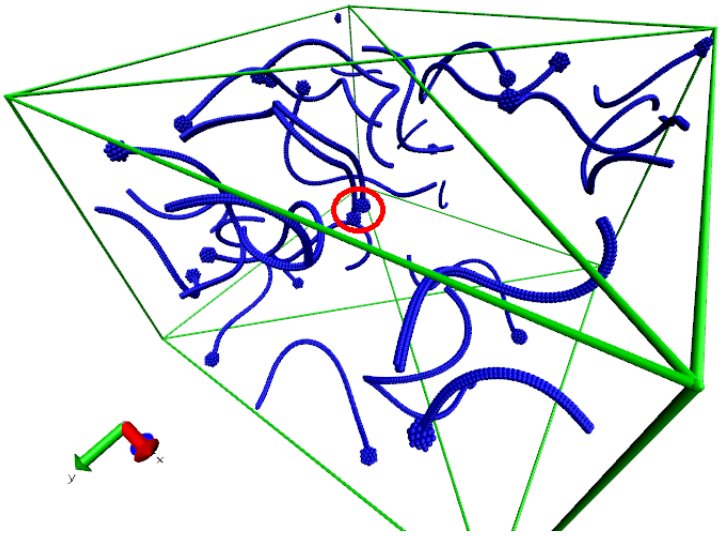

Figure 3.25.: System (B): 20 bend TCS sperm with elongated tails of length $L = 75a$, wave number $k = \pi/50$, beating frequency $\omega = \pi/120$ and a random phase shift φ_0. The snapshot shows the sperm in the simulation box of size $100a \times 100a \times 70a$ after $t \approx 92t_{\mathrm{B}}$. The red circle points out the heads of two synchronized sperm.

cluster. But it increases the collision probability, and the swift motion of sperm flagella crossing the path of a swarm easily destroys the fragile cohesion and surface adhesion. While bend sperm also show a high averaged concentration near the walls, the distance between the single captured swimmers and the wall often oscillates strongly due to the rotation of the beating plane, such that the situation cannot be considered a quasi two-dimensional system. It has also been shown that twisting of the flagellum and its beating plane from front to rear of the flagellum might lead to desynchronization and increases with a higher sperm concentration [53]. Another factor of our sperm model that probably reduces the ability of sperm to synchronize with other swimmers is that the beat frequency ω is constant. A sperm cannot change its phase shift φ_0 to easily adapt to other near sperm, while in nature this should be possible due to varying stress on the flagellum.

A snapshot from simulation (B) of bend TCS sperm with elongated tails ($L = 75a$), lower wave number ($k = \pi/50$) and lower beat frequency ($\omega = \pi/120$) is presented in Fig. 3.25. Over the much longer runtime (which was only possible because of the smaller system size) two clusters of two synchronized sperm swim-

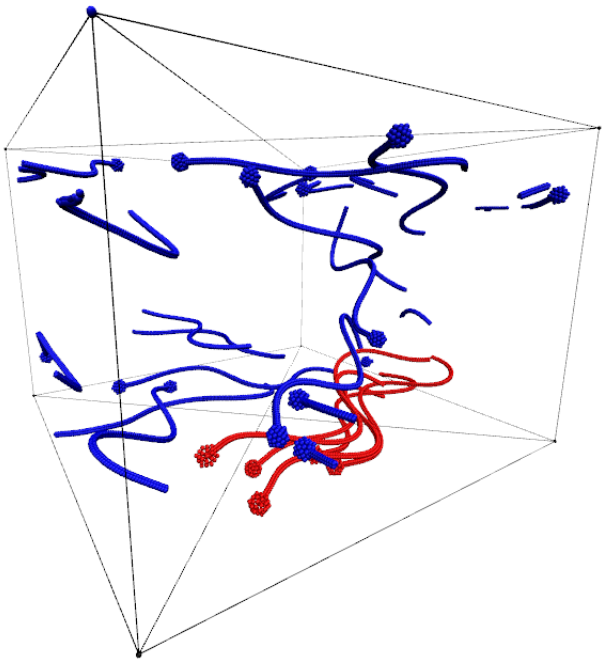

Figure 3.26.: System (C): 20 straight sperm with elongated tails of length $L = 75a$, wave number $k = \pi/50$, beating frequency $\omega = \pi/120$ and no phase shift. A cluster of five sperm close to a wall is marked in red.

ming together for a significant time could be found, surprisingly not for sperm captured near the surface but for bulk sperm (although the surface aggregation in this system is as pronounced as in system (A)). The 50% longer tails increase the strength of the synchronizing interaction, furthermore in this system there is no phase difference between the flagellar beats of all sperm. This is supported by simulation (C) shown in Fig. 3.26, where straight sperm with elongated tails form a swarm of five sperm captured by the surface adhesion. Clusters of two or sometimes three sperm are common in this system. The elongation of the sperm tails however is only a means to increase interaction strength and does not mimic real sperm, although the limit of the long flagellum without the head resembles nematodes [97]. A more promising route to stronger interaction is to introduce a more realistic beat pattern (as is reported in section 3.3.3) and especially to develop a beat mechanism that can adapt the frequency ω, the phase shift φ_0 and possibly even the amplitude A to the stresses resulting from interaction with other sperm.

3.3.2. Wall aggregation depending on head size and beat frequency

As mentioned in Sec. 1.3.6, the degree of surface aggregation strongly depends on anatomic parameters of the model. We studied the influence of the sperm head radius r_h and the beating frequency ω on the surface adhesion of single sperm. The simulations used straight sperm of length $L = 50a$ with two different head sizes and beating frequencies, as well as a flagellum without a head or mid-piece. Along with the head radius, also the number of point particles forming the head has been reduced: While the $r_\mathrm{h} = 2.0a$ head consists of $N_\mathrm{h} = 163$ point particles, the small $r_\mathrm{h} = 0.4a$ head is formed by only twelve particles.

Concerning the long-range interaction, a smaller head and a lower swimming velocity reduce the polarity of the swimmer and therefore the strength of the dipole flow field, such that a weaker interaction is expected. Fig. 3.27 shows that the surface aggregation indeed strongly depends on the head size. It is much weaker for sperm with smaller heads or the flagellum entirely without head. Running the sperm with reduced beat frequency has a similar effect, but it also decreases the swimming velocity. The strong effect of the head radius indicates that hydrodynamic interactions are very important for the surface adhesion of sperm. While it has been shown that this sperm model also displays surface

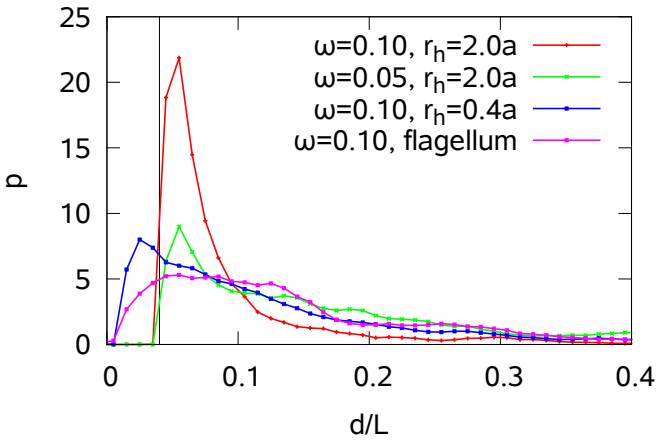

Figure 3.27.: The surface aggregation of straight sperm of length $L = 50a$, two different head radii r_h and beating frequencies ω, as well es for a pure flagellum without a passive head or mid-piece. Each data point is an average over three runs, the statistical error is $\sim 5\%$ for the $r_\mathrm{h} = 2.0$ sperm and about $\sim 15\%$ for the other swimmers. The vertical black line denotes the wall distance $d = 2a$, the nearest distance an $r_\mathrm{h} = 2a$-sperm may approach the wall.

aggregation in the absence of hydrodynamic interactions [72], in their presence the beating plane near a wall is permanently rotated to be perpendicular to the wall and therefore creates an effective repulsion between tail and wall by steric interactions. In the simulations with hydrodynamic interactions the tail rarely touches the wall directly, therefore the steric interactions cannot be important in this case.

3.3.3. Sperm cooperation depending on beat asymmetry

In Sec. 3.3.2 the importance of the sperm model parameters for the wall adhesion has been demonstrated. In light of the results of the multi-sperm simulations (Sec. 3.3.1), we aimed to learn about the influence of the flagellar beat pattern on the degree of synchronization.

Synchronization here means the following: Consider two flagella A and B with a planar beat pattern very close to each other. Let p_A be a point on flagellum A, and p_B the point on flagellum B that is closest to p_A. If the flagella are synchronized, also the phase

$$\varphi(t, s) = ks - \omega t + \varphi_0 \tag{3.7}$$

(compare with Eq. (2.21)) of the beat is the same in the points p_A and p_B, or it is different by π if one of the flagella is rotated by π around the orientation axis. Note first that this does not mean that the sperm heads have to be close to each other if the two sperm have different phase shifts φ_0, and second, in our simulations the beating frequency $\omega = \partial\varphi(t, s)/\partial t$ is constant over time, hence the flagella have to move along their axis of orientation relative to each other in order to synchronize [73]; the synchronization happens in the domain of space, not in the domain of time or frequency.

It has been shown by symmetry considerations that flagellum-driven swimmers would be unable to synchronize if they had a beat pattern with perfect reflection symmetry with respect to the axis perpendicular to their orientation (rear-front symmetry), such as the sine wave [98].

Our simulated sperm still synchronize [53] because the hydrodynamic drag forces deform the semi-flexible flagellum sufficiently, breaking the symmetry of the imposed sinusoidal beat pattern (Eq. (2.21)). For example, for a similar model of the flagellum only, it has been shown [53] that the beating plane is slightly rotated along the flagellum from front to end by $\approx 16°$. In the presence of outer perturbations this distortion is even stronger; in the case of two

synchronized flagella the twist angle is $\approx 18°$, the increase resulting also from direct collision between the flagella. Real sperm beat patterns also do not possess rear-front symmetry, often they display an increasing amplitude towards the rear [99, 6].

In order to increase the synchronizing interaction strength between sperm in our simulations and to make the model more realistic, we modified the imposed beat pattern to include a beating amplitude that increases along the tail from front to rear. First attempts failed due to the strong influence of the hydrodynamics on the actual shape of the beat pattern. A particular problem was the lashing out of the rear end of the tail. We switched to a phenomenological approach and modified $l_\mathrm{b}^{(1)}$ until a *healthy* beat pattern with increasing amplitude was achieved. (Beat patterns strongly vary between species, even a single sperm changes its beat pattern depending on environmental factors like viscosity or presence of boundaries [100], hence no attempt was made to mimic the beat pattern of a particular species.) After a trial-and-error process we arrived at the following bond-length modulation for the simulations presented here:

$$l_\mathrm{b}^{(1)}(t,s) = \begin{cases} l_\mathrm{b} + \frac{1}{6} l_\mathrm{b} A\big(2\cos\varphi(t,s) + 1.7(ks)^{0.9}\sin\varphi(t,s)\big) & \text{for} \quad s < s_\mathrm{T} \\ l_\mathrm{b} + \frac{1}{6} l_\mathrm{b} A\big(2\cos\varphi(t,s) + 1.7(ks)^{0.9}\sin\varphi(t,s) - \frac{1}{70}(ks)^{2.4}\big) & \\ \qquad \cdot\big(\log(14-ks) - 1\big) & \text{else.} \end{cases} \tag{3.8}$$

Here, $s_\mathrm{T} = 60.5149$ is the point of transition[7]. The parameter s is defined such that it is $s = 0$ at the front end of the beating tail, right after the stiff mid-piece; the unit of length of s is $l_\mathrm{b} = 0.5a$. Fig. 3.28 shows plots of the original and the modified $l_\mathrm{b}^{(1)}(t,s)$. Using the new modulation, the bending amplitude first increases, but decreases later due to the logarithmic term. In the plot this can be seen right at the end at $s = 100$; it reduces the lashing out of the rear tip of the tail. The length of the mid-piece has been reduced to $1a$, such that the tail ends at $s = 98$. Effectively, the shortening of the mid-piece has only a small effect, because the beating amplitude at the front of the tail is small. Fig. 3.29 illustrates the modified beat pattern with snapshots of a single sperm taken during one period of the beat and an overlay of ten pictures taken within one

[7] To be precise, at this point the two functions are only equal for $\omega t = n\pi$, $n = 0, 1, 2, \ldots$. The inconsistency is too small to be relevant for the simulations, but in future runs it might be corrected.

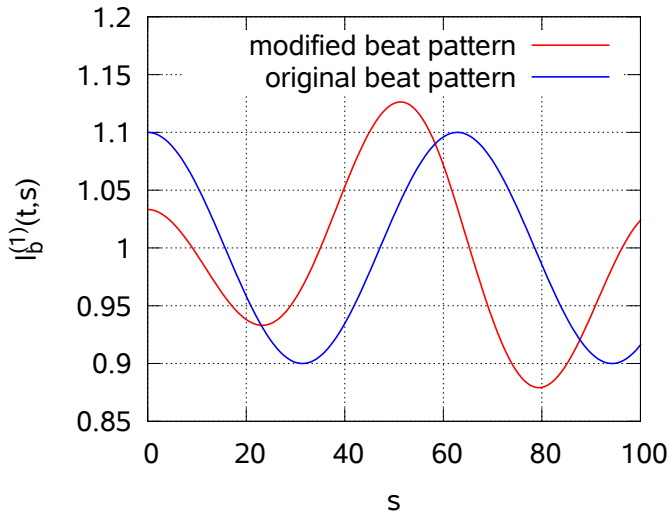

Figure 3.28.: The original (blue) and the modified (red) $l_{\mathrm{b}}^{(1)}(t,s)$ at $t=0$. Note that this is not the form of the (undisturbed) flagellum, but the bending of it.

period demonstrating the envelope of the beat. Snapshots of two synchronized sperm each for both beat patterns are shown in Fig. 3.30.

We run 16 simulations of two sperm with tail length $L = 50a$ and without phase shift starting close to each other (but not touching, at a distance of $8a$) and parallel aligned for both models. Usually the sperm synchronize immediately, swim together for some time Δt_{sync} and then part ways, sometimes due to distortions induced by collision of the flagella. A more detailed description of the synchronization process is given in Ref. [53]. For determining the point of separation, we use a closeness parameter $\zeta_{\mathrm{s}}(t)$. It describes the fraction of sperm-1 beads that are within a threshold distance of at least one of the sperm-2 beads at a given time t. We count the sperm as separated if $\zeta_{\mathrm{s}}(t)$ drops beneath a critical value $\zeta_{\mathrm{s}}^{\mathrm{crit}}$ and afterwards stays below $\zeta_{\mathrm{s}}^{\mathrm{crit}}$ for a given time interval.

Fig. 3.31 shows the percentage of the 16 independent systems $p^{\mathrm{sep}}(t)$ (for both sperm models) in which the sperm pair has already lost its synchronization after time t. On average the original system separates earlier. The average time the pairs succeed to swim together is $\langle \Delta t_{\mathrm{sync}}^{\mathrm{ori}} \rangle = 48(2) t_{\mathrm{B}}$ for the original beat pattern and $\langle \Delta t_{\mathrm{sync}}^{\mathrm{mod}} \rangle = 102(6) t_{\mathrm{B}}$ for the modified beat pattern, which is more than twice as long. At the same time the sample variance is much larger for the modified version. If the goal is to form more stable swarms of sperm, it might be necessary

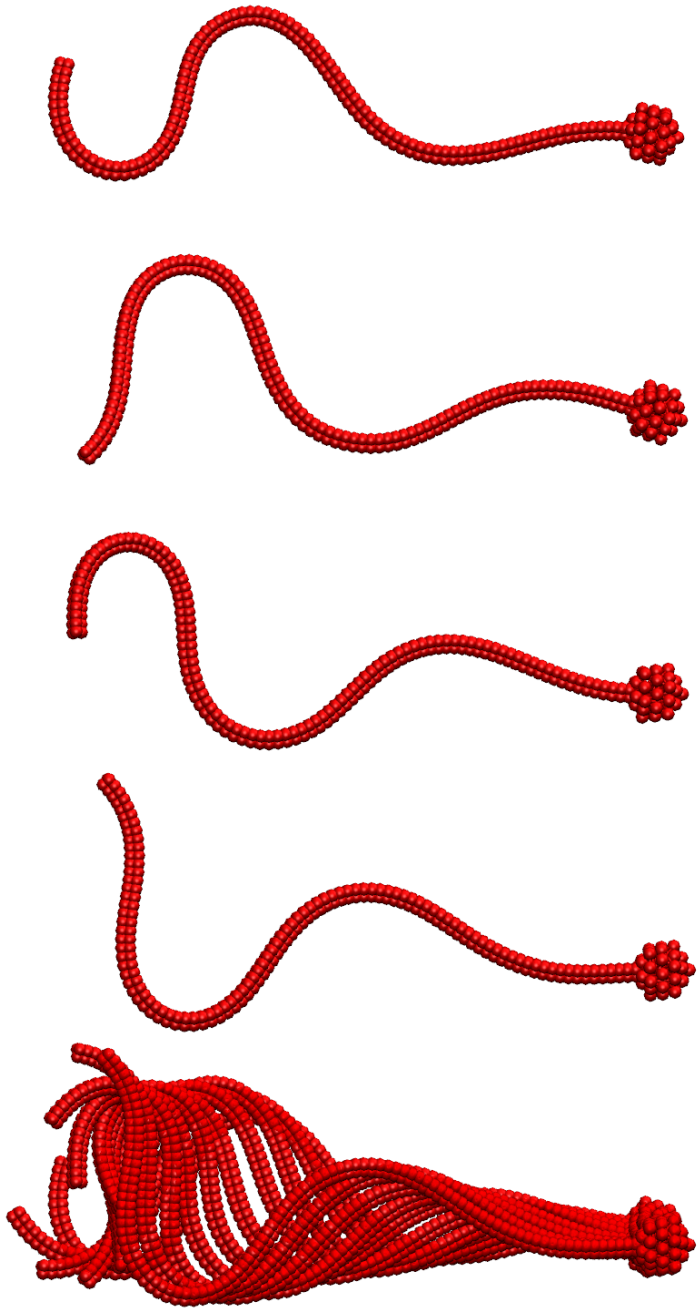

Figure 3.29.: Sequence of snapshots of a single sperm with the modified beat pattern. Top four pictures: the sperm at $t = 0$, $t = 0.24t_{\mathrm{B}}$, $t = 0.48t_{\mathrm{B}}$, $t = 0.72t_{\mathrm{B}}$. Bottom picture: Overlay of ten snapshots taken at $t = n \cdot 0.08t_{\mathrm{B}}$, $n = 0, \ldots, 9$. The uppermost sperm in the overlay is the $n = 9$ case.

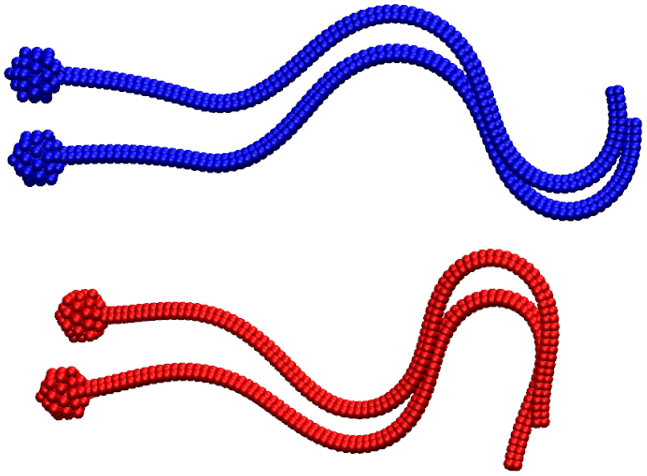

Figure 3.30.: Two synchronized sperm with the two different beat patterns. Blue (top): old beat pattern, defined by Eq. (2.21); red (bottom): new beat pattern with increasing beat amplitude towards the end of the sperm and shortened mid-piece, defined by Eq. (3.8).

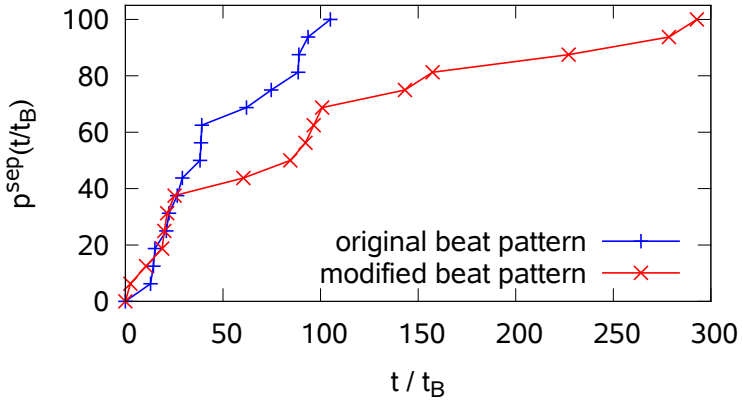

Figure 3.31.: Percentage of sperm that have already separated $p^{\mathrm{sep}}(t)$ after time t. 16 runs were performed for each beat pattern. The mean for the separation time is $\langle \Delta t^{\mathrm{ori}}_{\mathrm{sync}} \rangle = 48(2) t_{\mathrm{B}}$ for the original beat pattern and $\langle \Delta t^{\mathrm{mod}}_{\mathrm{sync}} \rangle = 102(6) t_{\mathrm{B}}$ for the modified beat pattern.

to further tweak the beat pattern in order to lower the variance. Furthermore, in Fig. 3.31 it seems that the modified sperm manage to stay synchronized for a time $t > 25t_{\mathrm{B}}$ continue to do so in a more stable manner. This could mean that for the modified sperm there exists a certain stable configuration that is not always reached; it might also be just a statistical effect due to the low number of runs, and should be studied further.

4. Summary and Outlook

We have developed a general three-dimensional model for self-propelled rod-like swimmers with a large aspect ration L/d. The swimmer experiences a driving force either on its entire body or on the front or rear half, giving it neutral, puller or pusher polarity, respectively. We have studied the behavior of this swimmer rod in particle-based mesoscale hydrodynamics simulations (multi-particle collision dynamics), especially considering systems with no-slip walls.

We have simulated single- and multi-rod systems between two no-slip walls, generally including hydrodynamics and excluded-volume interaction. Even without hydrodynamic interactions, self-propelled rods show a strong surface adhesion in the dilute case by a mechanism of sterical alignment with the walls [36].

Pusher In the pusher case (with hydrodynamics), hydrodynamic interactions support the parallel alignment of single swimmers with the wall and attract the swimmer towards it. The result is a concentration peak closer to the wall compared to neutrally driven swimmers. For higher concentrations of swimmers, the wall aggregation decreases with the number of swimmers N_s present in the system. We attribute this to swirls and jets that have been predicted and observed in active fluids and can be observed in visualizations of our pusher dynamics. A cluster analysis revealed that pushers form medium-size motile clusters (or swarms). Their cluster-size distribution decays with a power law with a small tail towards larger clusters. The average cluster size depends mainly on the rod density and increases weakly with the driving force. Nematic and polar correlation are relatively high for pushers on a short range, in particular very close to the walls. Because of this, pusher clusters have to be polar (and therefore motile). Due to the surface adhesion and the stabilizing steric-alignment effect of the wall, the clusters swim primarily (but not exclusively) near the surfaces. The autocorrelation of the pusher orientation decays exponentially at intermediate and long time scales, but with two different persistence times τ_1 (short times) and τ_2 (long times). τ_1 describes the dynamics of single rods, while the time scale

of the reorientation of whole clusters is given by the larger τ_2. The persistence length of the rods does not depend on the driving force and is proportional to $\frac{1}{\phi}$.

Neutral The neutrally-propelled system also shows wall aggregation based on steric effects, but not as strong as the pusher. Neutral rods show very weak cluster formation, the cluster-size distribution decays faster than a power law. The clusters found are always motile and result from aggregation by steric interaction and are not supported by hydrodynamic interaction. No swirls, jets or other flow defects are observed. Instead, a global nematic order is found that strongly depends on rod density and driving force. In simulations without walls we confirmed these observations. The isotropic-nematic phase transition is shifted to lower densities for self-propelled rods compared to passive rods.

Puller The dilute puller rods also show strong surface adhesion, although by a different mechanism. Hydrodynamic repulsion from the wall and a torque towards perpendicular alignment let the pullers swim along the wall at an oblique angle pointed towards the wall, thus keeping them close to the surface. In multi-rod systems, the cluster-size distribution of pullers follows a power law for clusters up to sizes on the order of 30 in the case of high densities, but also displays a long tail at large cluster sizes. In contrast to the pusher system, pullers form jamming clusters. Close to walls these structures show a hedgehog structure with the pullers pointing towards the surface head first at a large angle. At low densities, usually several smaller clusters are formed. At high densities a significant fraction of the rods (on the order of 40%, depending on system parameters) forms one giant cluster that spans from wall to wall. We also found signs for a typical size around which the single large cluster fluctuates. The typical size of the giant cluster scales with the total number of rods in the system N_s, and therefore with system size. While the puller clusters are not motile, they are also not static. They deform over time and sometimes break apart into faster moving clusters which later collide to reassemble into one giant cluster. These processes however are much slower than the jets and swirls in the pusher system. The formation of jamming clusters in puller systems is the result of the front sides of the rods attracting each other (leading to transient aster-like flow defects), coupled with excluded-volume interaction among the swimmers, which blocks their escape route after the collision.

In order to run the multi-rod simulations in reasonable time and for sufficiently large system sizes, we implemented the excluded-volume interaction on a GPU architecture and adapted an existing GPU implementation of the MPC-SRD algorithm. For our largest systems this resulted in a speedup factor of five, when comparing a single GPU/CPU pair with a node of eight CPUs. For future work with the rod model we suggest to continue the development and optimization of the GPU version as it is more cost efficient than large scale CPU parallelization.

Using this GPU implementation, the studies concerning the isotropic-nematic phase transition of neutral swimmers should be continued and extended with systems at higher densities and driving forces, and they should be compared to similar systems without hydrodynamic interactions. Concerning the pusher systems, a detailed study of the flow defects, by analyzing the fluid flow directly instead of the swimmers, seems to be promising. For applications of microfluidic chips, studies about cluster formation in shear flow would be of interest. Here the question is whether large jamming clusters might clog the microchannels.

Sperm We also continued studies with a more specific model for sperm motility in order to understand the role of a beating flagellum in swimmer dynamics. We observed the formation of sperm swarms in multi-sperm systems of symmetric, straight swimming sperm, but the attractive interaction between bend sperm was not sufficient for clustering. To reproduce the swarming behavior of real sperm, we decided to optimize our sperm model and started to study the influence of anatomic parameters on the sperm behavior. We found that decreasing the size of the sperm head or removing it entirely reduces the surface adhesion of single sperm. A similar effect results from decreasing the beat frequency. Considering the form of the flagellum beat we introduced a new model that results in a more asymmetric beat pattern. Here, the amplitude of the traveling wave increases from front to rear. This extends the mean time two synchronized swimming sperm stay together, but it also increases the variance. For future studies the model for the increasing-amplitude beat pattern should be optimized. Further steps should include a feedback mechanism that permits the flagellum to adapt parameters like the beat frequency, phase shift and amplitude to the hydrodynamic stresses. Finally, it would be interesting to implement viscoelastic fluids, as the natural environment of sperm is non-Newtonian due to high protein concentrations. This has been shown to influence swimming velocity and flagellar beat pattern [101, 28], and implementation of viscoelastic

fluids in the MPC dynamics has been successfully demonstrated [102, 103].

Appendix A.

GPU implementation of the excluded-volume interactions

In the single-rod simulations presented in Sec. 3.1 the part of the simulation taking most of the CPU time is by far the hydrodynamics (MPCD) part. The computational cost of the MD simulations dealing with the movement of the swimmer beads is negligible. To a lesser degree, this is still true for the multi-rod systems if only the bonded interactions are considered. As soon as non-bonded excluded-volume interactions between the swimmers are important, the computational cost increases dramatically with the number of swimmers N_s, and the MD part of the simulation clearly dominates the CPU time compared to the MPCD part.

The problem is as follows: Every two beads that do not belong to the same swimmer and come closer than the cutoff distance r_b feel a mutually repellent force (described by the potential in Eq. (2.6)). The simplest solution is to calculate the distances between all beads in question; these are $C_0 = N_\mathrm{s}(N_\mathrm{s} - 1)\hat{L}^2$ calculations. Considering in the high-density system of Sec. 3.2 there are $N_\mathrm{s} = 6048$ rods of length $\hat{L} = 20$, we have nearly $C_0 = 1.5 \cdot 10^{10}$ distance calculations per MD step or almost $3 \cdot 10^{13}$ distance calculations per time unit, which is a bit much for today's computers.

Neighbor lists For the simulations in this work we used the neighbor-list scheme. The commonly known principle is to create lists of particles in such a way that particles in list A can only interact with particles in a small number of other lists. In the case of the MPCD/MD simulations the size of the MPC cells a is larger than the cutoff distance and larger than the distance a swimmer bead is expected to travel in one MPC step, *but not much larger*. Taking into

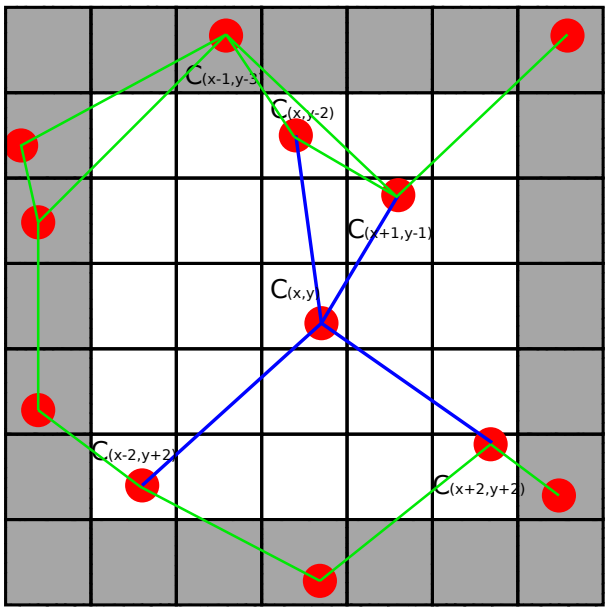

Figure A.1.: Two-dimensional version of the neighbor lists: Beads in the center cell $C_{(x,y)}$ might only interact (blue lines) with beads in cells two steps away $C_{x\pm\{0,1,2\},y\pm\{0,1,2\}}$, and not with beads in cells beyond (colored in gray). This is true for every bead, so if this step is repeated for each of the beads shown, the green links for possible interaction (and further links to particles outside the drawn area) are added. The linear size of one cell is a, the cutoff range for the interaction is $r_\mathrm{b} = 0.8$.

account that during the MPC step the particles are already sorted into lists C_j containing all particles within MPC cell j, this seems to be the optimal starting point for neighbor lists. For the excluded-volume interactions, we assume that during one MPC step a swimmer bead $i \in C_j$ in cell j can only interact with other beads that are located in cells two cells away (counting diagonal movement as one step) at the end of the MPC step (see Fig. A.1). In a three-dimensional system, each cell has $5 \times 5 \times 5 = 125$ neighbor cells (including itself). After a few MD steps (of which there are about 20 between MPC steps) the beads might have changed their cell, but the old lists are kept. We assume that the time is not sufficient for beads from outside this limit to come into interaction range $r_\mathrm{b} = 0.8a$ with beads in the center cell.

Another advantage of the neighbor lists is that is makes large-scale parallelization possible. Assuming the particles are distributed among several CPUs

according to the particles positions in space, only a limited amount of information would have to be transported between CPUs. A detailed description of a similar scheme of information transport for the parallelization of the MPC algorithm is given in Ref. [104]. The parallelization employed in our studies only involves work distribution in true shared-memory systems, making the problem of information transport less severe. All our simulations except for the large multi-rod runs described in table 3.1 have been run on single nodes (consisting of 8 CPUs) of the Juropa supercomputer at the Jülich Supercomputing Centre (JSC), using the OpenMP parallelization interface. For very large systems, especially those that show clustering behavior (like the puller systems in table 3.1) and therefore increase the frequency of excluded-volume interactions, this level of parallelization is not sufficient.

CUDA port The chosen solution was to port the MD part to the CUDA API so it can be run on the Judge NVidia GPU (*graphics processing unit*) cluster in the JSC. The GPU architecture provides a high number of processors combined with efficient thread management and fast shared memory [105]. The structure is fundamentally different from the x86 CPU architecture, making custom optimizations of the algorithms in use necessary. For example the bottleneck in performance usually is random memory-access latency, which hence should be avoided if possible. The MPC part of the simulation was already ported to CUDA [106] (with some limitations by that time). This implementation was adapted and extended to include no-slip walls for use in our simulations. Due to lack of time several advanced optimizations employed by Westphal have not been used, leaving room for further improvement of the performance. It follows a short summary of the implementation of the MD part of the simulation on the CUDA framework. We describe the logical order of subroutine execution, however the MD and MPC parts are largely independent of each other and therefore partly run simultaneously using CUDA streams.

1. **Grid shift.**

2. **Fluid streaming step.** For each fluid particle i: Start a thread that calculates the new position $\vec{r}_i(t + \Delta t)$ after the streaming step and the new MPC cell number j. Append particle i to the linked list of particles

in cell C_j using atomic instructions[1].

3. **Integrate bead motion.** This consists of several sub-steps that are repeated $\Delta t_{\mathrm{mpc}}/\Delta t_{\mathrm{md}} = 20$ times. It is assumed the the EV interaction lists (step 5) have already been built in the previous iteration.

   a) **Velocity Verlet I.** For each bead start a thread: The first half of the velocity Verlet integration scheme is performed with the old acceleration data.

   b) **Calculate bonded interactions.** For each bead start a thread: Calculate bonded interactions.

   c) **Calculate EV interactions.** For each bead i start a thread: Calculate the distance d to all beads in the EV interaction list and add the acceleration for bead i if $d \leq r_{\mathrm{b}}$.

   d) **Velocity Verlet II.** For each bead start a thread: The second half of the velocity Verlet integration scheme is performed with the new acceleration data.

4. **Build EV cell lists.** In order to keep the MD and MPC parts as detached from each other as possible (to allow for parallel processing) the excluded-volume interaction uses a different set of lists. Two layers of lists are employed, the first one being the cell lists also in use in the CPU version, described in Fig. A.1 (but separate from the fluid particle lists). Here, for each swimmer bead one thread is started to sort the particle into bead-cell lists.

5. **Build EV interaction lists.** For each bead i start a thread: Determine the 125 neighbor lists of the cell of particle i and generate a list with all potential interaction partners in these 125 cells. For this list a special structure described below is used.

6. **Calculate center-of-mass velocities of cells.** For each cell start a thread: Sum up momentum of all particles (beads and fluid) in this cell,

[1] Linked lists are particularly poor suited for use on the GPU, however sometimes they cannot be avoided easily. Atomic operations like *look up a value x in memory, overwrite it with y and return the old x* are guaranteed to be executed without interruption by other threads, making linked-list handling thread save without the need for thread locks (which would seriously hurt performance).

add momentum transfer from the driving force F_{D} of the active beads if present.

7. **Collision step for fluid particles.** For this, start one thread per fluid particle.

8. **Collision step for bead particles.** For this, start one thread per bead particle. (Separate from fluid collision because of the different list structures.)

The EV interaction list is a list for each bead i containing all beads in the 125 neighbor lists. This list is read 20 times by step 3c, we therefore wanted to avoid using a linked list. We employed a fixed size array instead under the assumption that each bead has at most $N_{\mathrm{i}} = 128$ possible interaction partners. Test runs have confirmed this number to be sufficient. The memory structure of the EV interaction list is as follows, where BxPy denotes the y-th possible interaction partner of bead x: B0P0, B1P0, B2P0, ..., B0P1, B1P1, B2P1, ..., B0P127, B1P127, B2P127, ... When in step 3c an array of threads reads from this list, the memory access is *coalesced*, meaning threads 0, 1, 2... read the data in consecutive order, avoiding random memory access (see Ref. [105] on coalesced memory access).

For comparison, we ran the bl1-system from Tab. 3.1 on a CPU and GPU architecture. The bl1 system contains $N_{\mathrm{s}} = 6048$ puller rods, consisting of $\hat{L}N_{\mathrm{s}} = 120960$ beads, in a box of size $120a \times 120a \times 60a$, containing $8.6 \cdot 10^6$ fluid particles. The CPU machine is one node of the Juropa supercomputer with eight Intel Xeon 2.93GHz cores, the GPU machine is a node on the Judge cluster (*Juelich Dedicated GPU Environment*), consisting of twelve Intel Xeon 2.66GHz cores and two NVidia Tesla M2050 (Fermi) GPU cards. Our program uses only one GPU core and one CPU core, so that we could run to simulations at once on each Judge node. After a runtime of 23h and 20min, the simulation on the Juropa node advanced by 950 time units (corresponding to 47500 MPC steps). At the same time the simulation on half a Judge node advanced by 4937 time units (246850 MPC steps, which is 5.2 times as fast as the CPU version) if double floating point precision was used (as was on Juropa), and by 5596 time units (279800 MPC steps) if single floating point precision was used. We could not detect significant differences between systems run on single precision compared to double precision, however further testing is necessary here. Furthermore at

this early stage of the simulations, the systems were still in the homogeneous phase (especially the CPU system). It is to be expected that the CPU version of the program will show a stronger slow-down at stages of high-density clustering, due to the increased number of excluded-volume interactions.

Appendix B.

Abbreviations and Symbols

Symbols with a hat (e.g. $\hat{L}$) are dimensionless numbers that count discrete elements.

- A flagellum-beat strength (bending amplitude)
- a linear size of one MPC-cell; basic unit of length
- α angle of rotation for the relative velocities in the SRD collision step
- β exponent of the power law describing the decay of the cluster-size distribution
- c cluster size
- c_{s} velocity of sound in the MPC fluid
- ζ parameter describing the degree of spatial closeness between all parts of two sperm flagella
- d distance
- d_{LJ} range of the repulsive Lennard-Jones potential of the walls
- Δt_{md} time step of the MD part of the simulation
- Δt_{mpc} time step of the MPC part of the simulation
- η dynamic viscosity of the fluid
- F_{D} total driving force of a rod
- F_{wall} attractive force between swimmer and wall

- k wave number of sperm beat
- k_B Boltzmann constant
- K_b spring constant for the bonds between neighboring beads in the swimmer
- K_bend bending-stiffness constant for rods
- $l_\mathrm{b}^{(i)}$ bond length between neighboring beads on filament i of the swimmer
- $\hat{L}$ number of beads in a rod
- L length of a rod or length of the tail of the sperm; $L = \hat{L} \cdot l_b$
- m_b mass of a bead (solute particle) in a rod
- m_fl mass of a fluid particle; basic unit of mass
- N_s number of swimmers in the system
- $n(c)$ number of clusters of size c
- $\vec{n}_i$ orientation of swimmer i
- ω sperm beat frequency
- p pressure
- $p(z)$ probability density of swimmers at distance z from the nearest wall
- $p^{>}(c)$ average percentage of rods that are part of a cluster of size c or bigger
- φ_0 constant phase shift of the sperm
- r_b diameter of a bead concerning excluded-volume interaction
- r_h sperm-head radius
- $\vec{r}_i$ position of particle i
- $\hat{\rho}$ number of fluid particles per MPC cell of volume a^3; fluid (mass) density: $\rho = \hat{\rho} \cdot m_\mathrm{fl}/a^3$

- s position along the flagellum of a sperm
- T temperature of the fluid
- t time
- $t_{\mathrm{B}} = \frac{2\pi}{\omega}$ duration of one beat of the sperm
- $t_{\mathrm{L}} = L/v_0$ the time it takes a single swimmer to swim the distance of its own length L
- τ persistence time
- θ angle between swimmer and wall
- $\vec{u}(\vec{r})$ velocity of the fluid element at position $\vec{r}$
- V volume of the system box
- v_0 swimming velocity of a single, undisturbed swimmer
- $\vec{v}_i$ velocity of particle or swimmer i
- $\vec{v}_j^{\mathrm{CM}}$ center-of-mass velocity of all particles in cell j
- ξ_{p} persistence length

Bibliography

[1] T. Vicsek and A. Zafiris, *Collective motion*, arXiv:1010.5017, 2010.

[2] N. H. Mendelson, A. Bourque, K. Wilkening, K. R. Anderson, and J. C. Watkins, *Organized Cell Swimming Motions in Bacillus subtilis Colonies: Patterns of Short-Lived Whirls and Jets*, Journal of Bacteriology **181**, 600 (1999).

[3] M. F. Copeland and D. B. Weibel, *Bacterial swarming: a model system for studying dynamic self-assembly*, Soft Matter **5**, 1174 (2009).

[4] A. P. Berke, L. Turner, H. C. Berg, and E. Lauga, *Hydrodynamic Attraction of Swimming Microorganisms by Surfaces*, Physical Review Letters **101**, 038102 (2008).

[5] I. H. Riedel, K. Kruse, and J. Howard, *A Self-Organized Vortex Array of Hydrodynamically Entrained Sperm Cells*, Science **309**, 300 (2005).

[6] J. Gray, *The Movement of Sea-Urchin Spermatozoa*, Journal of Experimental Biology **32**, 775 (1955).

[7] M. Böhmer, Q. Van, I. Weyand, V. Hagen, M. Beyermann, M. Matsumoto, M. Hoshi, E. Hildebrand and U. B. Kaupp, *Ca2+ spikes in the flagellum control chemotactic behavior of sperm*, EMBO Journal **24**, 2741 (2005).

[8] H. C. Berg and D. A. Brown, *Chemotaxis in Escherichia coli analysed by Three-dimensional Tracking*, Nature **239**, 500 (1972).

[9] E. H. Harris, *Chlamydomonas as a Model Organism*, Annual Review of Plant Physiology and Plant Molecular Biology **52**, 363 (2001).

[10] J. P. Hernandez-Ortiz, C. G. Stoltz, and M. D. Graham, *Transport and Collective Dynamics in Suspensions of Confined Swimming Particles*, Physical Review Letters **95**, 204501 (2005).

[11] V. Narayan, S. Ramaswamy, and N. Menon, *Long-Lived Giant Number Fluctuations in a Swarming Granular Nematic*, Science **317**, 105 (2007).

[12] Y. Hatwalne, S. Ramaswamy, M. Rao, and R. A. Simha, *Rheology of Active-Particle Suspensions*, Physical Review Letters **92**, 118101 (2004).

[13] M. J. Kim and K. S. Breuer, *Enhanced diffusion due to motile bacteria*, Physics of fluids **16**, L78 (2004).

[14] P. T. Underhill, J. P. Hernandez-Ortiz, and M. D. Graham, *Diffusion and Spatial Correlations in Suspensions of Swimming Particles*, Physical Review Letters **100**, 248101 (2008).

[15] L. I. Segerink, A. J. Sprenkels, P. M. ter Braak, I. Vermes, and A. van den Berg, *On-chip determination of spermatozoa concentration using electrical impedance measurements*, Lab on a Chip **10**, 1018 (2010).

[16] L. D. Landau and E. M. Lifschitz, *Hydrodynamik* (Akademie Verlag, 1991).

[17] D. B. Dusenbery, *Life at small Scale - The Behavior of Microbes* (Scientific American Library, 1996).

[18] E. M. Purcell, *Life at low Reynolds number*, American Journal of Physics **45**, 3 (1977).

[19] Alexander, G. P. and Yeomans, J. M., *Dumb-bell swimmers*, Europhysics Letters **83**, 34006 (2008).

[20] E. Lauga and D. Bartolo, *No many-scallop theorem: Collective locomotion of reciprocal swimmers*, Physical Review E **78**, 030901 (2008).

[21] G. Taylor, *The Action of Waving Cylindrical Tails in Propelling Microscopic Organisms*, Proceedings of the Royal Society of London. Series A. Mathematical and Physical Sciences **211**, 225 (1952).

[22] B. M. Friedrich, I. H. Riedel-Kruse, J. Howard, and F. Jülicher, *High-precision tracking of sperm swimming fine structure provides strong test of resistive force theory*, Journal of Experimental Biology **213**, 1226 (2010).

[23] G. K. Batchelor, *Slender-body theory for particles of arbitrary cross-section in Stokes flow*, Journal of Fluid Mechanics **44**, 419 (1970).

[24] R. E. Johnson and C. J. Brokaw, *Flagellar hydrodynamics. A comparison between resistive-force theory and slender-body theory.*, Biophysical Journal **25**, 113 (1979).

[25] M. M. Tirado and J. G. de la Torre, *Translational friction coefficients of rigid, symmetric top macromolecules. Application to circular cylinders*, Journal of Chemical Physics **71**, 2581 (1979).

[26] M. M. Tirado, C. L. Martinez, and J. G. de la Torre, *Comparison of theories for the translational and rotational diffusion coefficients of rodlike macromolecules. Application to short DNA fragments*, Journal of Chemical Physics **81**, 2047 (1984).

[27] J. Elgeti and G. Gompper, Hydrodynamics of active mesoscopic systems, in *NIC Symposion*, John von Neumann Institute for Computing, 2008.

[28] E. Gaffney, H. Gadlha, D. Smith, J. Blake, and J. Kirkman-Brown, *Mammalian Sperm Motility: Observation and Theory*, Annual Review of Fluid Mechanics **43**, 501 (2011).

[29] Y. Wang, R. M. Hernandez, D. J. Bartlett, J. M. Bingham, T. R. Kline, A. Sen, T. E. Mallouk, *Bipolar Electrochemical Mechanism for the Propulsion of Catalytic Nanomotors in Hydrogen Peroxide Solutions*, Langmuir **22**, 10451 (2006).

[30] H. C. Berg, *E. coli in Motion* (Springer New York, 2003).

[31] L. Jelsbak and L. Sgaard-Andersen, *Pattern formation: fruiting body morphogenesis in Myxococcus xanthus*, Current Opinion in Microbiology **3**, 637 (2000).

[32] K. Drescher, K. C. Leptos, I. Tuval, T. Ishikawa, T. J. Pedley and R. E. Goldstein, *Dancing Volvox: Hydrodynamic Bound States of Swimming Algae*, Physical Review Letters **102**, 168101 (2009).

[33] W. F. Paxton, K. C. Kistler, C. C. Olmeda, A. Sen, S. K. St. Angelo, Y. Cao, T. E. Mallouk, P. E. Lammert and V. H. Crespi, *Catalytic Nanomotors: Autonomous Movement of Striped Nanorods*, Journal of the American Chemical Society **126**, 13424 (2004).

[34] G. Ozin, I. Manners, S. Fournier-Bidoz, and A. Arsenault, *Dream Nanomachines*, Advanced Materials **17**, 3011 (2005).

[35] V. Schaller, C. Weber, C. Semmrich, E. Frey, and A. R. Bausch, *Human sperm accumulation near surfaces: a simulation study*, Nature **467**, 73 (2010).

[36] J. Elgeti and G. Gompper, *Self-propelled rods near surfaces*, Europhysics Letters **85**, 38002 (2009).

[37] G. Li and J. X. Tang, *Accumulation of Microswimmers near a Surface Mediated by Collision and Rotational Brownian Motion*, Physical Review Letters **103**, 078101 (2009).

[38] J. P. Hernandez-Ortiz, P. T. Underhill, and M. D. Graham, *Dynamics of confined suspensions of swimming particles*, Journal of Physics: Condensed Matter **21**, 204107 (13pp) (2009).

[39] T. Ishikawa, *Suspension biomechanics of swimming microbes*, Journal of The Royal Society Interface **6**, 815 (2009).

[40] E. Lauga and T. R. Powers, *The hydrodynamics of swimming microorganisms*, Reports on Progress in Physics **72**, 096601 (2009).

[41] I. O. Götze and G. Gompper, *Mesoscale simulations of hydrodynamic squirmer interactions*, Physical Review E **82**, 041921 (2010).

[42] J. R. Blake, *A note on the image system for a stokeslet in a no-slip boundary*, Mathematical Proceedings of the Cambridge Philosophical Society **70**, 303 (1971).

[43] J. S. Guasto, K. A. Johnson, and J. P. Gollub, *Oscillatory Flows Induced by Microorganisms Swimming in Two Dimensions*, Physical Review Letters **105**, 168102 (2010).

[44] K. Drescher, R. E. Goldstein, N. Michel, M. Polin, I. Tuval, *Direct Measurement of the Flow Field around Swimming Microorganisms*, Physical Review Letters **105**, 168101 (2010).

[45] G. Gompper, Microswimmers, in *42nd IFF Springschool 2011, Macromolecular Systems in Soft and Living Matter*, Forschungszentrum Jülich, 2011.

[46] T. Vicsek, A. Czirók, E. Ben-Jacob, I. Cohen, and O. Shochet, *Novel Type of Phase Transition in a System of Self-Driven Particles*, Physical Review Letters **75**, 1226 (1995).

[47] V. Mehandia and P. R. Nott, *The collective dynamics of self-propelled particles*, Journal of Fluid Mechanics **595**, 239 (2008).

[48] V. Gyrya, I. Aranson, L. Berlyand, and D. Karpeev, *A Model of Hydrodynamic Interaction Between Swimming Bacteria*, Bulletin of Mathematical Biology **72**, 148 (2010).

[49] A. Najafi and R. Golestanian, *Simple swimmer at low Reynolds number: Three linked spheres*, Physical Review E **69**, 062901 (2004).

[50] M. Leoni, J. Kotar, B. Bassetti, P. Cicuta, and M. C. Lagomarsino, *A basic swimmer at low Reynolds number*, Soft Matter **5**, 472 (2009).

[51] L. Rothschild, *Non-random Distribution of Bull Spermatozoa in a Drop of Sperm Suspension*, Nature **198**, 1221 (1963).

[52] J. Elgeti, U. B. Kaupp, and G. Gompper, *Hydrodynamics of Sperm Cells near Surfaces*, Biophysical Journal **99**, 1018 (2010).

[53] Y. Yang, *Swimming and Swarming of Self-Propelled Particles*, PhD thesis, Cologne University, 2009.

[54] L. J. Fauci and A. McDonald, *Sperm motility in the presence of boundaries*, Bulletin of Mathematical Biology **57**, 679 (1995).

[55] H. H. Wensink and H. Löwen, *Aggregation of self-propelled colloidal rods near confining walls*, Physical Review E **78**, 031409 (2008).

[56] S. Rafaï, L. Jibuti, and P. Peyla, *Effective Viscosity of Microswimmer Suspensions*, Physical Review Letters **104**, 098102 (2010).

[57] J. Henrichsen, *Bacterial surface translocation: a survey and a classification*, Bacteriological Reviews **36**, 478 (1972).

[58] D. A. Fletcher and J. A. Theriot, *An introduction to cell motility for the physical scientist*, Physical Biology **1**, T1 (2004).

[59] Y. Yang, V. Marceau, and G. Gompper, *Swarm behavior of self-propelled rods and swimming flagella*, Physical Review E **82**, 031904 (2010).

[60] F. Ginelli, F. Peruani, M. Bär, and H. Chaté, *Large-Scale Collective Properties of Self-Propelled Rods*, Physical Review Letters **104**, 184502 (2010).

[61] S. R. McCandlish, A. Baskaran, and M. F. Hagan, *Spontaneous Segregation of Self-Propelled Particles with Different Motilities*, arXiv:1110.2479, 2011.

[62] L. Onsager, *The Effects of Shape on the Interaction of colloidal Particles*, Annals of the New York Academy of Sciences **51**, 627 (1949).

[63] J. Kierfeld, K. Frentzel, P. Kraikivski, and R. Lipowsky, *Active dynamics of filaments in motility assays*, The European Physical Journal - Special Topics **157**, 123 (2008).

[64] A. Baskaran and M. C. Marchetti, *Nonequilibrium statistical mechanics of self-propelled hard rods*, Journal of Statistical Mechanics: Theory and Experiment **2010**, P04019 (2010).

[65] A. Baskaran and M. C. Marchetti, *Enhanced Diffusion and Ordering of Self-Propelled Rods*, Physical Review Letters **101**, 268101 (2008).

[66] R. Aditi Simha and S. Ramaswamy, *Hydrodynamic Fluctuations and Instabilities in Ordered Suspensions of Self-Propelled Particles*, Physical Review Letters **89**, 058101 (2002).

[67] A. Baskaran and M. C. Marchetti, *Statistical mechanics and hydrodynamics of bacterial suspensions*, Proceedings of the National Academy of Sciences **106**, 15567 (2009).

[68] D. Saintillan and M. J. Shelley, *Orientational Order and Instabilities in Suspensions of Self-Locomoting Rods*, Physical Review Letters **99**, 058102 (2007).

[69] D. Saintillan and M. J. Shelley, *Instabilities and Pattern Formation in Active Particle Suspensions: Kinetic Theory and Continuum Simulations*, Physical Review Letters **100**, 178103 (2008).

[70] J. Elgeti, M. E. Cates, and D. Marenduzzo, *Defect hydrodynamics in 2D polar active fluids*, Soft Matter **7**, 3177 (2011).

[71] H. Moore, K. Dvorakova, N. Jenkins, and W. Breed, *Exceptional sperm cooperation in the wood mouse*, Nature **418**, 174 (2002).

[72] J. Elgeti, *Sperm and Cilia Dynamics*, PhD thesis, Cologne University, 2006.

[73] Y. Yang, J. Elgeti, and G. Gompper, *Cooperation of sperm in two dimensions: Synchronization, attraction, and aggregation through hydrodynamic interactions*, Physical Review E **78**, 061903 (2008).

[74] J. Elgeti, U. B. Kaupp, and G. Gompper, *Response to Comment on Article: Hydrodynamics of Sperm Cells Near Surfaces*, Biophysical Journal **100**, 2321 (2011).

[75] D. M. Woolley, *Motility of spermatozoa at surfaces*, Reproduction **126**, 259 (2003).

[76] D. J. Smith, E. A. Gaffney, J. R. Blake, and J. C. Kirkman-Brown, *Human sperm accumulation near surfaces: a simulation study*, Journal of Fluid Mechanics **621**, 289 (2009).

[77] D. J. Smith, E. Gaffney, H. Shum, H. Gadlha, and J. Kirkman-Brown, *Comment on the Article by J. Elgeti, U. B. Kaupp, and G. Gompper: Hydrodynamics of Sperm Cells Near Surfaces*, Biophysical Journal **100**, 2318 (2011).

[78] L. Verlet, *Computer "Experiments" on Classical Fluids. I. Thermodynamical Properties of Lennard-Jones Molecules*, Physical Review **159**, 98 (1967).

[79] A. Malevanets and R. Kapral, *Mesoscopic model for solvent dynamics*, The Journal of Chemical Physics **110**, 8605 (1999).

[80] T. Ihle and D. M. Kroll, *Stochastic rotation dynamics. I. Formalism, Galilean invariance, and Green-Kubo relations*, Physical Review E **67**, 066705 (2003).

[81] T. Ihle and D. M. Kroll, *Stochastic rotation dynamics. II. Transport coefficients, numerics, and long-time tails*, Physical Review E **67**, 066706 (2003).

[82] E. Tüzel, M. Strauss, T. Ihle, and D. M. Kroll, *Transport coefficients for stochastic rotation dynamics in three dimensions*, Physical Review E **68**, 036701 (2003).

[83] G. Gompper, T. Ihle, D. M. Kroll, and R. G. Winkler, *Multi-Particle Collision Dynamics: A Particle-Based Mesoscale Simulation Approach to the Hydrodynamics of Complex Fluids*, Advances in Polymer Science **22**, 1 (2009).

[84] R. Kapral, *Multiparticle Collision Dynamics: Simulation of Complex Systems on Mesoscales*, Advances in Chemical Physics **140**, 89 (2008).

[85] H. Noguchi, N. Kikuchi, and G. Gompper, *Particle-based mesoscale hydrodynamic techniques*, Europhysics Letters **78**, 10005 (2007).

[86] I. O. Götze, H. Noguchi, and G. Gompper, *Relevance of angular momentum conservation in mesoscale hydrodynamics simulations*, Physical Review E **76**, 046705 (2007).

[87] T. Ihle and D. M. Kroll, *Stochastic rotation dynamics: A Galilean-invariant mesoscopic model for fluid flow*, Physical Review E **63**, 020201 (2001).

[88] M. Ripoll, R. G. Winkler, and G. Gompper, *Hydrodynamic screening of star polymers in shear flow*, European Physical Journal E **23**, 349 (2007).

[89] A. Lamura, G. Gompper, T. Ihle, and D. M. Kroll, *Multi-particle collision dynamics: Flow around a circular and a square cylinder*, Europhysics Letters **56**, 319 (2001).

[90] N. Kikuchi, M. Pooley, J. F. Ryder, and J. M. Yeomans, *Transport coefficients of a mesoscopic fluid dynamics model*, Journal of Chemical Physics **119**, 6388 (2003).

[91] M. Ripoll, K. Mussawisade, R. G. Winkler, and G. Gompper, *Low-Reynolds-number hydrodynamics of complex fluids by multi-particle-collision dynamics*, Europhysics Letters **68**, 106 (2004).

[92] J. T. Padding and W. J. Briels, *Translational and rotational friction on a colloidal rod near a wall*, The Journal of Chemical Physics **132**, 054511 (2010).

[93] J. Elgeti, U. B. Kaupp, and G. Gompper, *Hydrodynamics of Sperm Cells near Surfaces (Supporting Material)*, Biophysical Journal **99**, 1018 (2010).

[94] A. M. Pourmoosa, personal communication, 2011.

[95] J. Dunkel and I. M. Zaid, *Noisy swimming at low Reynolds numbers*, Physical Review E **80**, 021903 (2009).

[96] G. J. Vroege and H. N. W. Lekkerkerker, *Phase transitions in lyotropic colloidal and polymer liquid crystals*, Reports on Progress in Physics **55**, 1241 (1992).

[97] J. Gray and H. W. Lissmann, *The Locomotion of Nematodes*, Journal of Experimental Biology **41**, 135 (1964).

[98] G. J. Elfring and E. Lauga, *Hydrodynamic Phase Locking of Swimming Microorganisms*, Physical Review Letters **103**, 088101 (2009).

[99] R. Rikmenspoel, *The Tail Movement of Bull Spermatozoa: Observations and Model Calculations*, Biophysical Journal **5**, 365 (1965).

[100] S. F. Goldstein, *Asymmetric waveforms in echinoderm sperm flagella*, Journal of Experimental Biology **71**, 157 (1977).

[101] H. C. Fu, T. R. Powers, and C. W. Wolgemuth, *Theory of Swimming Filaments in Viscoelastic Media*, Physical Review Letters **99**, 258101 (2007).

[102] Y.-G. Tao, I. O. Götze, and G. Gompper, *Multiparticle collision dynamics modeling of viscoelastic fluids*, Journal of Chemical Physics **128**, 144902 (2008).

[103] S. Ji, R. Jiang, R. G. Winkler, and G. Gompper, *Mesoscale hydrodynamic modeling of a colloid in shear-thinning viscoelastic fluids under shear flow*, Journal of Chemical Physics **135**, 134116 (2011).

[104] G. Sutmann, R. G. Winkler, and G. Gompper, Simulating hydrodynamics of complex fluids: Multi-particle collision dynamics coupled to molecular dynamics on massively parallel computers, (in preparation).

[105] J. Sanders and E. Kandrot, *CUDA by Example - An Introduction to General-Purpose GPU Programming* (Addison-Wesley, 2011).

[106] E. Westphal, C.-C. Huang, S. P. Singh, R. G. Winkler, and G. Gompper, GPU accelerated mesoscale simulations of multi-particles collision dynamics, (in preparation).

Kurzzusammenfassung

Selbstangetriebene Mikroschwimmer sind Organismen oder künstliche Schwimmer die sich aus eigener Kraft in Flüssigkeit fortbewegen können. Beispiele hierfür sind Spermien, verschiedene schwimmende Bakterien wie Escherichia coli, die grüne Alge Chlamydomonas reinhardtii und künstliche bimetallische Stäbchen die als Katalysator für Wasserstoffperoxid fungieren. Obwohl sich diese Schwimmer in ihrer Größe und in ihrem Antriebsmechanismus unterscheiden, können sie anhand ihrer Polarität als Pusher oder Puller klassifiziert werden. Pusher werden dabei im hinteren Bereich, Puller im vorderen Bereich angetrieben. Schwimmer verschiedener Polarität zeigen ein stark unterschiedliches Verhalten. Um dieses zu untersuchen entwickeln wir ein Modell von stäbchenähnlichen Schwimmern und führen dreidimensionale Simulationen durch. Wir modellieren die hydrodynamischen Wechselwirkungen mit Hilfe einer teilchen-basierten mesoskopischen Simulationstechnik (Multi Particle Collision Dynamics, MPCD).

Im Mittelpunkt unseres Interesses stehen die Wechselwirkungen der Schwimmer untereinander und mit Wänden bei hohen Schwimmerkonzentrationen. Betrachtet man einzelne Schwimmer so zeigt sich, dass Schwimmer aller Polaritäten (Pusher, Puller und neutral angetrieben) die meiste Zeit nahe den Oberflächen zu finden sind. Am stärksten ausgeprägt ist dieser Effekt jedoch im Fall der Pusher. Diese werden durch hydrodynamische Wechselwirkung mit der Wand und durch Kollision mit ihr parallel zu der Wand ausgerichtet. Des Weiteren sorgen die hydrodynamischen Wechselwirkungen für eine Anziehung zwischen Pusher und Wand, so dass die Pusher sehr nahe and der Wand schwimmen. Diese Anziehungskraft messen wir in der Simulation und vergleichen sie mit dem Dipolmodell, welches häufig als Fernfeldnäherung für das Flussfeld um selbstangetriebene polare Schwimmer verwendet wird. Für Puller können wir zeigen, dass sie durch hydrodynamische Abstoßung von der Wand in der Mitte ihres Körpers und durch Anziehung an ihrem vorderen Ende leicht in Richtung Wand geneigt schwimmen. Durch diese Ausrichtung zur Wand verlassen sie diese trotz der Abstoßung nicht. Allerdings schwimmen sie dadurch in etwas größerem Ab-

stand von der Wand als Pusher.

In der Vergangenheit wurden Studien über selbstangetriebene Schwimmer bei hoher Dichte meistens im zweidimensionalen Raum durchgeführt, oder es wurden Hydrodynamik oder körperliche Wechselwirkungen nicht beachtet. Durch Verwendung effizienter Parallelisierung auf GPU Hardware sind wir im Stande das kollektive Verhalten von Stäbchen im dreidimensionalen Raum bei verschiedenen Dichten und Antriebskräften zu untersuchen, unter Berücksichtigung von Hydrodynamik und körperlichen Wechselwirkungen. Unsere Ergebnisse zeigen die Bedeutung der Polarität der Schwimmer: Neutral angetriebene Stäbchen zeigen nur schwache hydrodynamische Wechselwirkung. Die körperliche Wechselwirkung jedoch führt zu einer Verschiebung des isotrop-nematischen Phasenübergangs zu geringeren kritischen Dichten, verglichen mit passiven Stäbchen. Pusher Stäbchen richten sich parallel zueinander aus und formen mittelgroße bewegliche Cluster, die sich zu Flussdefekten wie Jets und Strudel entwickeln können. Die Cluster schwimmen hauptsächlich nahe der Oberflächen, wo die Konzentration der Stäbchen am höchsten ist. Das Konzentrationsgefälle zwischen Wand und Systemmitte nimmt jedoch mit ansteigender Stäbchendichte ab. Während auf kurzen Distanzen polare Ordnung auftritt, wird diese auf großen Skalen durch die Flussdefekte zerstört. Wir können jedoch zeigen, dass sich bei hohen Pusherdichten systemweit eine positive nematische Ordnung einstellt, sich also auch Cluster aneinander ausrichten können.

Die Cluster in Puller Systemen sind grundlegend anders. Bei einer geringen Stäbchendichte werden an den Wänden mehrere kleine unbewegliche igelähnliche Cluster gebildet, die sich bei hoher Stäbchendichte zu einem riesigen, von Wand zu Wand reichenden Cluster entwickeln. Diese riesigen Cluster umfassen gewöhnlich einen großen Anteil aller Stäbchen des Systems. Die Cluster sind zwar unbeweglich, jedoch nicht statisch; sie verformen sich langsam. Wir gehen davon aus, dass sich die Puller Cluster aufgrund von sternförmigen Flussdefekten verbunden mit körperlichen Wechselwirkungen bilden.

Wir setzen Studien über ein spezifischeres Spermienmodell fort. Diese Modellspermien zeigen ebenfalls eine erhöhte Schwimmerkonzentration nahe der Oberflächen. Außerdem können zwei dieser Spermien sich einander anziehen und synchronisieren. In Simulationen mit vielen geradeaus schwimmenden Spermien zeigen wir die Bildung von kleinen Clustern, für Clusterbildung unter gebogenen Spermien jedoch ist die Wechselwirkung zu schwach. Um die Wechselwirkungsstärke zu erhöhren modifizieren wir das sinusförmige Schlagmuster des

Flagellums so, dass die Schlagamplitude zum Ende des Schwanzes hin ansteigt. Dies führt tatsächlich dazu, dass die Synchronisation zwischen zwei Spermien für längere Zeit anhält, verglichen mit dem Modell mit sinusförmigem Schlagmuster.

Acknowledgments

I would like to give my thanks to Gerhard Gompper for his support, advice, good ideas, fruitful discussions and of course for giving me the opportunity to work in such an interesting place as the Forschungszentrum Jülich. Jens Elgeti provided one of the simulation programs I used in my work, and I would like to thank him for keeping the code well readable, as well as providing helpful advice. I acknowledge financial support from the *International Helmholtz Research School on Biophysics and Soft Matter BioSoft* and want to thank all members of the IHRS BioSoft for many experiences I would not want to miss and for extending my understanding of biological topics significantly. Special thanks go to Thorsten Auth for his work as the coordinator of the research school. All members of the ICS-2 group did their great part in creating a very amicable atmosphere.

Finally I want to thank Sina Borchert for her tremendous support going beyond words in all other aspects of my life, for motivation and for her patience.

Erklärung

Ich versichere, dass ich die von mir vorgelegte Dissertation selbständig angefertigt, die benutzten Quellen und Hilfsmittel vollständig angegeben und die Stellen der Arbeit - einschließlich Tabellen, Karten und Abbildungen -, die anderen Werken im Wortlaut oder dem Sinn nach entnommen sind, in jedem Einzelfall als Entlehnung kenntlich gemacht habe; dass diese Dissertation noch keiner anderen Fakultät oder Universität zur Prüfung vorgelegen hat; dass sie noch nicht veröffentlicht worden ist sowie, dass ich eine solche Veröffentlichung vor Abschluß des Promotionsverfahrens nicht vornehmen werde. Teilpublikationen liegen nicht vor. Die Bestimmungen dieser Promotionsordnung sind mir bekannt. Die von mir vorgelegte Dissertation ist von Prof. Dr. G. Gompper betreut worden.